

*Department of Construction Sciences*  
Solid Mechanics

ISRN LUTFD2/TFHF-18/5228-SE(1-84)

# **Fracture mechanics and damage modeling of injection molded high density polyethylene**

Master's Dissertation by  
**Isabelle Wahlström**

Supervisors:  
PhD Elin Persson Jutemar, Tetra Pak®  
M. Sc Viktor Petersson, Tetra Pak®  
PhD Jonas Engqvist, Div. of Solid Mechanics

Examiner:  
Assoc. Prof. Stephen Hall, Div. of Solid Mechanics

Copyright © 2018 by the Division of Solid Mechanics  
and Isabelle Wahlström

Printed by Media-Tryck AB, Lund, Sweden

For information, address:

Division of Solid Mechanics, Lund University, Box 118, SE-221 00 Lund, Sweden

Webpage: [www.solid.lth.se](http://www.solid.lth.se)



# Abstract

For many applications a fracture is a disaster, leading to failure of the application and thus its usefulness. However, when it comes to the opening of a food and beverage package, fracture is a necessity. At Tetra Pak, food and beverage packages are produced to make food safe and available everywhere. Today, many of the packages include polymer parts, such as the opening of the packages.

In the technology development process, virtual engineering has become an important tool. The possibility of performing simulations may shorten the development time and increase the quality of the product. To perform simulations that are close to the real behavior of the material, the mechanical properties need to be known.

At Tetra Pak®, the general knowledge of the mechanical properties of a polymer is well known by the use of tensile tests, which can be translated into a material model. However, this model is on macroscopic scale and does not include microstructure nor damage modeling. Therefore, X-ray scattering was used to further investigate the microstructure, whilst the fracture mechanical behavior has been studied by the use of tensile testing, Scanning Electron Microscopy and Digital Image Correlation.

From the experimental test, it was concluded that the positioning and the direction of a crack leads to highly different fracture mechanical behavior, indicating that the anisotropy plays an important role. Furthermore, the internal layers of an injection molded polymer delaminate during tensile testing. The knowledge gained from the experiments was used to create a virtual model, including damage modeling to capture the damage behavior. The virtual model captured the overall mechanical response and damage behavior well, though further work to improve the model can be done.

# Preface

This master thesis was conducted at Tetra Pak Packaging Solutions AB in Lund, during the spring of 2018 and is the continuation of my work as a Technical Talent at Tetra Pak. Therefore, I would like to start off with thanking my former mentor Leo Persson, who guided me through my years as a Technical Talent and taught me a lot about polymers and not to forget initiated this master thesis.

This thesis would not have been possible without the help of some very important people, my supervisors at Tetra Pak; PhD. Elin Persson Jutemar, Viktor Petersson and Eskil Andreasson. I truly consider this thesis to have been a team effort and I am very grateful for the help, guidance and many interesting discussions throughout the project. Though I have done my thesis independently, I have never felt lonely.

Furthermore, I would like to thank my supervisor at LTH; PhD. Jonas Engqvist. You have been a great support and guidance throughout this project, especially during the Digital Image Correlation testing and interpretation of the Small Angle X-ray Scattering and Wide Angle X-ray Scattering data. I could not have asked for a more competent, interested and encouraging supervisor.

Finally, I would like to thank Linnea Björn, master thesis student at Chalmers who also conducted her thesis at Tetra Pak. Without you, there would not have been any X-ray scattering in this thesis.

There are many more, who have been a part of making this thesis a success. To all of you I am grateful.

# Abbreviations

CD – Cross direction

CTOD – Crack tip opening displacement

DIC – Digital image correlation

DVC – Digital volume correlation

HDPE – High density polyethylene

LDPE – Low density polyethylene

MD – Machine direction

SAXS – Small angle X-ray scattering

SEM – Scanning electron microscopy

WAXS – Wide angle X-ray scattering

XRD – X-ray diffraction

# Contents

<b>1</b>	<b>Introduction.....</b>	<b>1</b>
1.1	Background.....	1
1.1.1	<i>Previous work.....</i>	2
1.2	Problem Formulation.....	6
1.3	Objective.....	6
1.4	Restrictions.....	6
1.5	Method.....	6
<b>2</b>	<b>Theory.....</b>	<b>8</b>
2.1	Polymers.....	8
2.1.1	<i>Morphology.....</i>	8
2.1.2	<i>Mechanics of Polymers.....</i>	9
2.2	Injection Molding.....	12
2.2.1	<i>Process.....</i>	12
2.2.2	<i>Effect on Morphology of Polymers.....</i>	13
2.3	Fracture mechanics.....	14
2.3.1	<i>Fracture Mechanics and Damage Behavior of Polymers.....</i>	17
2.4	Tensile Testing.....	19
2.5	Virtual Engineering.....	20
2.5.1	<i>Material Models in Abaqus.....</i>	20
2.5.2	<i>Damage Models in Abaqus.....</i>	21
2.6	Scanning Electron Microscopy.....	24
2.7	Digital Image Correlation.....	26
2.8	Small Angle X-ray Scattering and Wide Angle X-ray Scattering.....	28
<b>3</b>	<b>Experiments and Results.....</b>	<b>30</b>
3.1	Dogbone Sample.....	33
3.1.1	<i>Tensile Testing.....</i>	33
3.1.2	<i>Small Angle X-ray Scattering and Wide Angle X-ray Scattering.....</i>	36
3.2	Fracture Mechanical Testing.....	42
3.2.1	<i>Tensile Testing.....</i>	42
3.2.2	<i>Scanning Electron Microscopy.....</i>	47
3.2.3	<i>Digital Image Correlation.....</i>	49

<b>4</b>	<b>Abaqus Simulation</b> .....	<b>59</b>
4.1	Dogbone Sample.....	59
4.2	Fracture Mechanical Testing .....	61
<b>5</b>	<b>Discussion</b> .....	<b>65</b>
<b>6</b>	<b>Conclusion</b> .....	<b>68</b>
<b>7</b>	<b>Future Work</b> .....	<b>69</b>
<b>8</b>	<b>References</b> .....	<b>70</b>
<b>Appendix</b> .....		<b>72</b>
A.	Data collection points for SAXS and WAXS for deformed specimen.....	72
B.	Tensile Testing of Plates.....	73
C.	SEM-images .....	76

# 1 Introduction

## 1.1 Background

Tetra Pak is a world leading company in packaging solutions and processing. The company was founded in Lund, 1951 by Ruben Rausing. It started off with developing a paper-based package for milk, which required a minimum amount of material use, whilst still providing maximum hygiene, thus creating the Tetra Classic® [1]. Today, Tetra Pak employs more than 24 000 worldwide people and has created a range of packages in its portfolio, as shown in Figure 1.1, packages that are distributed to people in more than 170 countries. Some of the many products that can be packaged or processed in Tetra Pak machines are beverages, dairy products, ice cream, cheese, food, vegetables and pet food [2].



Figure 1.1: The range of Tetra Pak packages, with the original package Tetra Classic® to the far left [2].

From the beginning, the packages were made primarily out of polymer coated paper. Today, increasingly more polymers are being incorporated in the package, whilst still having paperboard as the main constituent. The use of polymer parts makes it possible to improve the performance and increase the design possibilities and use of packages. The polymer parts are mostly found in the caps and the tops and are often manufactured by means of injection molding.

In the technology development process, virtual engineering has become an important tool. The possibility of performing simulations has facilitated and speeded up the development process. To perform simulations that mimic the actual behavior of the material the mechanical properties need to be known. At Tetra Pak, the general knowledge of the mechanical properties of a polymer is well known by the use of tensile tests, which can be translated into a material model. However, this model is on macroscopic scale and does not include neither microstructure nor damage modeling. Therefore, an extension of the current material model to include a damage model is needed to be able to capture the opening behavior of closures on a macroscopic scale.



### 1.1.1 Previous work

Prior to this master thesis, the author has been working at Tetra Pak as Technical Talent, during two years, performing material characterization. In this section a short summary of the previous work is presented since this thesis is a continuation of that work. The, for this thesis, relevant results and conclusions of the previous work are also presented.

The material characterization process is shown schematically in Figure 1.2. The process begins with injection molding plates out of which tests specimens can be made. The plate is defined in the ISO 294-5 standard, for which the geometry is presented in Figure 1.3. A description of the injection molding process is presented later on in this report, in section 2.2.1.



Figure 1.2: Schematic illustration of workflow in previous work.

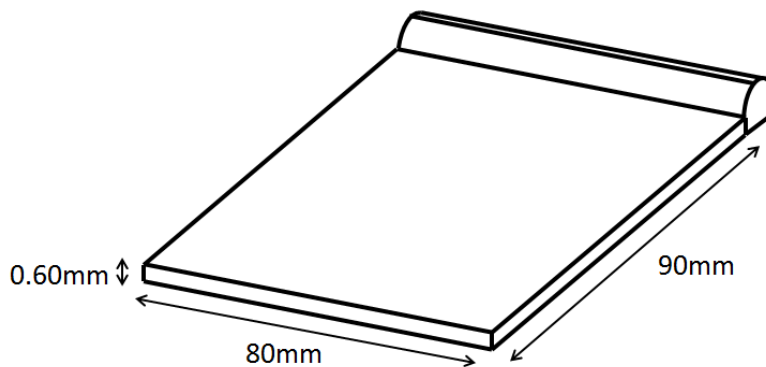


Figure 1.3: Geometry of injection molded plate.

After the plates had been manufactured, the test specimen in the shape of dogbones were punched out in the machine direction (MD) and the cross direction (CD), as presented in Figure 1.4. MD is in the direction of the melt flow, whilst CD is in the perpendicular direction. The dogbone samples were tested in tensile loading at various temperatures, displacement rates and in the two material directions, as shown in Table 1.1.

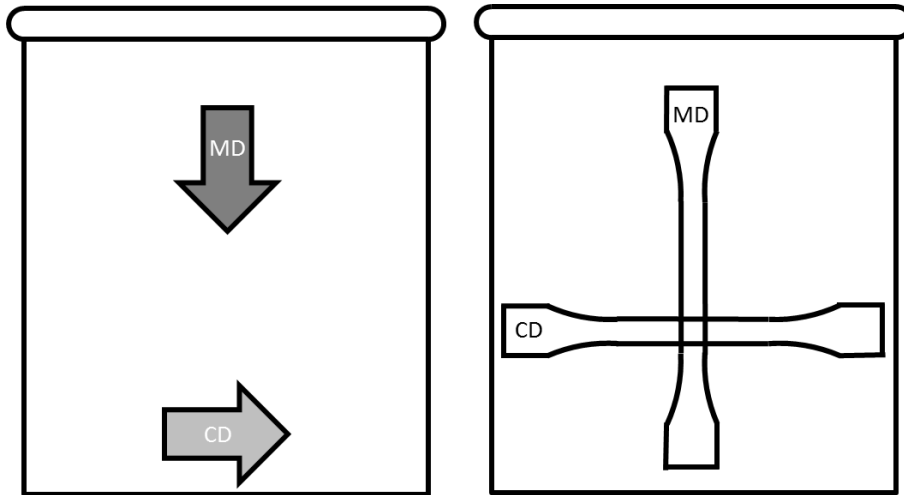


Figure 1.4: Injection molded plate with directions and test specimen positions.

Table 1.1: Settings used for tensile testing.

Settings			
<b>Temperature</b>	6°C	23°C	35°C
<b>Displacement rate</b>	50 mm/min	100 mm/min	300 mm/min
<b>Material direction</b>	MD	CD	

From each setting, a force-displacement curve was extracted. By testing 10 specimens for the same setting an averaged curved was constructed, until the first fracture. By the use of inverse calibration, a material card for the material for the specific settings was created. The inverse calibration is an optimization loop where the material parameters are adjusted to decrease the difference obtained in the simulation compared to the physical test. A schematic illustration of the inverse calibration and thus the optimization loop is illustrated in Figure 1.5. The optimization loop is exited when either the error is sufficiently low or a maximum number of loops has been performed.

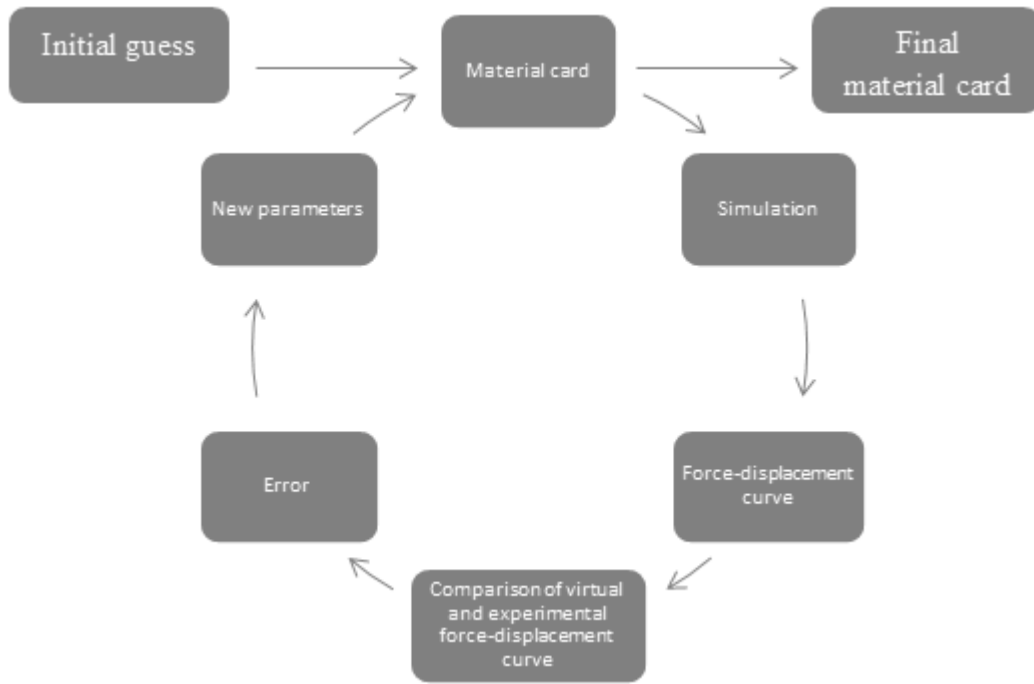


Figure 1.5: Schematic illustration of the inverse calibration process.

In Figure 1.6, plots of the final comparison between physical and virtual force-displacement curve is shown as well as the true stress-strain curve. The true stress-strain curve is an analytical expression determined by nine parameters from the simulation. The damage behavior is related to the end of these curves and beyond since these curves are up to the first fracture. In this thesis, force-displacement curves are presented in normalized force and normalized displacement. The same normalization is used throughout the report, enabling comparison of plots.

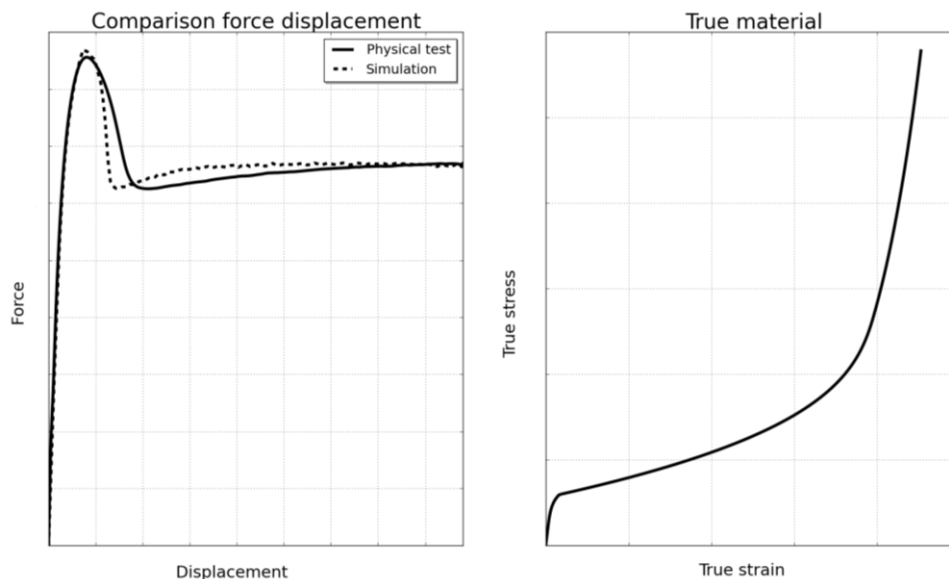


Figure 1.6: Comparison of force-displacement curves from inverse calibration. True stress strain curve from simulation.

From the extracted data the conclusion could be made that there is a temperature and displacement rate dependency. It could also be concluded that the material has very different

properties in the two different material directions, as shown in Figure 1.7 and Figure 1.8. CD, compared to MD, has a higher yield strength, which is followed by a sharper drop in force as well as less extension before fracture. An increase in temperature leads to a decrease in force, whilst increasing the displacement rate leads to higher yield strength.

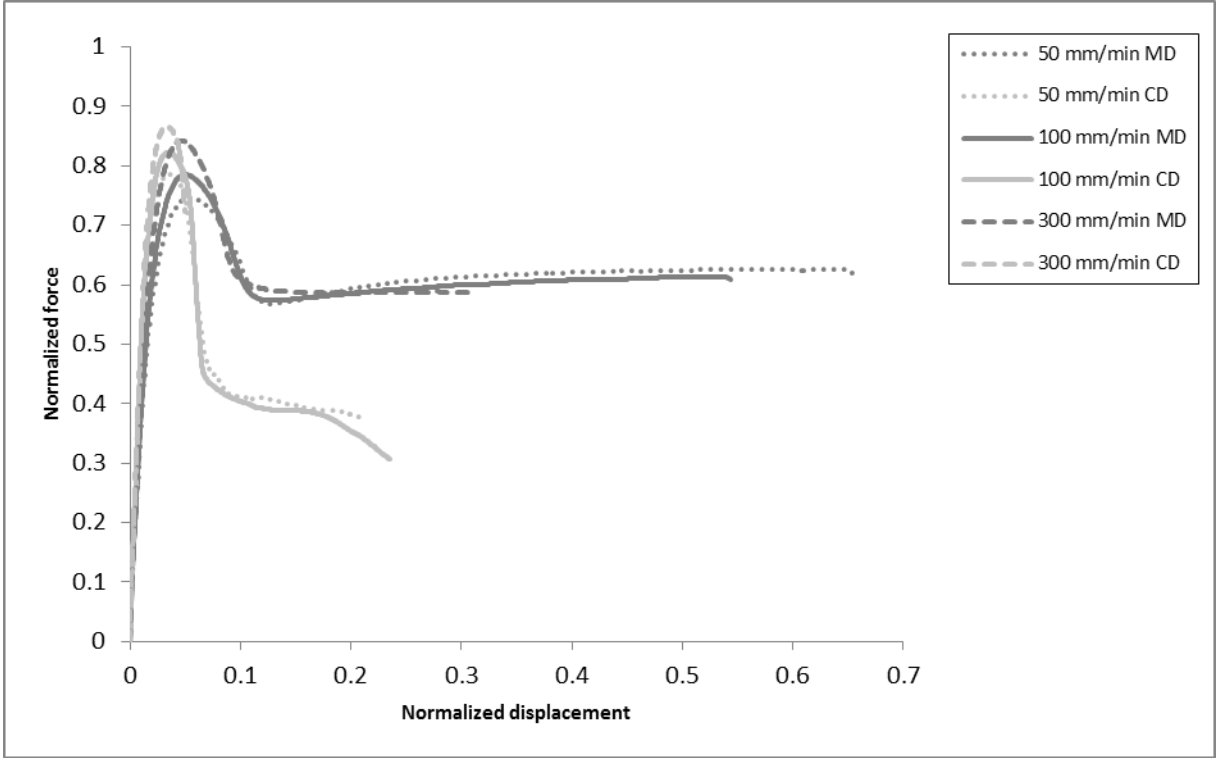


Figure 1.7: Normalized force-displacement curves showing displacement rate dependency at 23°C.

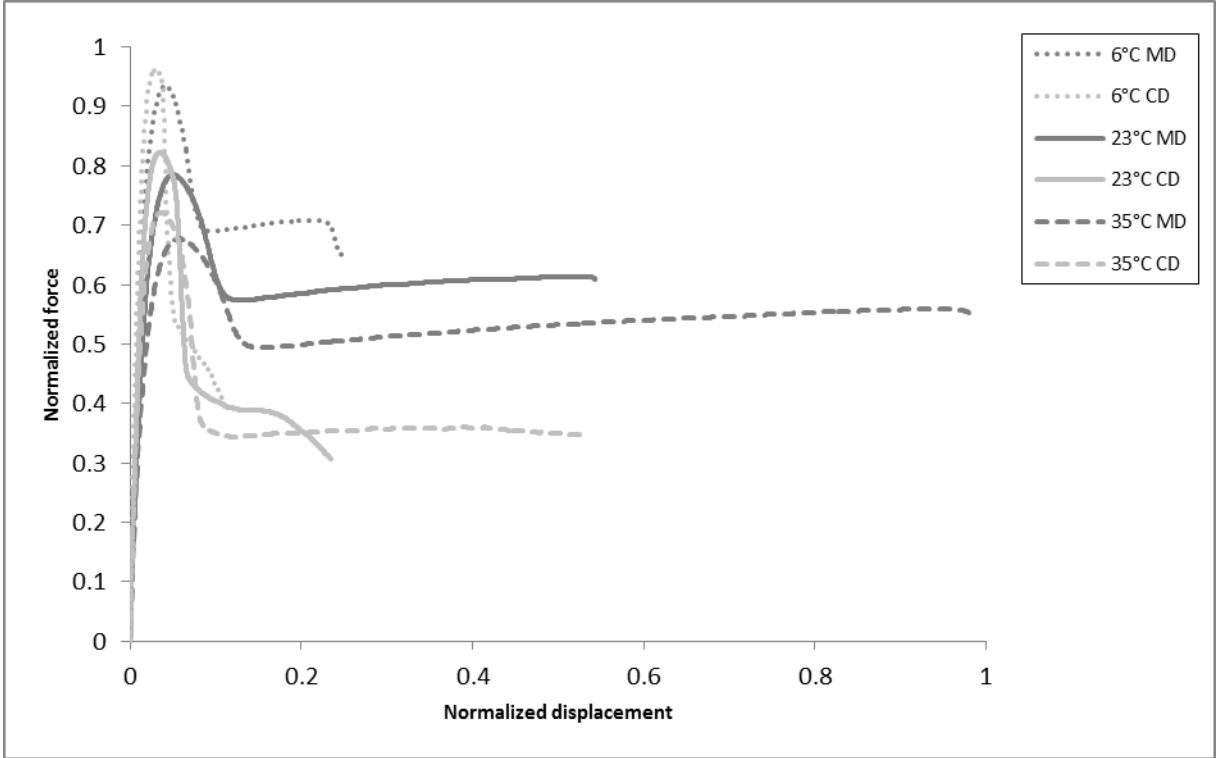


Figure 1.8: Normalized force-displacement curves showing temperature dependency at 100 mm/min.

## 1.2 Problem Formulation

The use of virtual engineering is being increasingly used to reduce the development time and cost. Polymer parts are commonly used in packages, especially in the caps and tops. For simulations to better capture the behavior of openings, more knowledge of damage behavior, damage modeling and damage criteria is needed. This knowledge is to be gained from experimental and virtual test methods.

## 1.3 Objective

The objective of this master thesis is to increase the knowledge of damage behavior, damage modeling and damage criteria for an injection molded ductile polymer to be able to better capture the real behavior of openings in simulations. By doing so the development process can be improved, leading to new designs with better mechanical properties and less material use.

## 1.4 Restrictions

In the Tetra Pak packages there are a number of different polymers being used. This thesis is focused on one of them. Furthermore, the applications are used in a variety of temperatures, though in this thesis tests are focused on behavior at room temperature. The tests are also configured in such a way that they are feasible to perform in the available test equipment. This leads to a limitation in specimen dimensions and also test parameters as speed and maximum extension.

## 1.5 Method

The method used in this thesis consist of several segments that are interlinked. A schematic illustration of the method and its constituents is shown in Figure 1.9. The process included going back and forward to segments due to after time more knowledge being gained, thus leading to new ideas and approaches.

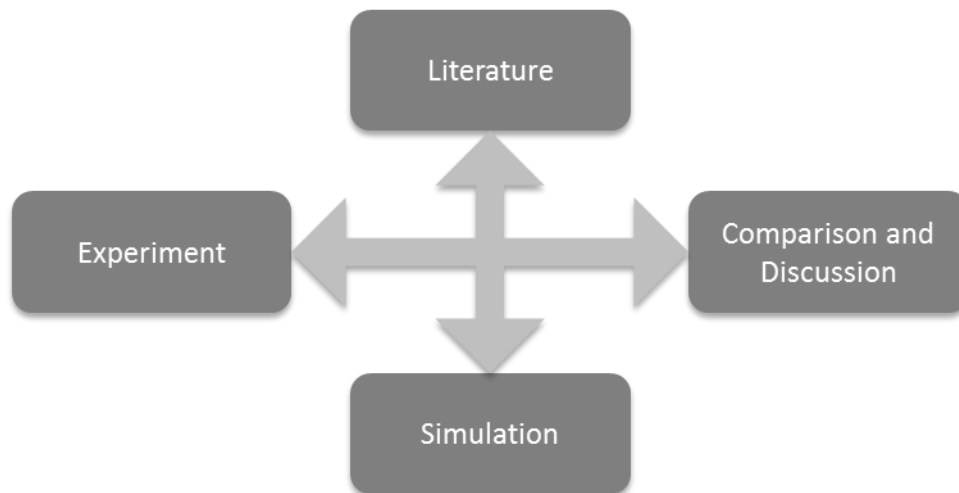


Figure 1.9: Schematic illustration of the methodology.

The experimental techniques included in this thesis work are:

- Tensile testing of dogbone sample
- Tensile testing of cracked plates
- Digital Image Correlation (DIC)
- Scanning Electron Microscopy (SEM)
- Small Angle X-ray Scattering (SAXS)
- Wide Angle X-ray Scattering (WAXS)

To study and model fractures in a polymer part, several steps are required. To start with test specimens are to be produced. This includes injection molding plates, out of which test specimens are punched or cut out from. To be able to properly model the damage behavior, knowledge of the continuum behavior is need. Therefore, tensile testing of the polymer is required. The material properties can then be an input to the virtual engineering in Abaqus, where different models for continuum and damage behavior can be implemented and evaluated. To gain further knowledge and understanding of the internal structure of the material, and thus see if this explains the macroscopic behavior, X-ray scattering is used.

To investigate the fracture mechanics further, a different type of test specimen is used during tensile testing, a cracked plate. SEM is used to investigate more in detail how the fracture looks. To further investigate the heterogeneous deformation and damage, DIC is used in conjunction with tensile testing. DIC is a full-field measurement method, making it possible to study how the whole part reacts to load and not only measure what is happening in a single point or at the boundaries, which traditionally has been the case for tensile testing. The use of DIC for studying material behavior of polymers has been used in several studies, for example by Hwang et al. [3]. DIC has also been used by Abanto-Bueno and Lambros [4] to study the displacement field around a growing crack and thereby investigate the fracture behavior. In this thesis DIC is primarily used to compare the simulation results to the experimental, rather than studying the material behavior of the test specimen in detail.

## 2 Theory

### 2.1 Polymers

#### 2.1.1 Morphology

Polymers are molecules consisting of many small repeating units, also referred to as monomers. For polymers there are two main groups; thermosets and thermoplastics. Thermosets have a network molecular structure, i.e. there is crosslinking between the molecular chains. Due to this structure, thermosets do not soften when heated. Thermoplastics on the other hand do not have crosslinks and thus soften when heated. Thermoplastics can be melted and cooled repeatedly, which results in many manufacturing processes in which they can be used and also enables recycling.

Polymers can further be divided into two groups depending on the crystallinity of the polymer; amorphous and semi-crystalline. Crystallinity is when the molecular chains are packed and aligned in an ordered atomic arrangement. The degree of crystallinity may vary from none to about 95% crystalline. A polymer in which there is no order is called amorphous, whilst a polymer with some degree of order is called semi-crystalline, as illustrated in Figure 2.1 [5].

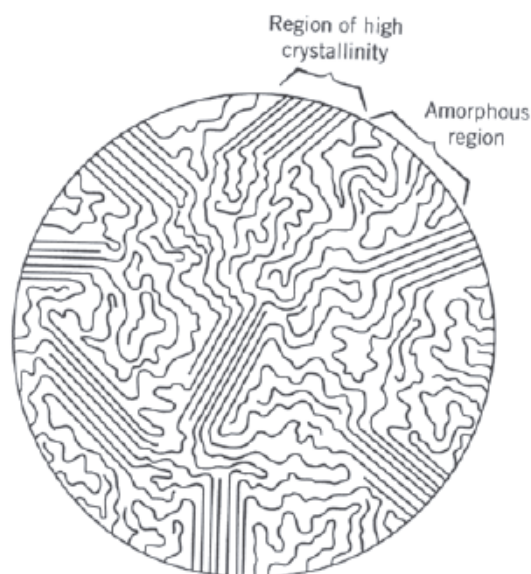


Figure 2.1: Molecular structure of a semi-crystalline polymer, showing amorphous and crystalline regions [5].

#### High Density Polyethylene

In this master thesis, the material being studied is a semi-crystalline high density polyethylene (HDPE), which is a thermoplastic polymer. The polyethylene molecule consists of a repeating unit of carbon and hydrogen. The molecular chains of polyethylene can have lateral branches, as shown in Figure 2.2, which affects the density and crystallinity of the polymer. Less amount of lateral branching results in higher crystallinity and hence higher density. HDPE has

no or few lateral branches, resulting in a high density, whilst, low density polyethylene (LDPE) has more branching and thus a lower density [6].

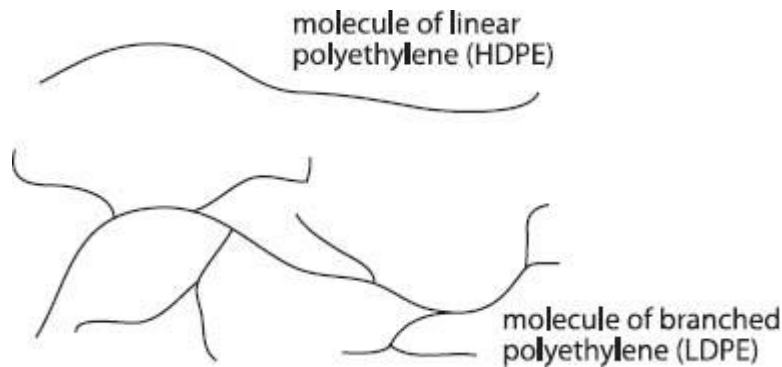


Figure 2.2: Lateral branching of HDPE and LDPE [7].

### 2.1.2 Mechanics of Polymers

The mechanical properties of polymers can be specified by Young's modulus, yield and tensile strength. These as well as other parameters can be determined from a stress-strain curve obtained from a tensile test. A typical stress-strain curve for semi-crystalline polymers is shown in Figure 2.3. The mechanical properties of polymers and thus the resulting stress-strain curve is highly dependent on temperature, strain rate, its environment and how the sample was produced. An increase in temperature will lead to a decrease in Young's modulus and tensile strength but an increase in ductility, where tensile strength refers to the stress at which fracture occurs. Also, strain rate has an effect on the material properties. If the strain rate is decreased, the material becomes softer and more ductile. There are typically three different stress-strain behaviors for polymers; brittle, plastic and highly elastic, as presented in Figure 2.4 [5].

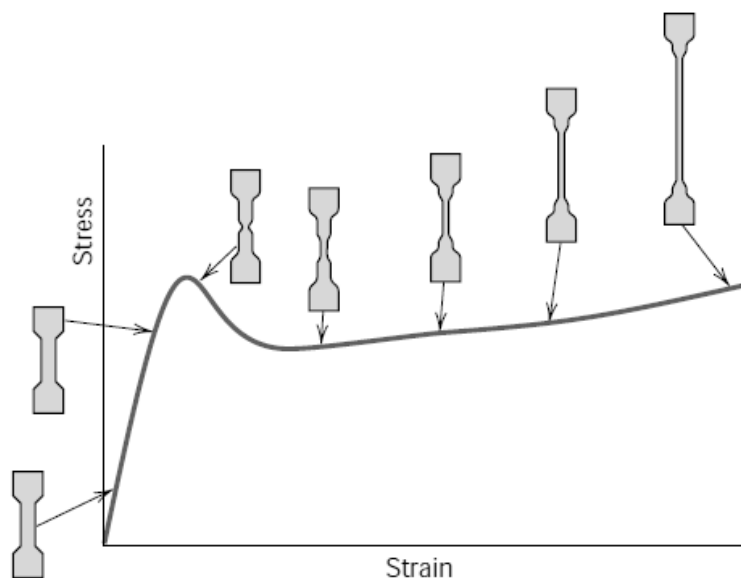


Figure 2.3: Typical stress-strain curve for a semi-crystalline polymer [5].



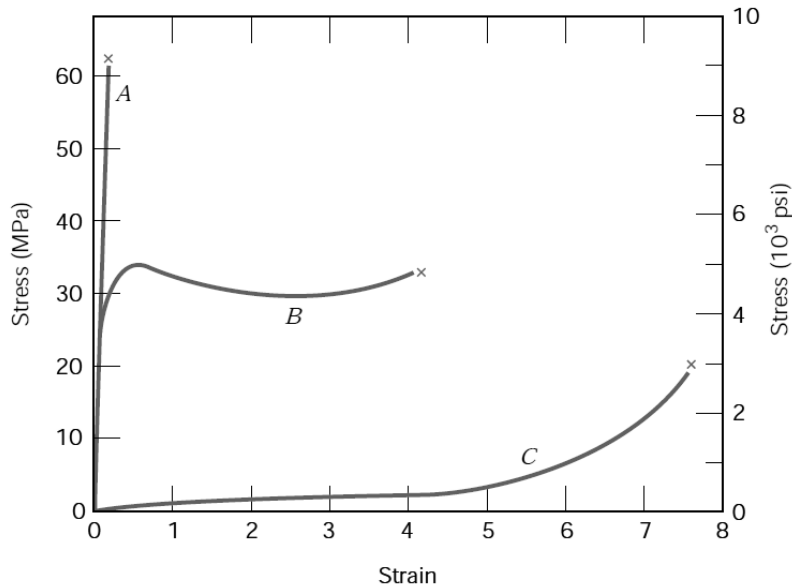


Figure 2.4: Stress-strain curves, A brittle, B plastic and C highly elastic [5].

The stress-strain curve from a tensile test can determine several parameters. In Figure 2.5 a typical stress-strain curve is shown, with different regions marked. The first region up to point A is the linear range in which Young's modulus, the stiffness of the material, can be calculated as the slope of the curve. Up to point B the material is in the elastic region, which means the sample would return to its original shape after unloading. At point C the yield stress of the material and the corresponding elongation can be measured. After point C necking occurs which will extend until breakage, see also Figure 2.3. At failure, point D, the failure stress and the failure strain can be determined [6].

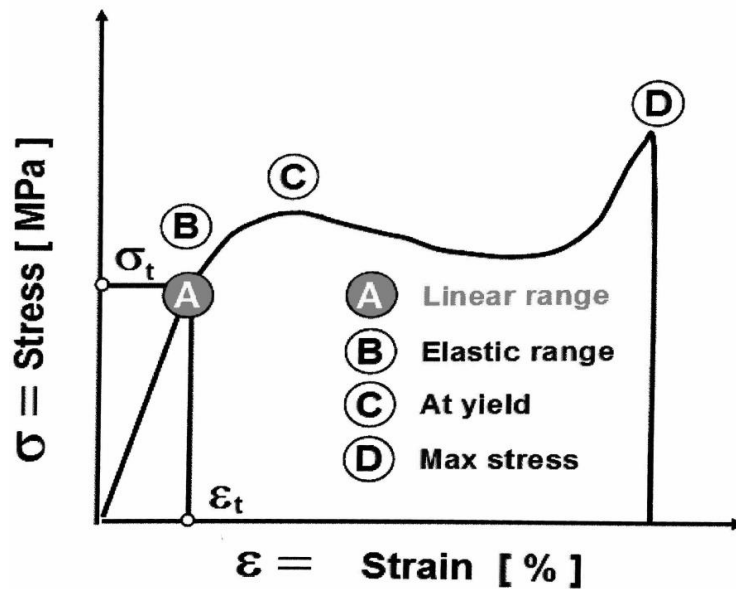
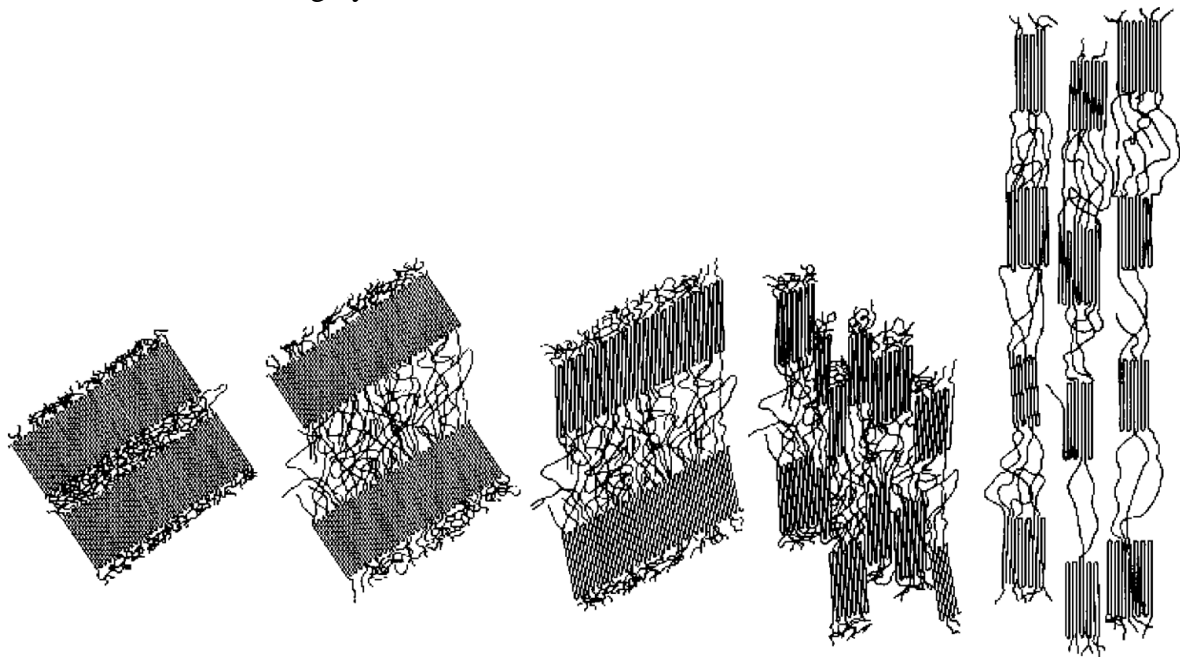


Figure 2.5: Typical stress-strain curve with points marked [6].

Semi-crystalline polymers consist of amorphous regions and crystalline lamellar regions. When a semi-crystalline polymer starts to deform, the amorphous regions start to align in the direction of applied tensile load, as shown in Figure 2.6. The process continues with change both in the amorphous and crystalline regions. The amorphous chains continue to align and become elongated and in the lamellar crystallites there is bending and stretching of the chain covalent bonds. This is all happening in the elastic region. When the plastic region is entered the lamellae start to align to the tensile axis, which results in them breaking up into thinner lamellae and leads to a highly oriented structure.



*Figure 2.6: Stages of deformation of a semi-crystalline polymer [5].*

As described in previous paragraphs, the material behavior during tensile loading can be described as a stress-strain curve, also called engineering stress-strain curve. This curve is based on the initial cross-section of the test specimen. However, the cross-sectional area will decrease during loading, resulting in a higher stress than that depicted by the stress-strain curve. Therefore, the stress-strain curve is only valid until the onset of necking. Taking into consideration this change in cross-sectional area, a true stress-strain curve can be constructed that is based on the instantaneous cross-sectional area and the instantaneous strain.

## 2.2 Injection Molding

Injection molding is one of the most common manufacturing techniques for polymer parts. In the following section a brief description of the injection molding process is given. Also, the effects on the morphology and thus the properties of polymer parts are presented.

### 2.2.1 Process

The injection molding process consists of taking plastic granules, melting them and pushing the melt into a mold followed by cooling and ejection of the plastic part. The plastic material can consist of a polymer or of a combination of polymer and masterbatch. A masterbatch is a concentrated additive used to change the color of the part or to improve properties such as UV-resistance and mechanical properties.

The injection molding machine consists of two parts; the injection unit and the clamping unit, as presented in Figure 2.7. In the injection unit, plastic granules are placed in a hopper, which feeds the injection machine with material. From the hopper the plastic granules are fed to a screw, where the material is heated and becomes a viscous melt. The screw continuously pushes the material towards the nozzle and thus the mold. At the nozzle, the melt flows into the mold cavity. The mold is a part of the clamping unit. The mold usually consists of two parts; one fixed mold half and one moveable. In the moveable half there are ejector pins that facilitates the removal of the part from the mold.

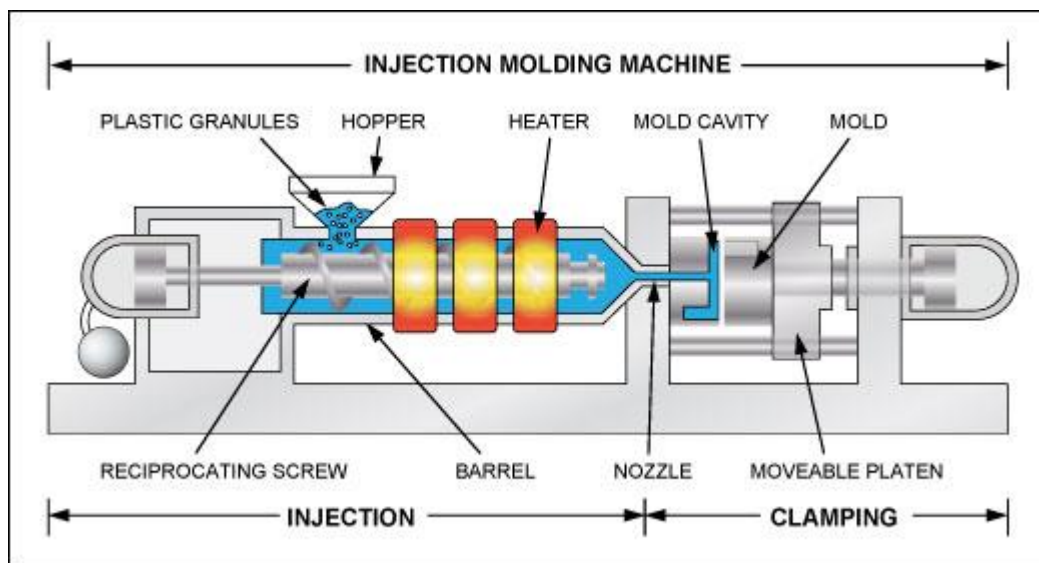


Figure 2.7: Schematic illustration of an injection molding machine [8].

The injection molding cycle starts with the mold closing, after which injection of molten material occurs. During the hold pressure phase more material is pushed into the mold to compensate for shrinkage when the part solidifies. Thereafter, the part is cooled, meanwhile the next dose of material is moved forward by the screw. Before the mold opens and ejects the part, there is a small pause time to compensate for variations in dosing time. When the part has been ejected, the mold is closed and a new cycle begins [6].

### 2.2.2 Effect on Morphology of Polymers

When cooling, in the injection molding process, different zones through the thickness of the polymer part are created, as presented in Figure 2.8. The zones have different properties due to the fact that they have different polymer/crystal orientation and amount of crystalline growth. The process settings used during the injection molding will affect the resulting layer thicknesses and the mechanical properties. Layers or zones are created in the injection molding process due to the shear forces that originate when the polymer melt is injected into the mold cavity and due to the temperature gradients build up during the cooling phase. The outer layer, the layer closest to the mold, is called the surface or the skin layer. This layer will be cooled quickly due to the cooler mold, resulting in an orientation of polymers in the flow direction. The inner part, called the core or bulk, has a random orientation of polymer chains, resulting in isotropy, i.e. the mechanical properties are independent of direction. Between the bulk and the skin is a layer called the shear zone, which experiences shear forces in the flow direction as well as rapid crystallization, resulting in high degree of orientation of the polymer chains. In the shear layer, the orientation of polymer chains is primarily in the flow direction [9].

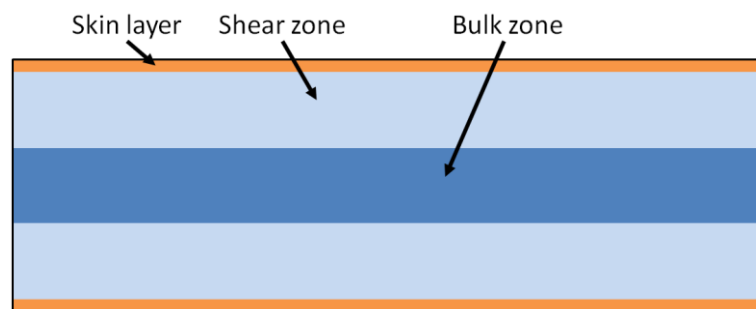


Figure 2.8: The different layers, through the thickness, created in the injection molding process.

Due to the solidification in the mold, there are different properties in different directions. There are two directions which are often used; MD and CD, as presented earlier in section 1.1.1.

## 2.3 Fracture mechanics

A fracture is an unstable crack growth, which can occur when an applied load reaches a critical value. If, at this load, there is no fracture, the crack will get rounded and expand without there being any instability and thus no crack growth. The more common case is for fracture to occur at a critical load. This load decreases with increasing crack length [10].

A crack can experience three types of loading, three different modes, as depicted in Figure 2.9. The first mode, mode I, consists of a principle load normal to the crack plane, resulting in opening of the crack. For mode II, the load is in-plane shear and hence tends to slide one crack face in relation to the other. Mode III is out-of-plane shear loading, also referred to as tearing. The loading of a cracked body can be in one mode or in a combination of different modes [11].

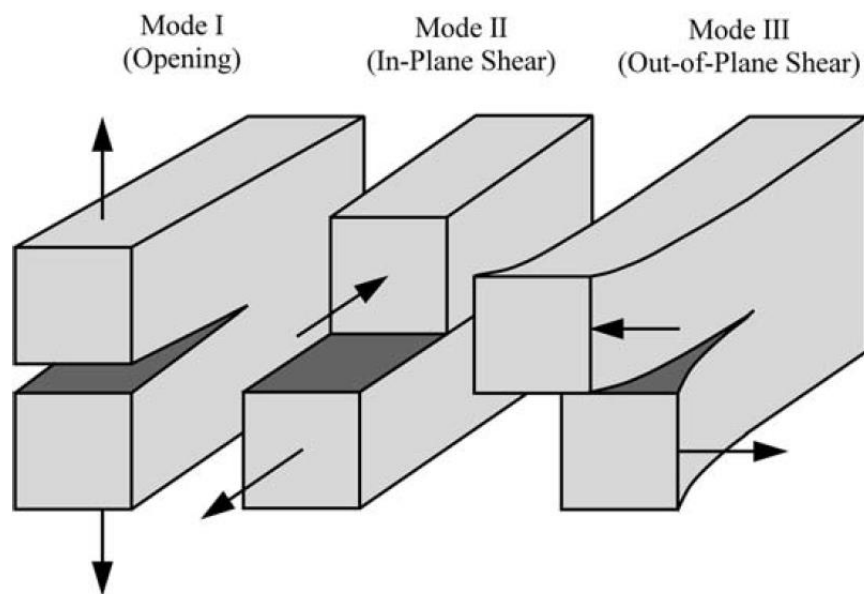


Figure 2.9: Modes of loading that can be applied to a crack [11].

The small region near the crack edge, where a structure fractures, is called the process region. This region is always small and subjected to high loads, regardless of the size of the structure failing. The physical appearance of the process region and the physical processes happening depend on the type of material and environmental conditions, such as temperatures and loading rate. In general, the important process in the process region is the nucleation and growth of micro-separations that eventually merge with the main crack. The micro-separation is a material separation, decohesion, on the microstructural level, which is nucleated at inhomogeneities in the material. The type of micro-separation depends on type of material as well as the local load velocity and triaxiality. Some types of micro-separations are voids, micro-cracks and disentangling of molecules. Depending on loading mode, the micro-separations may be created by tensile or shearing force.

When a fracture occurs, it is done so in a process consisting of phases. There are three distinct phases; loading without crack growth, stable crack growth and unstable crack growth. In a structure, near a crack, there are different regions that evolve during the loading phases, as

can be seen in Figure 2.10. The process region is the region closest to the crack edge, outside of which there is a plastic region. As the crack grows and the crack edge advances, there is a wake of the process region and the plastic region left behind. In the wake of the plastic region, the material returns to deforming elastically, however, a reversed plastic flow may occur leading to a secondary plastic region. Outside of these regions is the elastic region. The process region usually cannot be adequately analyzed by continuum mechanics, however, the plastic region can. Thus, calculating stresses and strains is not enough to solve crack and fracture problems, nevertheless the knowledge of stresses and strains in the area outside of the process region is essential for understanding the process of crack growth and fracture.

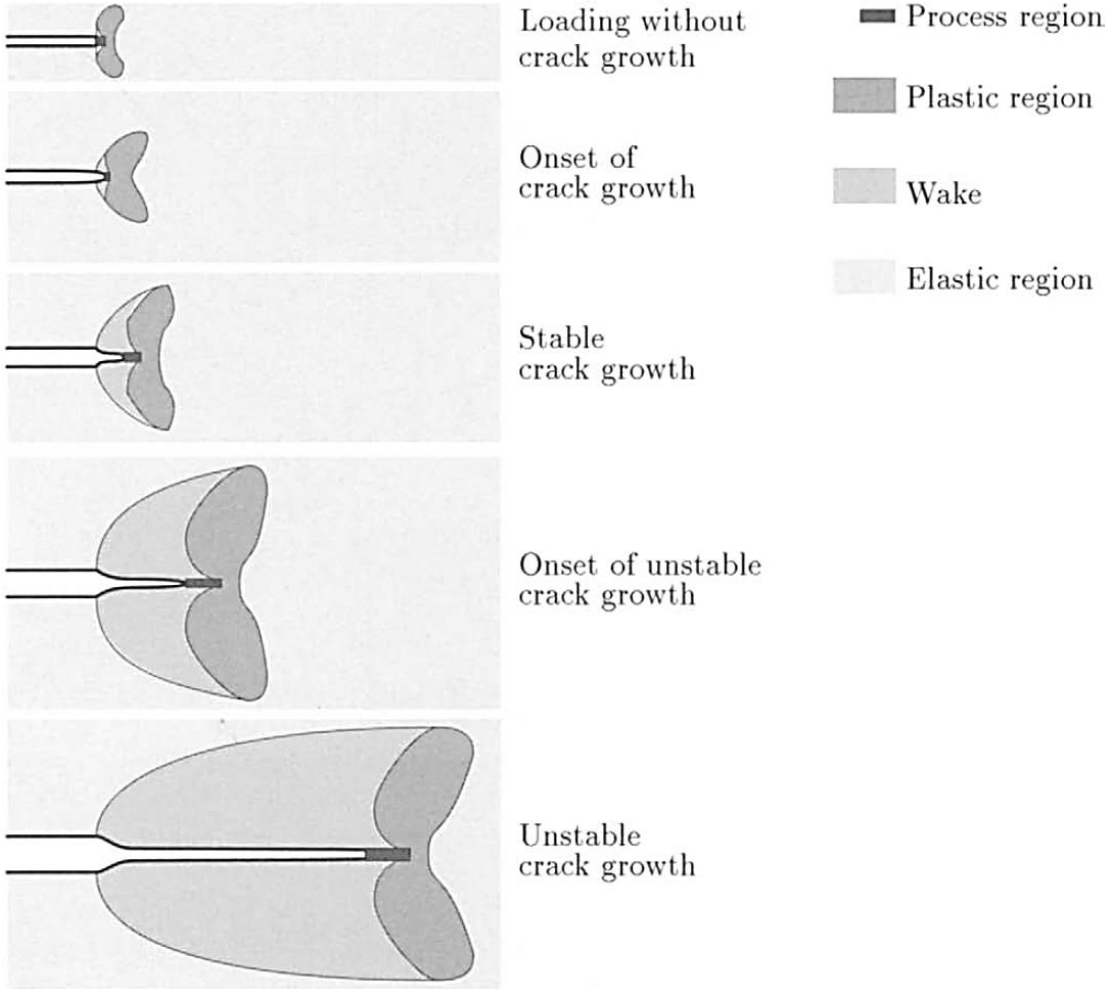


Figure 2.10: The phases of the fracture process and its corresponding regions [10].

In the first phases, loading without crack growth, a crack loaded in mode I will for small loads start to open and strain concentrations at the crack edge will appear. As the applied load is increased, there will for most materials be plastic flow and a process region will start to form. The process region is developed by micro-separations, which are the result of increasing stress and strains. Further increase of the load leads to growth of the process region and the plastic region. Moreover, there can be blunting of a sharp crack before there is any crack growth, as is represented in Figure 2.11. Blunting of the crack edge is caused by the plastic flow close to the crack edge and by the height increase of the process region. Several

experimental techniques for measuring the opening and blunting of the crack exist [10]. The degree of blunting in a material is a measurement of its fracture toughness, where an increase in blunting corresponds to an increased toughness. The parameter of crack blunting is called crack tip opening displacement (CTOD) [11].

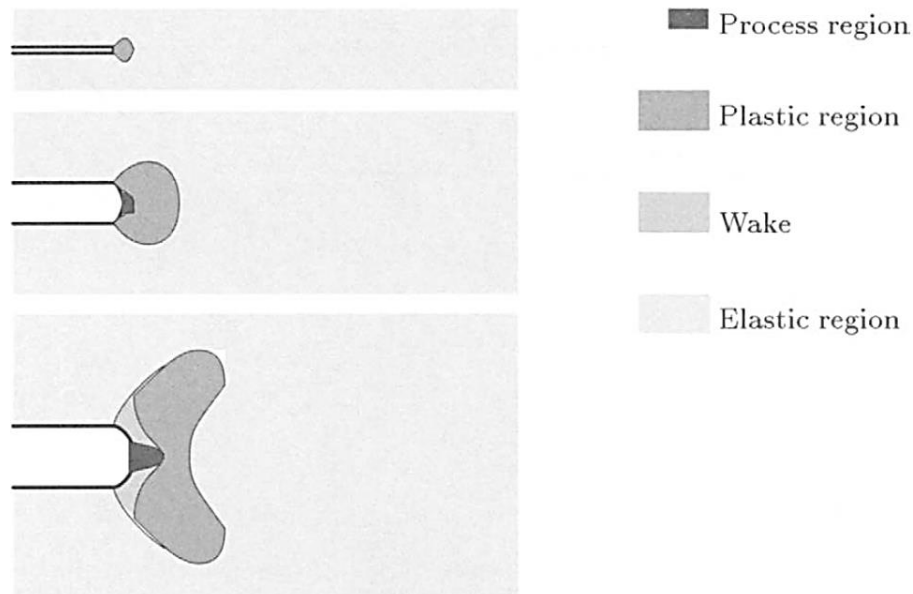


Figure 2.11: Opening of crack and blunting of a sharp crack [10].

The second phase, stable crack growth, begins with the onset of crack growth, which depends on several factors. These factors include material properties, crack and body geometry, load distribution and magnitude, as well as environmental conditions. Time can also be of importance due to viscoplastic flow in and near the process region. During this phase, the size of the plastic region increases due to increased loading of the structure. As the crack growth process moves towards unstable crack growth, the time effects become more and more important. Crack growth in a structure occurs when micro-separations in front of the crack edge merge with the main crack. To detect when this growth occurs is often very difficult. The stable crack growth is usually quite small compared to the crack length. The amount depends on the several factors; material properties, environmental conditions, load and body geometry. The stable crack growth is determined by local conditions at the process region, whilst the onset of unstable crack growth is a result of global instability. The third phase, unstable crack growth, is followed and includes crack growth with high velocity.

The direction of the crack growth in an engineering structure is in a plane normal to the maximum principal stress. For cracks that do not originally coincide with such a plane, there will be a kink and then a smooth adjustment of direction. However, for anisotropic materials the cracks tend to follow planes of material symmetry rather than loading symmetry.

For a crack in a thin plate, a necking region may occur at the crack edge, as depicted in Figure 2.12. The height in the necking region, closest to the crack edge, is approximately equal to the thickness of the plate. For a sufficiently thin plate, the necking region grows continually during loading until complete sliding off occurs. The necking region penetrates deeper

towards the interior of the plate, which can lead to complete slip penetration through the thickness or it can lead to crack growth under incomplete penetration, thus creating shear lips near the surfaces of the plate. Some different scenarios are shown in Figure 2.13. Furthermore, the necking region can be considered to be a geometry related process region, whilst the process region relating to micro-separations is a material related process region. For a thicker plate, the deformation will be different; a material related process region is formed in the interior of the plate, whilst at the surface, a geometry related process region is formed. For this type of case, the growth starts earlier in the interior of the plate than at the surface, which creates a curved crack edge, also known as “thumbnail” or “tunneling” effect. Thus, conclusions drawn from cracks visible on the surface of a body can be misleading.



Figure 2.12: A schematic representation of the formation of necking in a thin sheet [10].

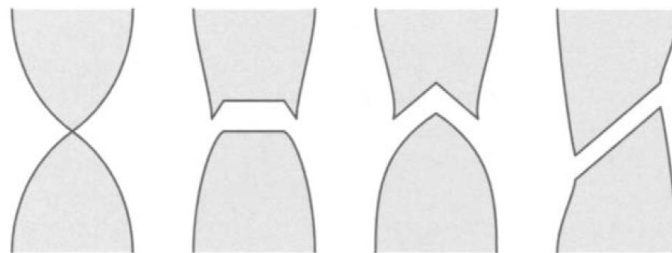


Figure 2.13: Examples of penetrations; to the left: complete slip penetration, the two in the middle: shear lip formation, to the right: asymmetric cross-sectional slip [10].

For fractures, there is also a temperature dependence. At sufficiently low temperatures, below the nil ductility temperature, the fracture surface is flat and runs straight across the plate. Whilst, above a sufficiently high temperature, the upper shelf, the fracture surface is typically slanted or showing pronounced shear lips. For the temperature region in between, the brittle-ductile temperature transition region, the fracture surface generally shows some degree of shear-lips [10].

### 2.3.1 Fracture Mechanics and Damage Behavior of Polymers

As the use of polymeric materials has increased in structural applications, so has the need for understanding the fracture mechanical behavior of polymers. Polymers experience highly strain rate sensitive mechanical behavior, as mentioned earlier in section 2.1.2. Therefore, the fracture mechanics of polymers is highly dependent on time and the fracture mechanics methodology developed for metals is not directly transferable [11].

For polymers, the plastic deformation occurs by molecules sliding as well as being disentangled and stretched. This is possible due to the weaker bonds between molecular



chains than between the atoms in the molecule. Thus, the micro-separation, which leads to fracture, occurring in polymers is rupture and disentangling of molecules. The nucleation sites for micro-separation can be crystalline regions, flaws, holes, inclusion and more [10].

For polymers, yield occurs either by shear yielding or crazing. The dominating mechanism depends on the molecular structure, stress state and temperature. Shear yielding are molecules sliding with respect to one another when subjected to a sufficiently large shear stress. For glassy polymers, tensile loading often leads to yield by crazing, which on the macroscopic level appears as a stress-whitened region. Crazing involves molecular chains, that at high strains align in packets referred to as fibrils, resulting in voids, as can be seen in Figure 2.14. Fracture occurs when the fibrils rupture [11]. Williams et al. studied the relationship between fracture behavior and temperature for polymers. The temperature dependence of fracture behavior for HDPE is shown in Figure 2.15 [5].

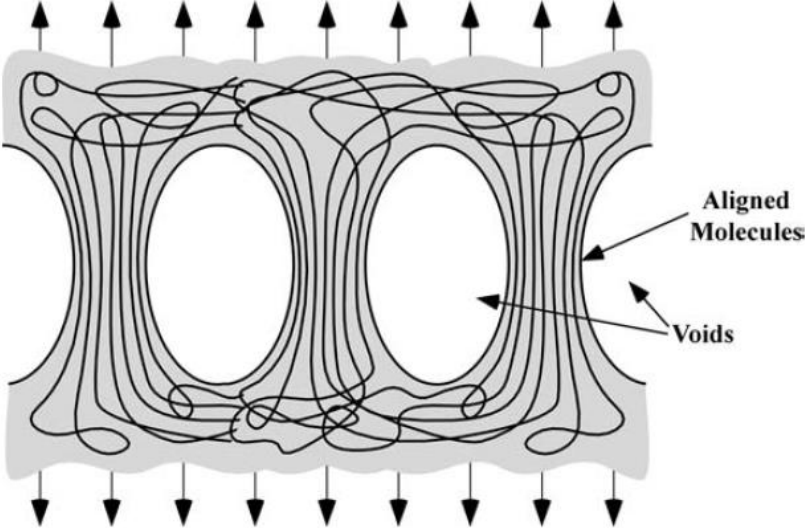


Figure 2.14: Crazing in glassy polymers, voids forming between fibrils [11].

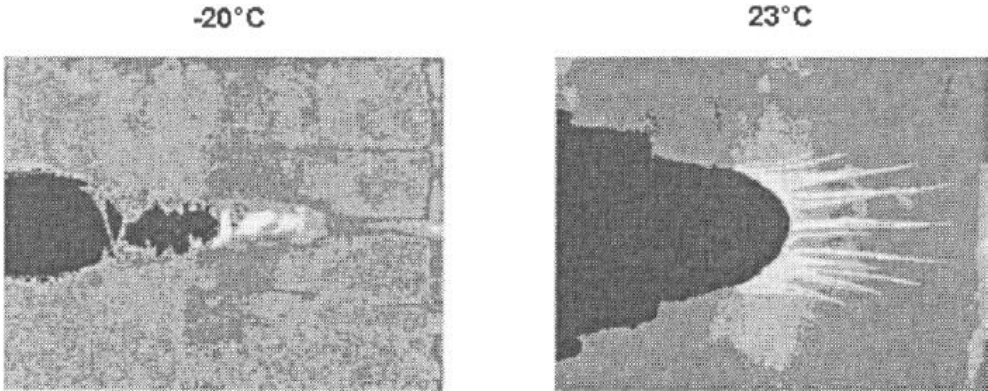


Figure 2.15: Crack tip in a fracture mechanical test specimen of HDPE after deformation. At -20°C crazing occurs, whilst at 23°C there is blunting [12].

## 2.4 Tensile Testing

One of the most common methods of testing to obtain stress-strain data is in tension. For tensile testing, the test specimen is mounted by its ends. The test specimen is continuously deformed by elongating the test specimen at a constant rate. The test is usually conducted until fracture, with a gradually increasing deformation applied uniaxially along the long axis of the test specimen. The resulting force as a function of deformation is measured during the test, from which stress-strain data can be obtained.

From the measured force, the stress,  $\sigma$ , can be derived as

$$\sigma = \frac{F}{A_0} \quad (2.1)$$

where  $F$  is the applied force,  $A_0$  is the initial area. From the measured elongation, engineering strain,  $\epsilon$ , is derived as

$$\epsilon = \frac{\Delta l}{l_0} \quad (2.2)$$

where  $\Delta l$  is difference in length between the initial length and the instantaneous length and  $l_0$  is the initial length.

The test specimens usually have a rectangular or circular cross-section. By the use of engineering stress and engineering strain geometrical factors of the test specimen is reduced, making it possible to compare test specimens with variations in geometry.

As mentioned earlier, section 2.1.2, it is possible to convert the stress-strain curve into true stress-strain curve by taking into account the change of cross-sectional area. Thus, the true stress,  $\sigma_T$ , is calculated as

$$\sigma_T = \frac{F}{A_i} \quad (2.3)$$

where  $A_i$  the instantaneous cross-sectional area over which necking is occurring. The true strain is determined as

$$\epsilon_T = \ln \frac{l_i}{l_0} \quad (2.4)$$

where  $l_i$  is the instantaneous length [5].

## 2.5 Virtual Engineering

The virtual engineering section of this master thesis was conducted in Abaqus, which is a software package for finite element analysis. The finite element system includes five parts; Abaqus/Standard, Abaqus/Explicit, Abaqus/CFD, Abaqus/CAE, Abaqus/Viewer and several add-on options. Where, Abaqus/Standard is a general-purpose finite element program, suitable for implicit analysis, for instance static, low-speed dynamic or steady-state transport analyses. Abaqus/Explicit is an explicit dynamics program and is more suited for simulating brief transient dynamic events, where high-speed, nonlinear, transient response dominates the solution. Abaqus/CFD is a computational fluid dynamics program. Abaqus/CAE is in an interactive environment and is used for creating models, submitting analyses, monitoring and diagnosing jobs as well as evaluating results. In Abaqus/Viewer post processing is done [13] [14].

In this section, a description of the material and damage models in Abaqus is presented. Only the models used in this thesis will be presented in detail. For further information on the possible material and damage models to use in Abaqus, the reader is referred to the Abaqus Documentation [14].

### 2.5.1 Material Models in Abaqus

In Abaqus, the material library consists of several material behaviors, including general properties (such as density and material damping), elastic mechanical properties, inelastic (plastic) material properties, thermal properties and more. In this section, the material behavior used in this thesis will be presented, which include general properties along with elastic and inelastic mechanical behavior.

The only general property used is density, which can be defined as a fixed value or a function of temperature and field variables. Regarding the elastic mechanical properties, there are several models in Abaqus, out of which the most simple one is linear elasticity. The linear elastic material model is only valid for small elastic strains and can be specified to be isotropic, orthotropic or anisotropic.

Similarly to the elastic mechanical properties, the inelastic behavior also has several models. Many of the plasticity models have been developed for modeling metals, but are also applied to other materials. Even though different materials can behave in very different ways, the fundamental concepts of plasticity theories are sufficiently general to be applicable to a wide range of materials. In Abaqus, most of the plasticity models are “incremental” theories, in which the mechanical strain rate is divided into an elastic and a plastic part. As most materials exhibit large plastic strains, the input to Abaqus should be given in true stress

$$\sigma_{true} = \sigma_{nom}(1 + \varepsilon_{nom}) \quad (2.5)$$

and logarithmic plastic strain

$$\varepsilon_{ln}^{pl} = \ln(1 + \varepsilon_{nom}) - \frac{\sigma_{true}}{E} \quad (2.6)$$

where  $\sigma_{nom}$  and  $\varepsilon_{nom}$  are the nominal stress and strain, respectively, gained from the uniaxial test and  $E$  is the Young's modulus.

Out of the possible plasticity models to use, in this thesis the one used is the classical metal plasticity model. It uses Mises or Hill yield surfaces with associated plastic flow, perfect plasticity or isotropic hardening behavior and can be used in combination with models of progressive damage and failure. Both Mises and Hill yield surfaces assume the yielding of the material is independent of the equivalent pressure stress. The Mises yield surface is used to define isotropic yielding, by entering the uniaxial yield stress as a function of uniaxial equivalent strain, temperature and/or other field variables. However, for Hill yield surface, anisotropic yielding is possible, by specifying a reference yield stress and a set of yield ratios. Other properties that can be defined include heat generation by plastic work, strain rate dependence, hardening and more. If no hardening is defined, the material is set to be a perfect plastic material, meaning the stress does not change with plastic strain. Furthermore, for Abaqus/Explicit an error tolerance is used to regularize the input data. This regularization value can be defined or is otherwise set to the default value of 0.03 [14].

### 2.5.2 Damage Models in Abaqus

In Abaqus, the specification of a failure mechanism consists of four parts, represented in Figure 2.16. The undamaged material behavior is that represented by the points a-b-c-d'. In the initial section, a-b, the material response is linear elastic. The following sections are plastic, with plastic yielding and strain hardening, b-c. At point c, the damage is initiated, after which the deformation is localized in a neck region of the test specimen. Due to damage, the material follows the curve of c-d instead of the undamaged response of c-d'. After the point c, there is an evolution of the degradation of the stiffness in the region of strain localization. Consequently, the failure mechanism is specified by defining the undamaged material response, the damage initiation criterion, the damage evolution law and also if elements should be deleted after the material stiffness is fully degraded (point d).

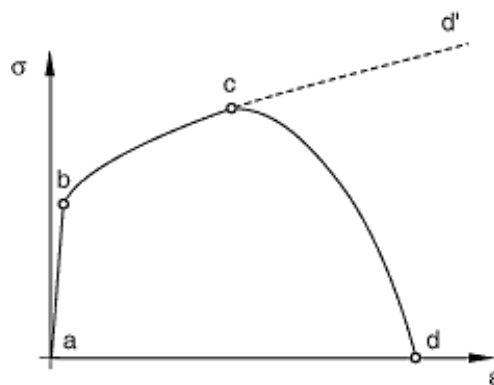


Figure 2.16: Typical stress-strain curve for a uniaxial test of a metal specimen, with regions for specifying failure mechanism indicated [14].

In Abaqus, there are three models of how to predict progressive damage and failure. These are:

- Progressive damage and failure for ductile metals
- Progressive damage and failure for fiber-reinforced materials
- Progressive damage and failure for ductile materials in low-cycle fatigue analysis

For this thesis, the most suitable model to use is the one for ductile metals and thus the other models will not be presented further. For the model of progressive damage and failure for ductile metals, the damage initiation criterion is divided into two groups:

- Damage initiation criteria for fracture of metals, including ductile and shear criteria
- Damage initiation criteria for the necking instability of sheet metal.

Out of these two, the one utilized in this thesis is the first one; fracture of metals.

For ductile metals, there are two main mechanisms that can cause fracture; ductile fracture due to the nucleation, growth and coalescence of voids and shear fracture due to shear band localization. In Abaqus, the two mechanisms have different initiation criteria. The ductile criterion assumes the equivalent plastic strain at the onset of damage to be a function of triaxiality and strain rate. Whilst, the shear criterion assumes the plastic strain at the onset of damage to be a function of the shear stress ratio and the strain rate.

Regarding the damage evolution, it is based on the damage being characterized by the progressive degradation of the material stiffness, which leads to material failure. The characteristic stress-strain curve with progressive damage degradation is presented in Figure 2.17. In the figure,  $\sigma_{y0}$  and  $\bar{\epsilon}_0^{pl}$  is the yield stress, respectively the equivalent plastic strain at the onset of damage. The damage variable  $D$  reaches 1 at failure, with the corresponding equivalent plastic strain at failure,  $\bar{\epsilon}_f^{pl}$ . The undamaged stress is presented as  $\bar{\sigma}$ . For an elastic-plastic material with isotropic hardening, the damage results in softening of the yield stress and degradation of elasticity.

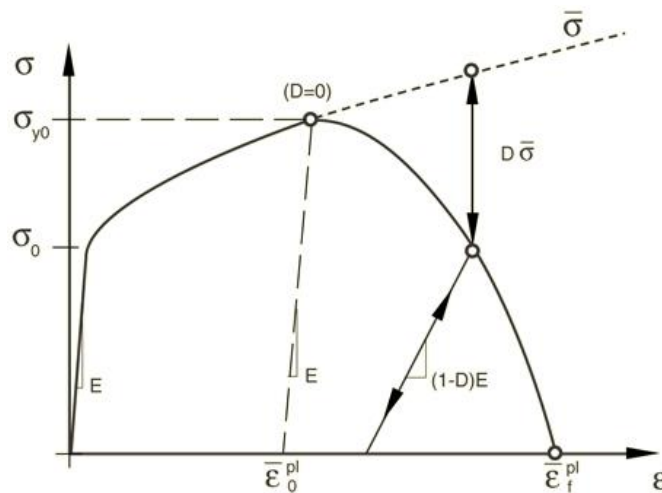


Figure 2.17: Stress-strain curve with progressive damage degradation, solid line being damage response whilst dashed line is without damage [14].

The damage evolution is driven by mesh-independent measures; either plastic displacement or physical energy dissipation. However, when material damage occurs, the stress-strain relationship cannot accurately represent the material behavior, otherwise leading to strong mesh dependency. Therefore, the damage evolution law is in Abaqus specified in terms of equivalent plastic displacement or as fracture energy dissipation, both of which reduce the mesh dependency, though do not eliminate it. The evolution of damage, based on effective plastic displacement, can in Abaqus be defined in three different ways: linear, tabular, or exponential. For fracture energy dissipation, linear and exponential is possible [14].

## 2.6 Scanning Electron Microscopy

With scanning electron microscopy (SEM), it is possible to get images of higher performance than with light microscopy. SEM offers higher resolution and larger depth of field, which makes it possible to see very small features and at the same time features of different heights can be in focus. The microscope consists of an electron column, a sample chamber, detectors and a viewing system. These sections further on include several parts, as shown in Figure 2.18. In the electron column, there is an electron gun, which generates a beam of electrons and accelerates the electrons down the column, towards the sample. The beam is focused using apertures and magnetic lenses as it passes through the column. Towards the end of the column, the beam is deflected by a set of scan coils, creating a scanning pattern over the sample surface. The last lens in the column focuses the beam into a small spot on the sample surface. Thereafter, the beam enters the sample chamber and penetrates the sample.

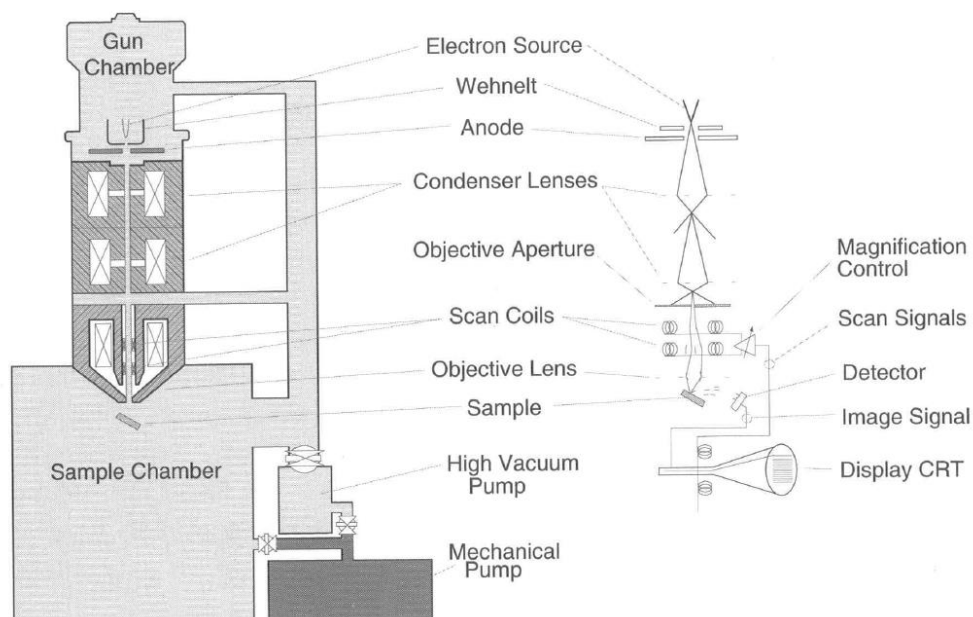


Figure 2.18: Schematic illustration of a SEM [15].

There is a variety of signals being created when the electron beam interacts with sample, as can be seen in Figure 2.19. Out of these signals, the most commonly used ones are secondary electron beam, backscattered electron beam and characteristic X-rays. The different signals offers different information; secondary electrons offers information on surface topography and give the best spatial resolution, X-rays give information on sample composition but have poor spatial resolution and backscattered electrons is mix of both, offering a medium resolution image and giving some, but not specific, compositional information.

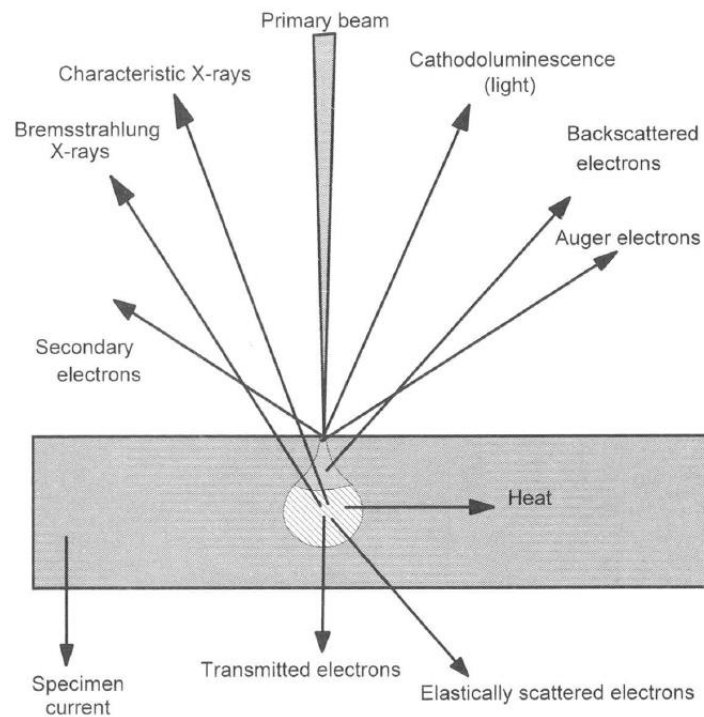


Figure 2.19: Signals generated by interaction between electron beam and sample [15].

For SEM, unlike optical microscopy, no real image is constructed. The images created are virtual images constructed from signals emitted by the sample. By scanning the sample surface in a rectangular pattern, the beam moves from point to point, creating a variation in signal strength that reflects the differences in the sample. From the output signal, a virtual image is then constructed [15].



## 2.7 Digital Image Correlation

Digital Image Correlation (DIC) is a full-field optical technique which is extensively used in experimental mechanics. DIC can provide information about the full-field displacements and strains by comparing the images of a sample before and after deformation or during the deformation process. There are different types of DIC; 2D and 3D. For 2D DIC one camera is used to acquire the images, a typical set-up is shown in Figure 2.20. For 2D DIC to be applicable there needs to be no out-of-plane deformation of the sample which also needs to be planar. If there is out-of-plane deformation or the sample is curved 3D DIC is preferred, which uses two cameras [16].

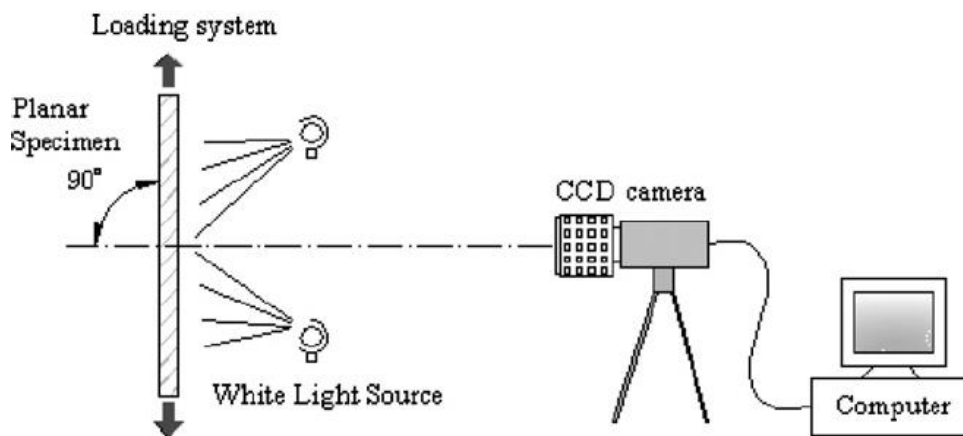


Figure 2.20: Typical set-up for 2D DIC [16].

The different DIC techniques consists of three steps: creating a speckle pattern, image acquisition and image analysis. A speckle pattern is a random intensity distribution on the samples surface. This could be applied for instance by spray-painting or airbrushing but could also be a naturally occurring pattern. The speckle pattern is a carrier of deformation which influences the accuracy and precision of the DIC. The image acquisition is the recording of the surface of the sample at different times during testing, done by one or two cameras. These images are then utilized in the image analysis, where the reference image is compared to the deformed image. To be able to get the displacement and strain fields, a cross-correlation algorithm between the images is used, which depend heavily on the quality of the speckle pattern. The quality of a speckle pattern is increased if the pattern has a highly random and isotropic distribution, high contrast and good adhesion to the sample. Some examples of speckle patterns are shown in Figure 2.21 [17].

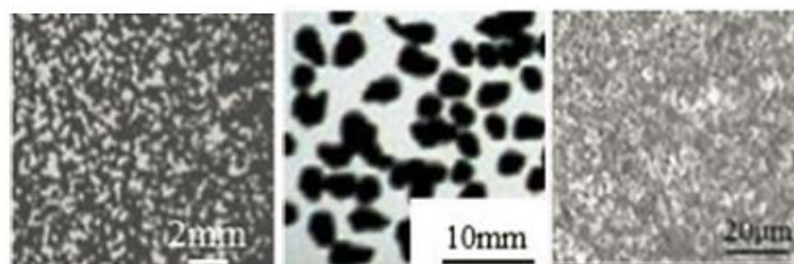


Figure 2.21: Speckle patterns by, from the left spraying, black permanent marker, airbrushing [17].

For 3D surface DIC, stereovision is used, thus making it possible to for any 3D object measure the 3D displacement field and the surface strain field. To get an accurate result, it is important to calibrate the cameras. From a pair of images taken by the cameras the coordinates of physical point can be determined by triangulation. Repeating this process for many points results in a 3D shape of the sample. By having a sequence of pair of stereo images (the two cameras each taking a picture at the same times) the deformation of the sample can be measured. This is done by tracking the displacement of a point in the images of one of the cameras between two times, as illustrated in Figure 2.22. By doing this for several points a 3D displacement field is obtained, from which the strain field can be computed [18].

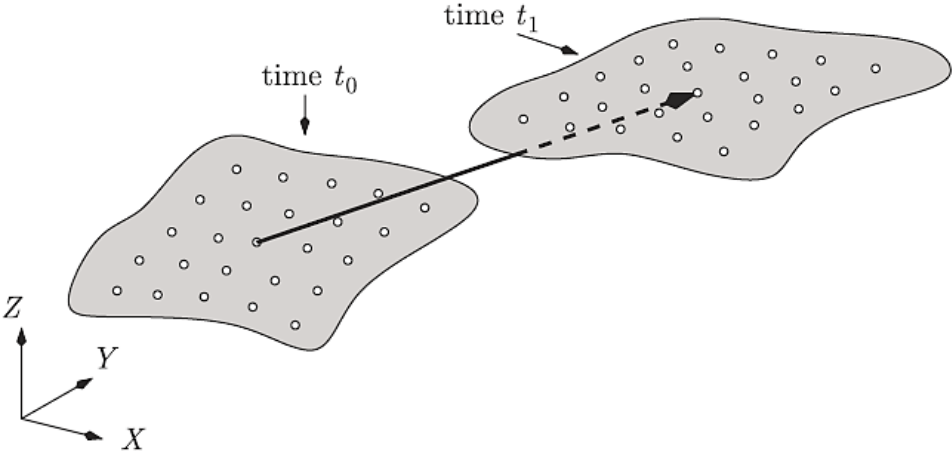


Figure 2.22: Illustration of tracking 3D displacement [18].

## 2.8 Small Angle X-ray Scattering and Wide Angle X-ray Scattering

X-ray diffraction (XRD) or X-ray scattering is a technique where an incoming X-ray beam is directed at a specimen. The beam is then scattered by the electrons within the crystal of the sample, creating a diffraction pattern. The pattern of X-ray intensity is recorded on a detector, where the scattered X-rays in some areas add up constructively and create diffraction peaks. A schematic image of the technique is shown in Figure 2.23. By studying the diffraction pattern, information about the sample's internal structure can be learned [19]. A random structure of the sample, isotropic, will lead to a pattern of equal intensities in concentric circles around the incoming beam. If there is partial orientation, anisotropy, intensity modulations will be present in the pattern. For a sample consisting of a single crystal, there will be intensive spots. Examples of various types of patterns are shown in Figure 2.24 [20].

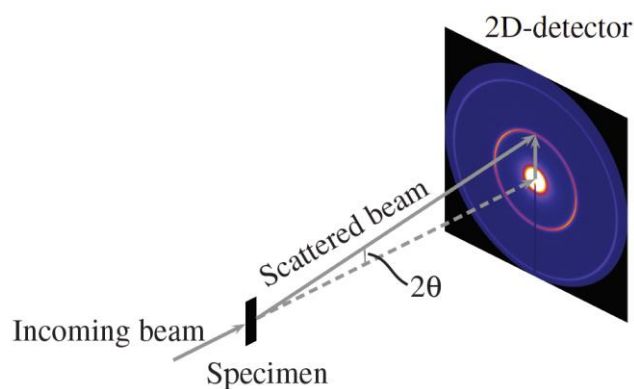


Figure 2.23: Schematic image showing scattering of a beam and the resulting diffraction pattern [21].

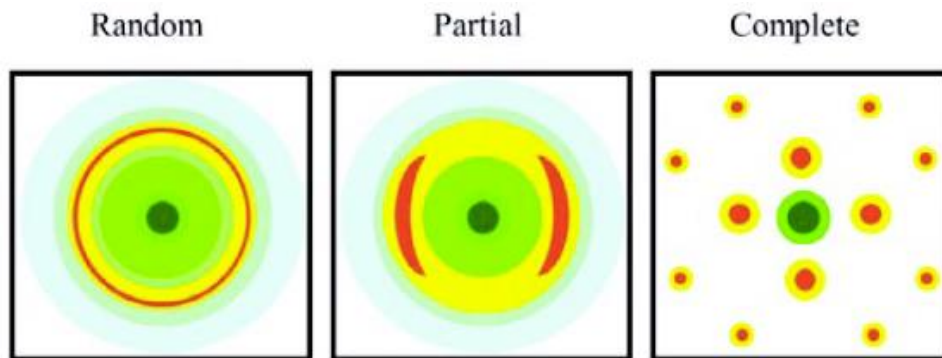


Figure 2.24: Diffraction patterns for an isotropic material, anisotropic material and a single crystal [20].

Both SAXS and WAXS are XRD-techniques. The main difference between SAXS and WAXS is the distance between the sample and the detector, where SAXS has a long distance and WAXS has a short distance. Changing the distance between the sample and the detector makes it possible to study structures of different length-scales. SAXS is used for larger structures, larger than 1 nm, such as the size of crystallites in semi-crystalline polymers, whilst WAXS is used for smaller structure, sub-nanometer scale, for example the intramolecular distance, intermolecular packing or the dimensions of the unit cell [19], [21].

When the incoming beam is scattered in a material, the scattering occurs off the atomic planes in the material, which are separated by a distance  $d$ , as shown in Figure 2.25. Diffraction peaks on the detector are created when the difference in optical path between adjacent X-rays is an integer multiple ( $m$ ) of the wavelength of the X-ray ( $\lambda$ ), thus creating constructive interference. This is what Bragg's law explains, presented in Equation 2.7, where  $\theta$  is the angle of incoming beam above the atomic plane [19].

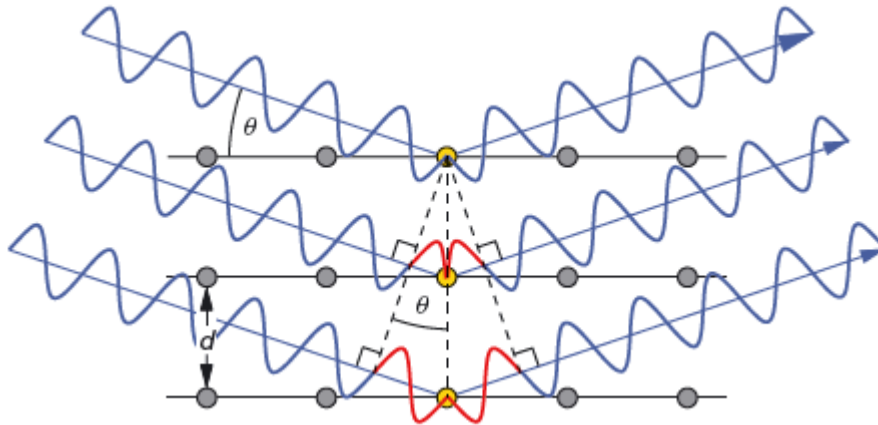


Figure 2.25: Interference of rays elastically scattering off successive atomic planes, separated from each other by a distance  $d$  [19].

$$m\lambda = 2d \sin \theta. \quad (2.7)$$

As previously shown in Figure 2.23, the angle  $2\theta$  is also the scattering angle, between the scattered beam and the incoming beam. From Bragg's law, the scattering vector  $q$  can be defined (for  $m=1$ ) as

$$q = \frac{4\pi}{\lambda} \sin \theta, \quad (2.8)$$

where the scattering vector  $q$  is related to the distance  $d$  as

$$q = \frac{2\pi}{d}. \quad (2.9)$$

The measured scattering can then be presented as intensity as a function of the scattering vector,  $q$  [21].

### 3 Experiments and Results

Experimental tests were performed for two different shapes of test specimens; dogbone samples and edge cracked plates. The dogbone samples were used for tensile testing and SAXS and WAXS. Whilst, the edge cracked plates were used for fracture mechanical testing by the use of tensile loading, including DIC and analysis of the fractured specimen in SEM.

#### Material

The material being studied in this master thesis is a semi-crystalline HDPE polymer with a density of  $0.95 \text{ g/cm}^3$  and a melt-flow index of  $26 \text{ g/10min}$ . To the material 10% pigment masterbatch is added to the mix of granulates of HDPE in the hopper of the injection molding machine. In this application the pigment masterbatch consists of concentrated white pigment (50%) in a carrier polymer of LDPE (50%).

#### Injection Molding

The test specimen used in this thesis were produced by injection molding plates, in the shape previously shown in Figure 1.3. Some of the settings used in the injection molding process is shown in Table 3.1. The volume of material that is injected into the mold is the shot volume. The hold pressure is applied when the degree of filling of the form is 85%, and is applied in two steps.

Table 3.1: Settings used in the injection molding process.

Parameter	Value	Unit
Melt temperature	260	°C
Nozzle temperature	255	°C
Mold temperature	60	°C
Shot volume	11	ccm
Hold pressure 1	1000	bar
Hold pressure 2	750	bar

When the parts have been ejected, the flood gate is cut off. The plates are then weighed and the thickness is measured, which can be seen in Table 3.2. The thickness is measured in two different regions; at the top, close to the injection point and at the bottom, the furthest away from the injection point. All plates have some variation in thickness throughout the plate.

Table 3.2: Weight and thickness of injection molded plates (averaged value).

Dimension	Value	Unit
Weight	4.4	g
Thickness, top	0.59-0.60	mm
Thickness, bottom	0.59-0.61	mm

**Sample preparation**

The geometry of the tensile test specimen (ISO 527-2-1BA), the dogbone sample, is shown in Figure 3.1. The dogbone samples were punched out of the injection molded plate as shown previously in Figure 1.4.

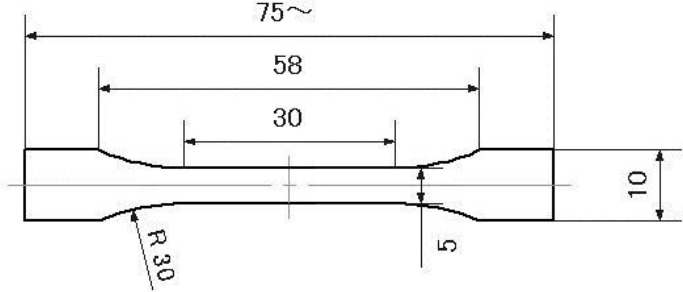


Figure 3.1: Shape of test specimen for tensile testing, dimensions in mm [23].

The sample preparation for the edge cracked plate was performed slightly differently. The test specimens were constructed from the same type of plate as for the tensile tests. The plates were cut through the middle to accommodate for the width of the existing grips for the tensile loader. In Figure 3.2 and Figure 3.3 the test specimen positions on the plate are shown. The dashed red lines indicate where the plate was cut, resulting in from one plate two different test specimens with a crack. The top cut is the same for all test specimens and is the removal of the flood gate from the injection molding process.

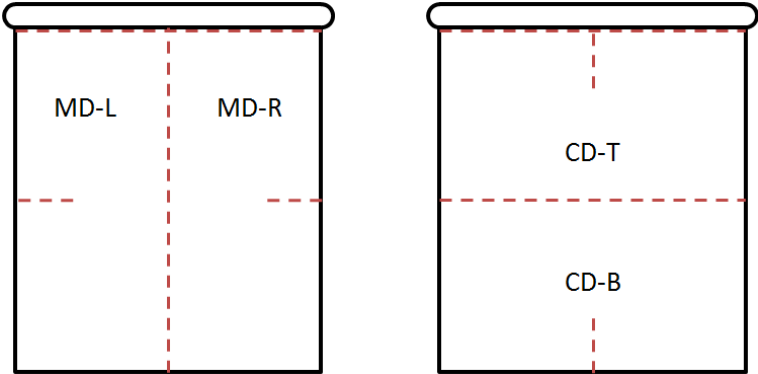


Figure 3.2: Plates with red markings where cuts were made and notations, MD and CD.

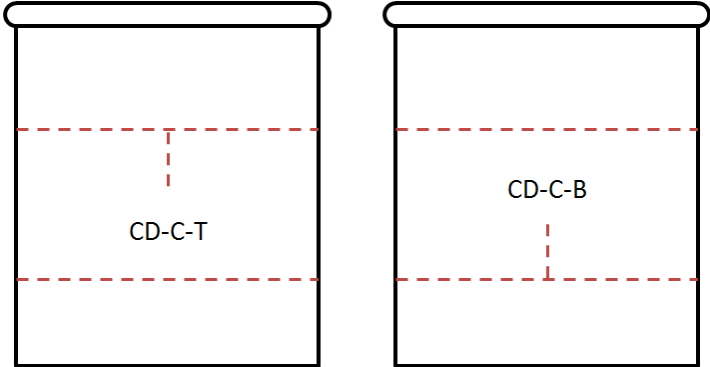


Figure 3.3: Plates with red markings where cuts were made and notations, CD center.

The notations of the test specimens requires further explanation. For the test specimens made from a plate cut in MD, the notation starts with MD and then which half it is; right or left. Thus, a MD test specimen has a crack in CD, from the edge of the plate towards the middle of the plate. Similarly, plates cut in CD give test specimen titled CD and the T or B depending on if it is from the bottom or the top of the plate. Accordingly, CD test specimen has a crack in MD. For the test specimens shown in Figure 3.3, they are cut in CD from the middle of the plate. The last part of the notation stands for where the crack originates, from the top (T) or the bottom (B). Due to the original dimensions of the plate, the width of MD is 40 mm, whilst for CD it is 45 mm.

### 3.1 Dogbone Sample

For the test specimen shaped as a dogbone, tensile testing was performed to be able to use inverse calibration to obtain a material card. To further study anisotropy of the MD specimen, SAXS and WAXS were used for an undeformed specimen and a deformed specimen.

#### 3.1.1 Tensile Testing

The tensile testing was performed by testing 10 specimens in MD and 10 in CD, in the dogbone shape shown previously in Figure 3.1. The tensile tests were performed in the machine Zwick/Roell Z010, with a load cell of 1 kN and an attached climate chamber. By the use of the climate chamber both temperature and humidity is controlled. The tests were performed at a temperature of 23°C and a displacement rate of 100 mm/min, whilst the humidity was uncontrolled and followed the humidity of the ambient environment.

#### Results

From the collected data of the tests, an average curve was constructed. The average curve was constructed by the use of a Python script, where the averaged curve is calculated until the earliest fracture. The resulting force-displacement curves for the 10 tests in MD as well as the calculated average curve are shown in Figure 3.4. From this figure one can determine that there is a good repeatability between the samples, the force-displacement curves show little variation in yield strength and after necking behavior. Also, there is little variation in maximum displacement of the 10 replicates.

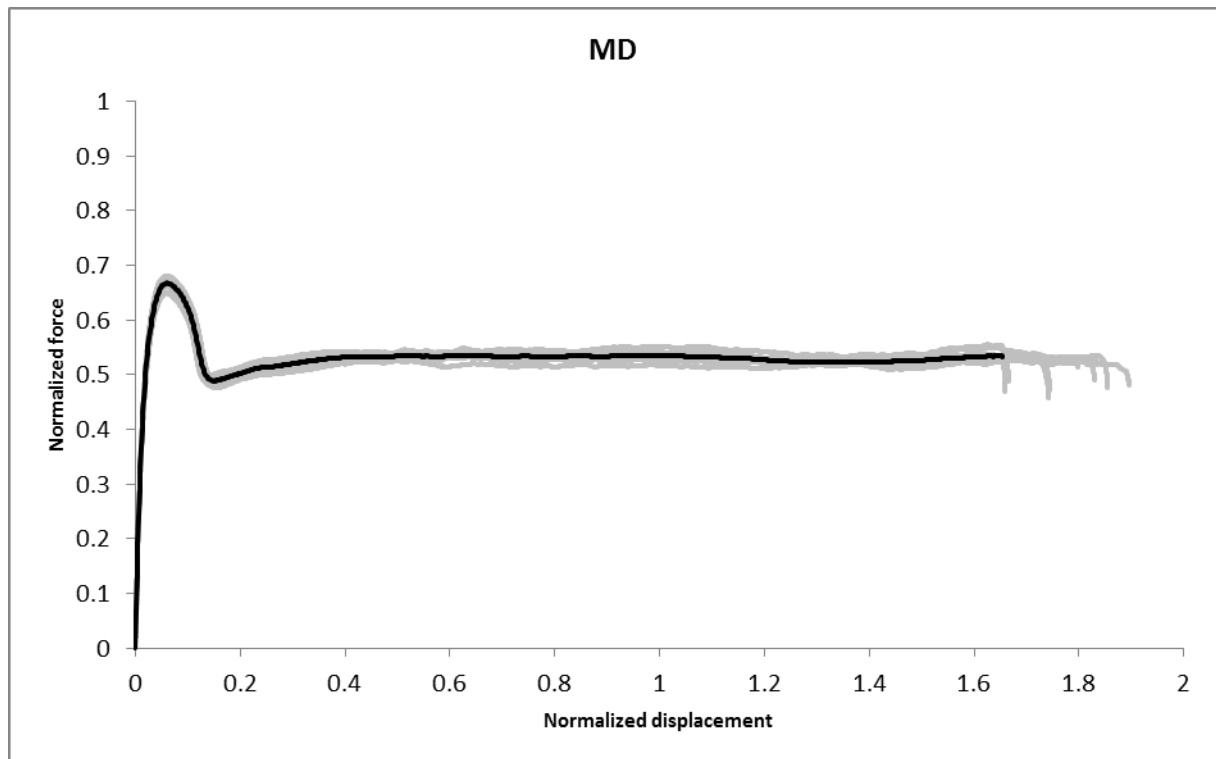


Figure 3.4: Normalized force-displacement curves for MD at 23°C and 100 mm/min.  
Gray are individual tests, black curve is average.



The force-displacement curves for the samples in CD are shown in Figure 3.5, combined with the calculated average curve. For CD there is a similar behavior until fracture occurs, though there is quite a bit of variation in displacement at fracture.

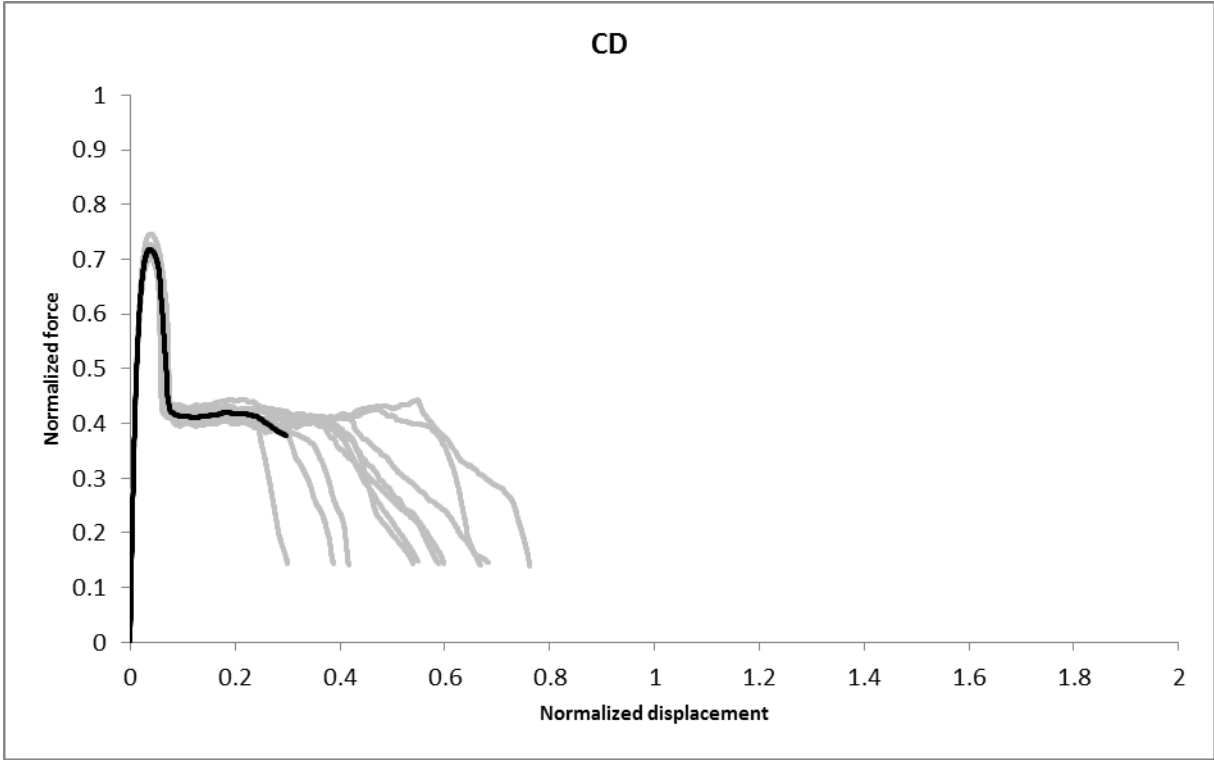


Figure 3.5: Normalized force-displacement curves for CD at 23°C and 100 mm/min. Gray are individual tests, black curve is average.

A comparison of the average curve for MD and CD is shown in Figure 3.6, where also the new average force-displacement curve is compared to the older one, constructed during previous work, as explained in section 1.1.1. From the figure, there is a clear difference shown between MD and CD, where CD has a higher yield strength, whilst MD has a larger displacement at fracture. For both the old and the new tests the same material was used, with the same amount and type of pigment masterbatch. The tests were performed with the same settings at the same temperature. For both cases the tests were performed within a couple of days from the date of injection molding.

There are some differences between the force-displacement curves of the old test and the new. Primarily, the new material exhibits a lower yield strength and a larger displacement at fracture. The difference in material behavior can be due to a number of reasons. Firstly, there could be a difference in the batches of material used in the two tests, even though they should be fairly identical. Secondly, in the injection molding machine some changes have been made. In the old set-up, there was an active needle to flow material into the mold. In the new set-up, the needle has been replaced by a screw. This change resulted in a need to change some settings in the injection molding process. Furthermore, the movable mold half has been changed from aluminum to steel, which affects the cooling of the part. Lastly, there can be a difference in time between injection molding and tensile testing.

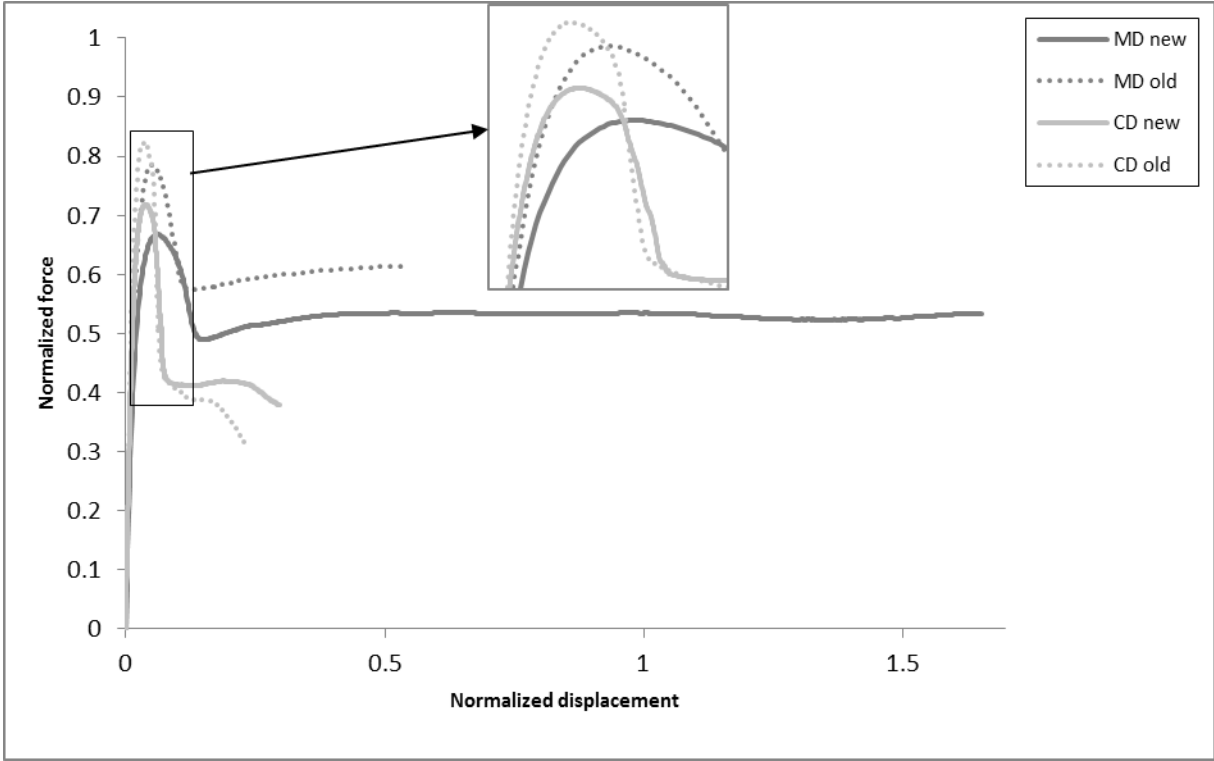


Figure 3.6: Normalized force-displacement curves for old and new tests at 100 mm/min and 23°C. Enlargement of peaks.

### 3.1.2 Small Angle X-ray Scattering and Wide Angle X-ray Scattering

SAXS and WAXS measurements were made at Chalmers, using SAXSLAB MAT:Nordic. Two specimens of MD were studied; one undeformed and one deformed, which had been loaded in tension for a displacement of 40 mm. In Figure 3.7, an illustration of the two specimens for SAXS and WAXS measurement are shown, along with the positions from where data was collected. For the undeformed specimen, three positions were chosen for both SAXS and WAXS. For the deformed dogbone, the distance between the data collection points for WAXS was 1 mm continually. Whilst, for the SAXS measurements the data was collected at the edges of the WAXS region and then focused on the necking transition, where the distance was set to 0.3 mm. The settings used for the different specimens and methods are presented in Table 3.3. A more precise illustration of the data collection points and relating beam size for the deformed specimen is found in Appendix A.

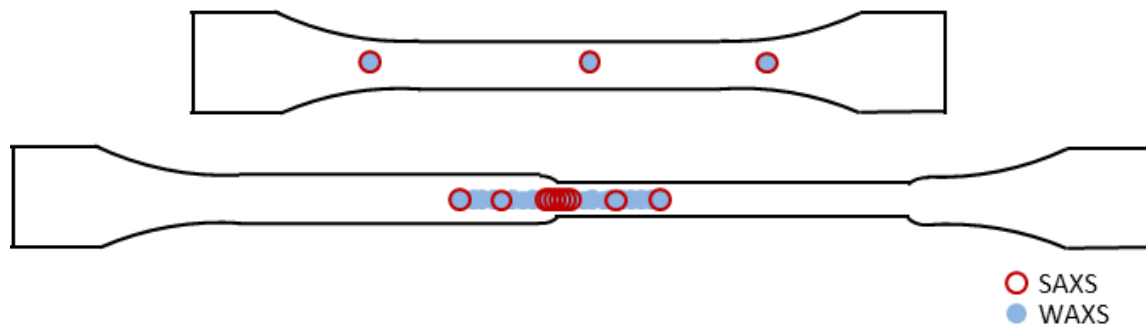


Figure 3.7: Illustration of positions of data collection for undeformed and deformed specimen of MD.

Table 3.3: Settings used for WAXS and SAXS measurements.

	WAXS			SAXS		
	Number of data points	Beam size (mm)	Measurement Time (s)	Number of data points	Beam size (mm)	Measurement Time (s)
<b>Undeformed</b>	3	0.9	180	3	0.3	300
<b>Deformed</b>	21	0.9	180	12	0.3	300

### Results

In the following section, the results of the SAXS and WAXS measurements are presented. Important to note is that no consideration is taken into variations in thickness. Thus the amplitude of the intensity curve is not to be compared between points of different thickness without caution. Also, the beam size impacts the result, in the way that the result presented is an average for the area measured by the beam. Furthermore, there is some amount of noise present, especially for SAXS, which is the result of a trade-off between measurement time and noise.

### Undeformed

The WAXS data collected for the undeformed sample is shown in Figure 3.8. The three positions in the material, where data was collected, show little to no variation. However, in each point the scattering pattern shows asymmetry. A higher intensity is found on the right and left side for the second circle, perpendicular to the length of the sample, which corresponds to an orientation of the material parallel to the length of the sample. Unfortunately, all data was not able to fit on the detector and therefore some parts of the circles are unknown. In the intensity plot, four peaks are present at  $q = 1.5 \text{ \AA}^{-1}$ ,  $q = 1.7 \text{ \AA}^{-1}$ ,  $q = 1.9 \text{ \AA}^{-1}$  and  $q = 2.1 \text{ \AA}^{-1}$ . From these peaks d-spacing can be calculated by the use of Equation 2.9. The corresponding values are  $d = 0.41 \text{ nm}$ ,  $d = 0.37 \text{ nm}$ ,  $d = 0.32 \text{ nm}$  and  $d = 0.30 \text{ nm}$ .

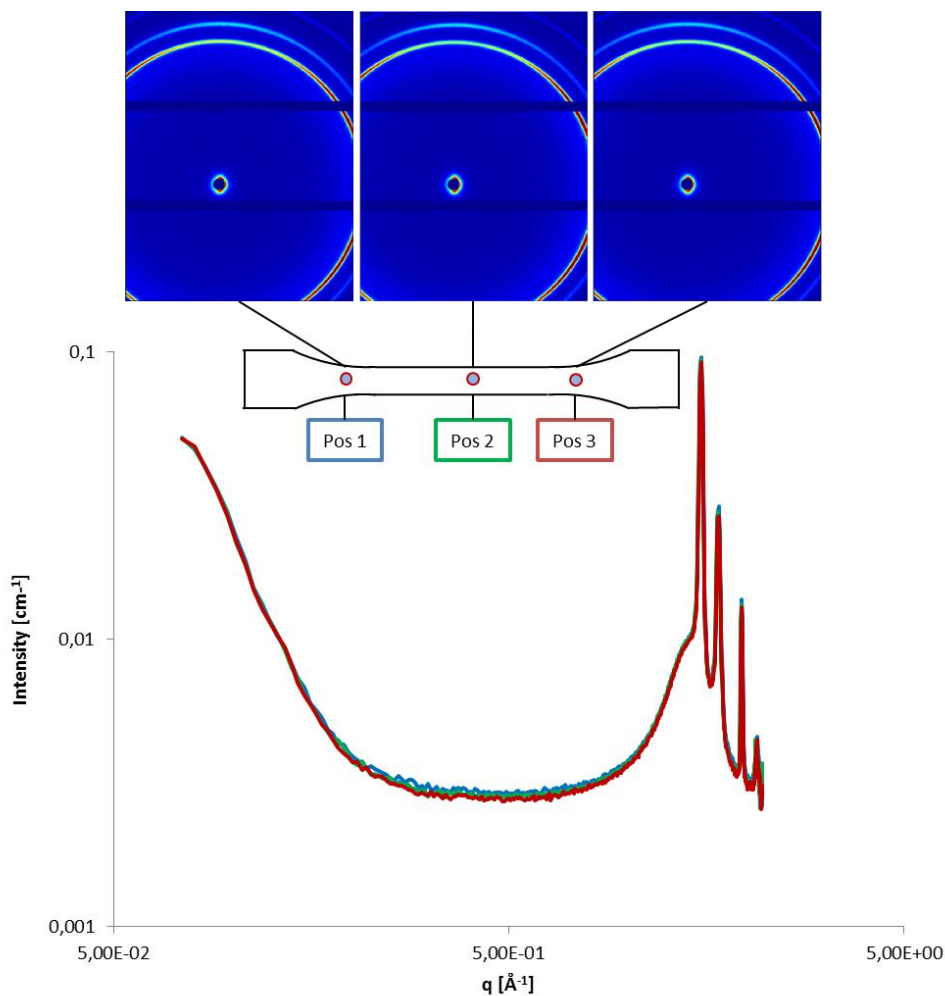


Figure 3.8: WAXS for undeformed specimen. Scattering patterns and plot of averaged intensity over azimuth for all positions.

In similar ways, the result from the SAXS measurements show little variation between the positions, as shown in Figure 3.9. Also, there is asymmetric scattering, indicating orientation in the sample. In the intensity plot, there is a broad peak at  $q = 0.042 \text{ \AA}^{-1}$ , which is followed by noise, making it difficult to detect any further peaks.

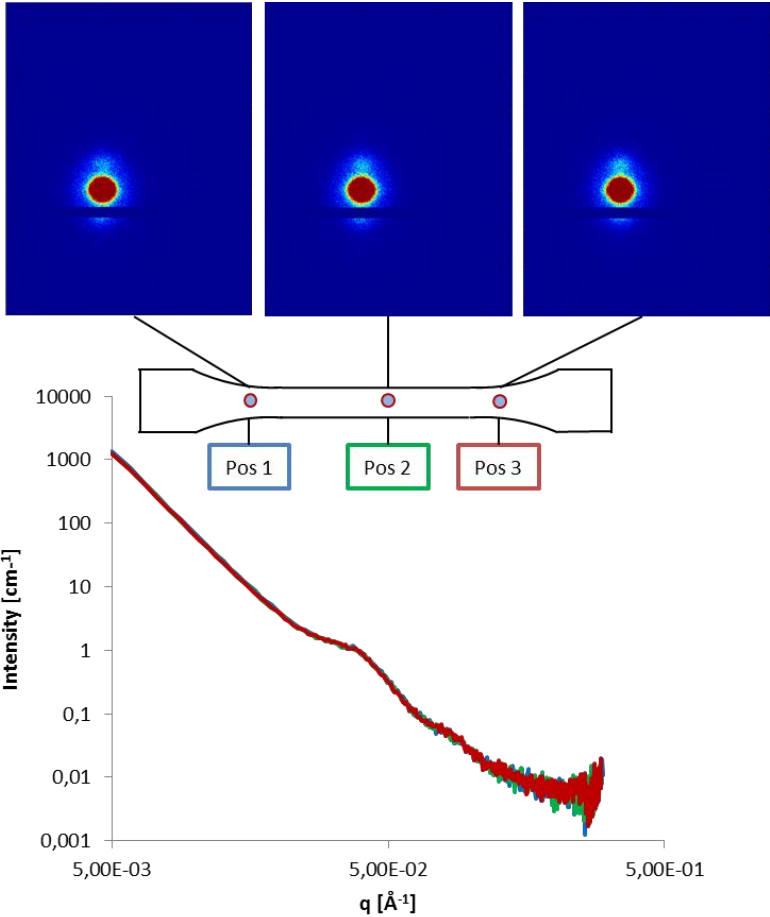


Figure 3.9 SAXS for undeformed specimen. Scattering patterns and plot of averaged intensity over azimuth for all positions.

### Deformed

For the deformed specimen, the results of the WAXS measurements are shown in Figure 3.10. For position A to G, there is no to little variation in scattering patterns and intensity plot, which show some anisotropy. However, for position H which is located on the transitional part to the necked area, the scattering pattern changes and shows more anisotropy, by having an increased intensity perpendicular to the loading direction. In the intensity plot, a new peak is shown to the left of the major peak, at  $q = 1.4 \text{ \AA}^{-1}$ , corresponding to  $d = 0.45 \text{ nm}$ . Furthermore, the intensity plot has dropped significantly, probably mostly due to a decrease in the thickness. However, by comparing the peak intensities, some have decreased more than others, though all of the previous peaks remain. The relative decreased intensity indicates a loss of order. Further on, for position I to U, the intensity plot decreases further and the originally major peak is barely visible. The scattering patterns show an intensity localization to the right, indicating further increase in orientation in the loading direction. A major difficulty for position I to U is that the main intensity seems to be located outside the detector. All of the positions show a sharp peak for the same high value of  $q = 2.0 \text{ \AA}^{-1}$ , corresponding to  $d = 0.32 \text{ nm}$ .

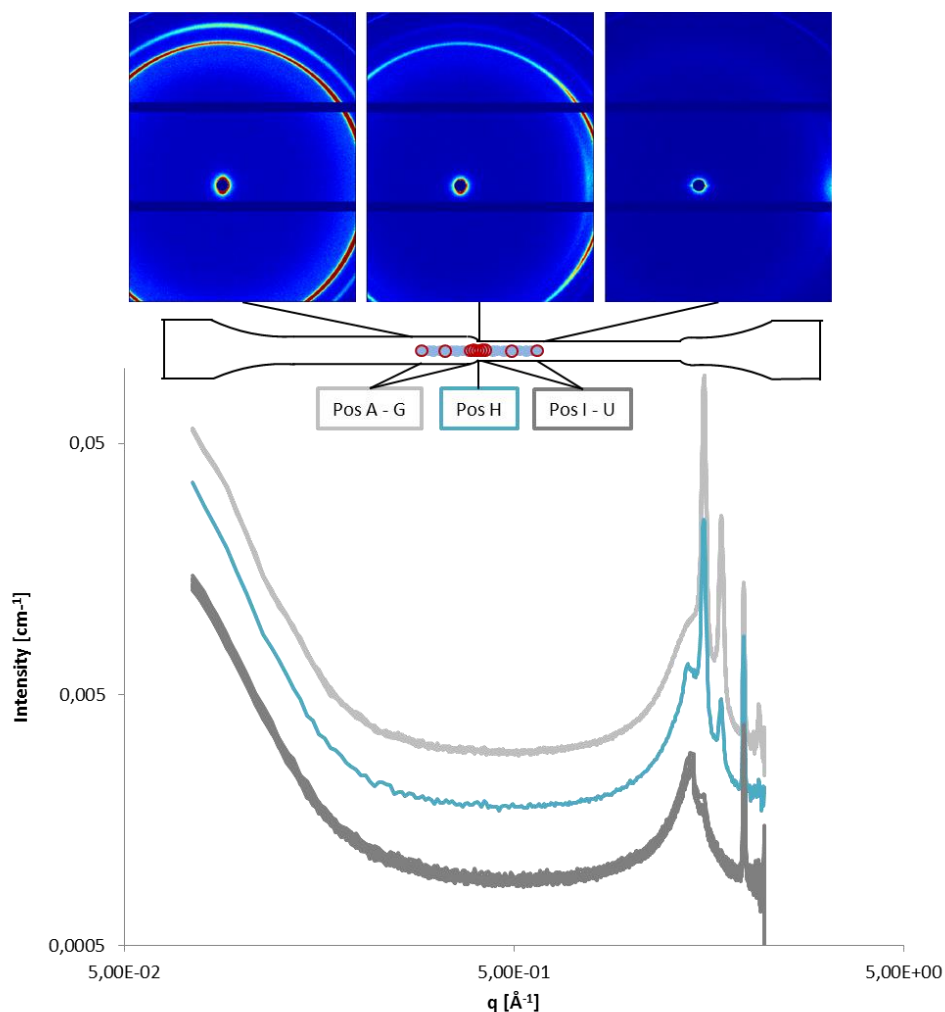


Figure 3.10: WAXS for deformed specimen. Scattering patterns for position A, H and U. Plot of averaged intensity over azimuth for all positions.

Moreover, the SAXS results show similar behavior for sections of positions, as can be seen in Figure 3.11. For position A to D, the scattering pattern has an oval shape in the loading direction and the intensity plot shows a peak at  $q = 0.042 \text{ \AA}^{-1}$ , corresponding to  $d = 15 \text{ nm}$ . Position E is located on the transition to necked region and shows a slightly different scattering pattern and intensity curve, with a less distinct peak. For position F, the scattering pattern is almost completely round and consequently no peak is found on the intensity plot. For position G to L, the scattering pattern has changed into a sharp eye, perpendicular to the loading direction and the intensity plot shows a new peak at  $q = 0.052 \text{ \AA}^{-1}$ , corresponding to  $d = 12 \text{ nm}$ . Thus, there has been a change in the loading direction.

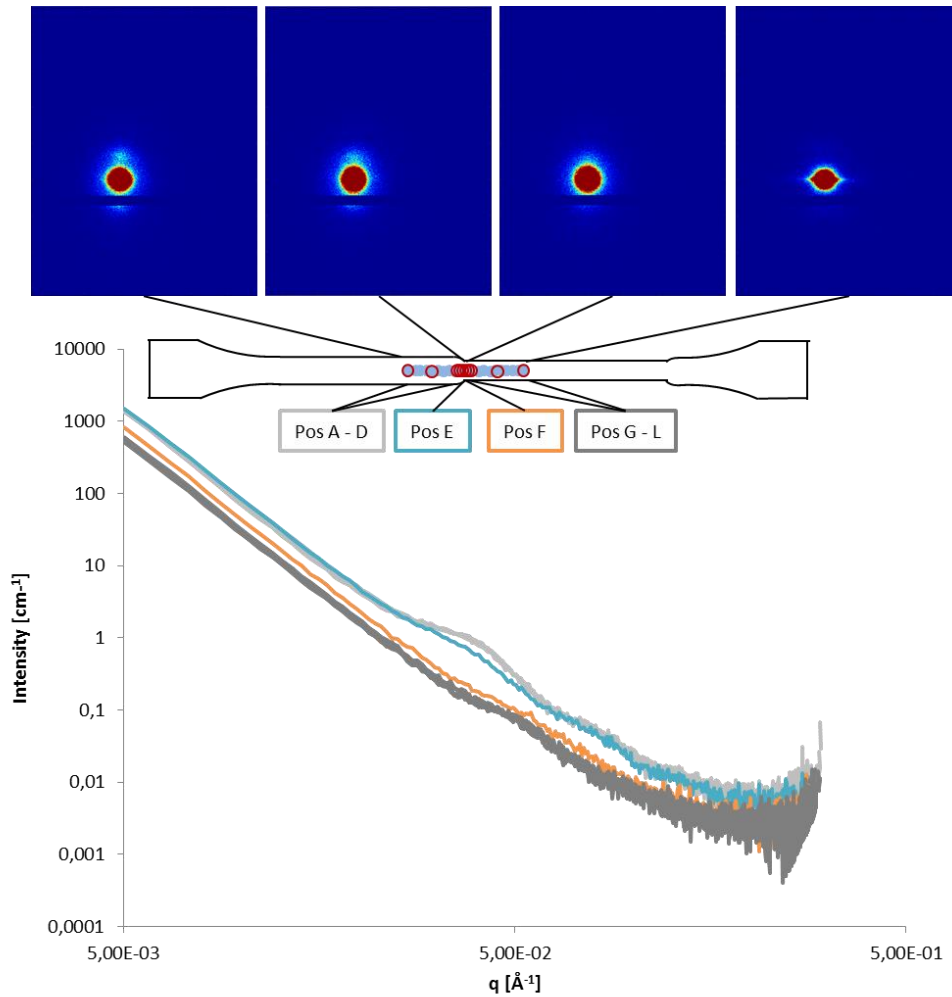


Figure 3.11: SAXS for deformed specimen. Scattering patterns for position A, E, F and L. Plot of averaged intensity over azimuth for all positions.

### Comparison of undeformed and deformed

Note, the intensity scale for the scattering plots in Figure 3.8 and Figure 3.10 are not the same, thus should not be compared directly, without adjusting the scales. However, the intensity curves can be compared to each other as shown in Figure 3.12 and Figure 3.13. From the figures, it can be seen for both WAXS and SAXS, that the region that has not been necked for the deformed sample is the same as the undeformed sample. Therefore, if this area of the sample has deformed, it has done so elastically. Also, since there were some days between deforming and unloading of the specimen and the WAXS and SAXS measurement, relaxation might have occurred.

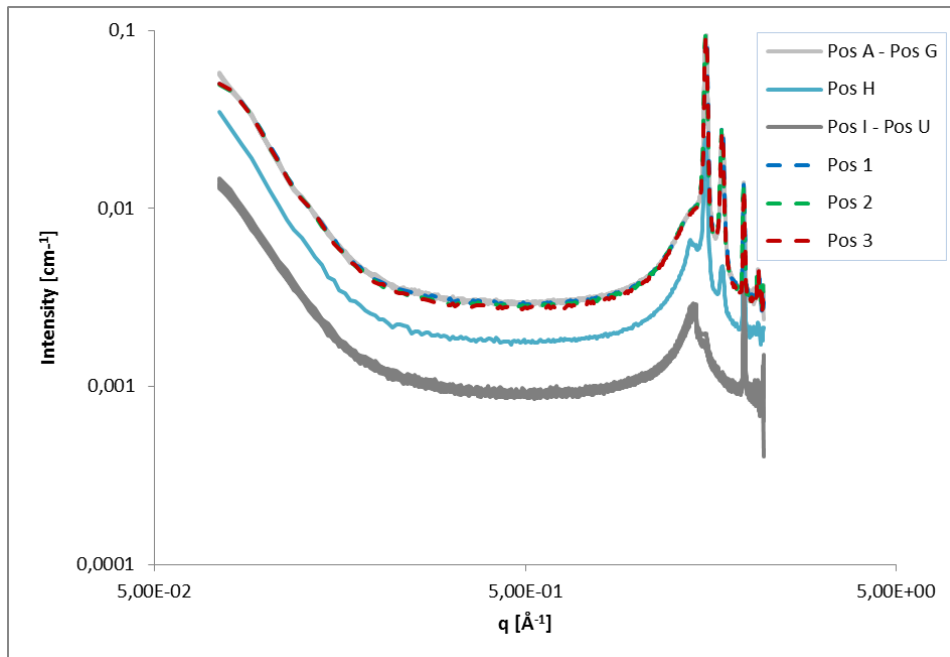


Figure 3.12: WAXS plots for deformed (A-U) and undeformed (I-3) specimen.

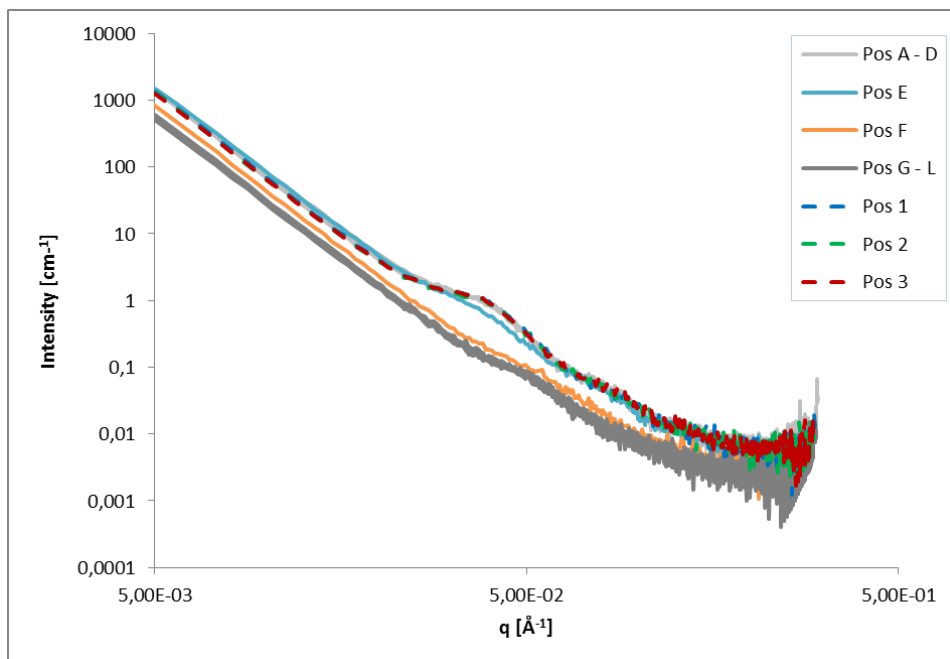


Figure 3.13: SAXS plots for deformed (A-L) and undeformed (1-3) specimen.



## 3.2 Fracture Mechanical Testing

The fracture mechanical testing consisted of tensile testing for various test specimens of plate. Also, the fracture of an MD sample was studied by the use of SEM. Finally, DIC was used during tensile testing of plates in MD-R and CD-T to be able to study the strain fields.

### 3.2.1 Tensile Testing

Tensile testing was done on the test specimen: MD-R, MD-L, CD-T, CD-B, CD-C-T and CD-C-B. The test specimen were loaded in tension, in mode I, at room temperature and humidity. To get a better knowledge of how the test specimen behave and what parameters are of importance, some initial testing was conducted in the same machine as for the dogbones. The tests included variation of:

- Specimen
- Crack length
- Displacement rate
- Distance between grips
- Positioning of grips

The results from the initial test are presented in Appendix B. From the initial test, it was concluded that the behavior depended on test specimen. MD-L and MD-R behave similarly, though MD-L has a slightly higher amplitude. From the tests of MD, it was concluded that there is good repeatability, whilst for CD there was more scattering. CD-B and CD-T have some repeatability. For CD-C-T and CD-C-B, the test showed large variations and no systematic pattern could be found. The rest of the test parameters were only tested on MD-R. An increase of initial crack length will decrease the amplitude of curve, whilst having the same characteristic shape. Increasing the displacement rate will decrease the displacement at fracture and at the same time change the shape of the force-displacement curve. By increasing the distance between the grips (the gauge length) the amplitude of the force-displacement curve decreases. Having the grips centered on the test specimen or towards the crack had no significant effect on the force-displacement curve.

There are some important factors to consider regarding the initial testing; the tests were conducted on a small amount of test specimens, there could have been some variation in geometry tolerance, grip positioning and tightening. Most importantly, it was later on concluded that the grips used during testing did not provide enough fixation and slippage occurred, which has an effect on the tests and makes them more difficult to compare.

The input from the initial testing lead to the following settings for the remaining tests:

- Room temperature and humidity
- Displacement rate of 100 mm/min
- Crack length of 15 mm
- Grips positioned centered and at a distance of 30 mm
- Test specimen MD-R and CD-T

For the application, the displacement rate is higher than the one used in the tests, however, several other aspects were taken into account, such as the limitations of the tensile machine, the amount of noise and comparability with other tests, including material card calibration tests. The crack length was chosen to give enough material left to study the fracture process, whilst still not getting an effect from being too close to the edge of the plate. The two specimen MD-R and CD-T were chosen as they represent the material behavior of the application the most. For the rest of this section, they will be referred to as MD and CD.

Seeing as there was some slippage, a second machine was tested for MD. Furthermore, as test were to be performed at LTH for the DIC, also this machine was tested. Unfortunately, some amount of slippage occurred for all machines. By changing the grips in the machine at LTH, from 25 mm to 40 mm, the amount of slippage could be limited.

**Results**

The results presented in this section are from the test performed on the first machine, at Tetra Pak. The force-displacement curve for MD is shown in Figure 3.14, along with the averaged curve. For MD, the curve is characterized by an initial peak that is followed by a drop in force. On the slope there is a kink, with a change in gradient. The test showed little variation in results, all have the same characteristic shape and similar amplitude.

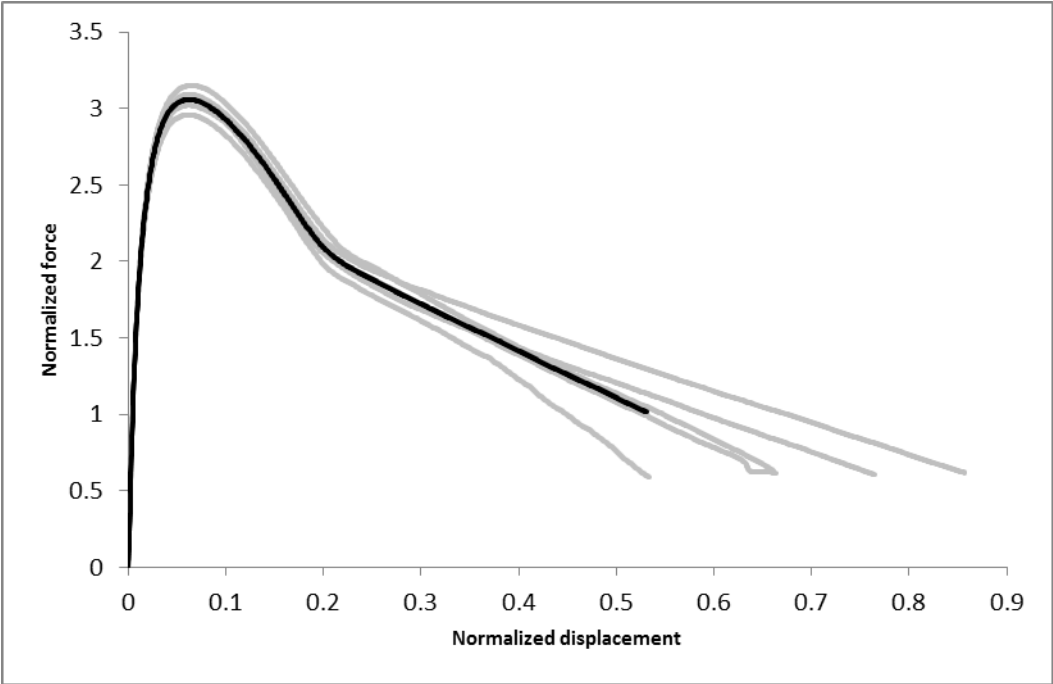


Figure 3.14: Normalized force-displacement curve for MD, average in black.

A fractured sample of MD is shown in Figure 3.15. It shows a highly stretched and necked segment close to the edge of the sample. The crack direction is in a downward angle, towards the edge of the sample. The sample shows asymmetric deformation, with a larger section of the stretched segment above the crack direction than below. Also, the necked region follows, for the top part, the original crack direction. Whilst, for the bottom half, the necked region is in the direction of the crack growth. Some small amount of threads are visible at the bottom fracture surface, which is also more rough than the top surface is. All of the test specimen in MD showed the same deformed shape.



Figure 3.15: Fractured MD sample. Black vertical line indicate original crack edge.

The force-displacement curve for CD is shown in Figure 3.16, where, a scattering of behavior can be seen. In general, most samples show a brittle behavior, where fracture occurs directly after a force peak. However, there is a quite large variation in amplitude. Compared with MD, CD shows less of a repeatability.

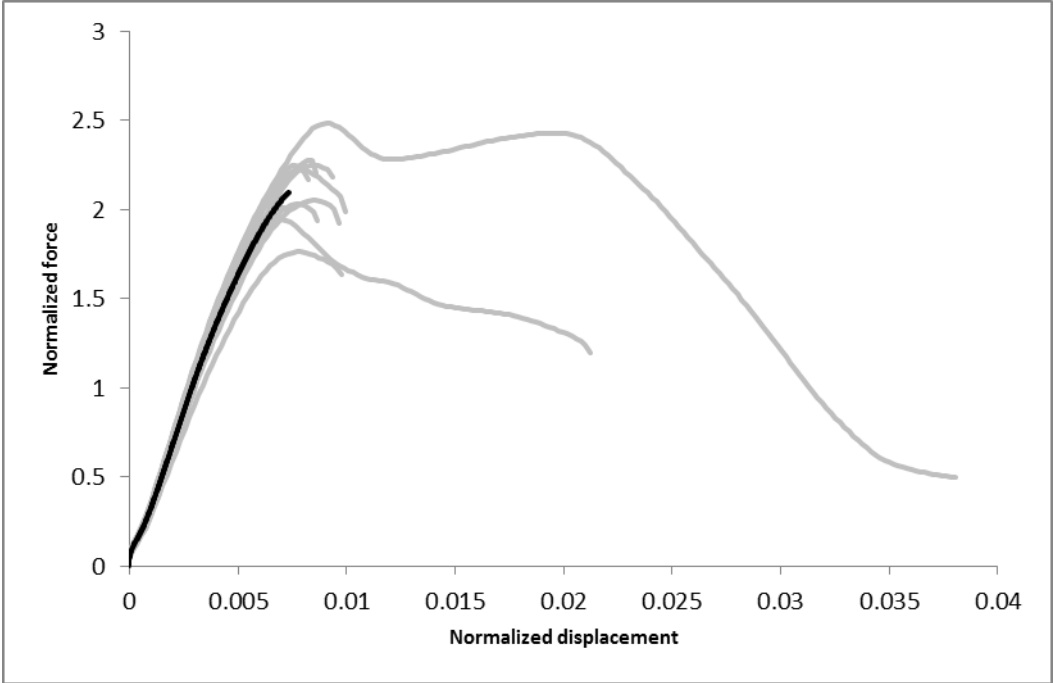


Figure 3.16: Normalized force-displacement curve for CD, average in black.

A fractured sample of CD is shown in Figure 3.17. For CD there is a difference in deformed shape depending on if the sample fractures directly after force peak or is elongated more before fracture. The sample shown in the figure below is representative of those fracturing directly after the force peak. The figure shows a straight direction of the crack growth, following the initial crack direction, leaving a sharp fracture surface with no threads. There seems to be no or little necking.

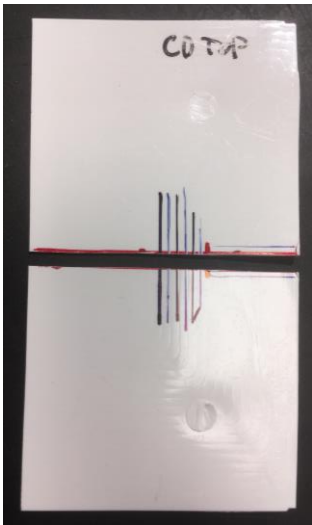


Figure 3.17: Fractured CD sample. Red horizontal line is in the direction of the original crack, vertical red line is original crack edge.

The visual analysis of the fracture samples of MD and CD show significant differences between the two specimen. MD has a much more ductile behavior, whilst CD has a very brittle behavior. A comparison of the average curve for MD and CD is presented in Figure 3.18, and shows how CD is much more brittle and has a higher Young's modulus than MD. When comparing the force-displacement curves of the two different types of test specimens, MD and CD, it is important to take into consideration the difference in geometry; CD is wider than MD. For both MD and CD, the grips did not provide enough friction, which impacts the results. To get a better understanding of what is the material behavior and the repeatability, better grips would be needed. A variation in results can also be due to differences in sample geometry and positioning in the machine.

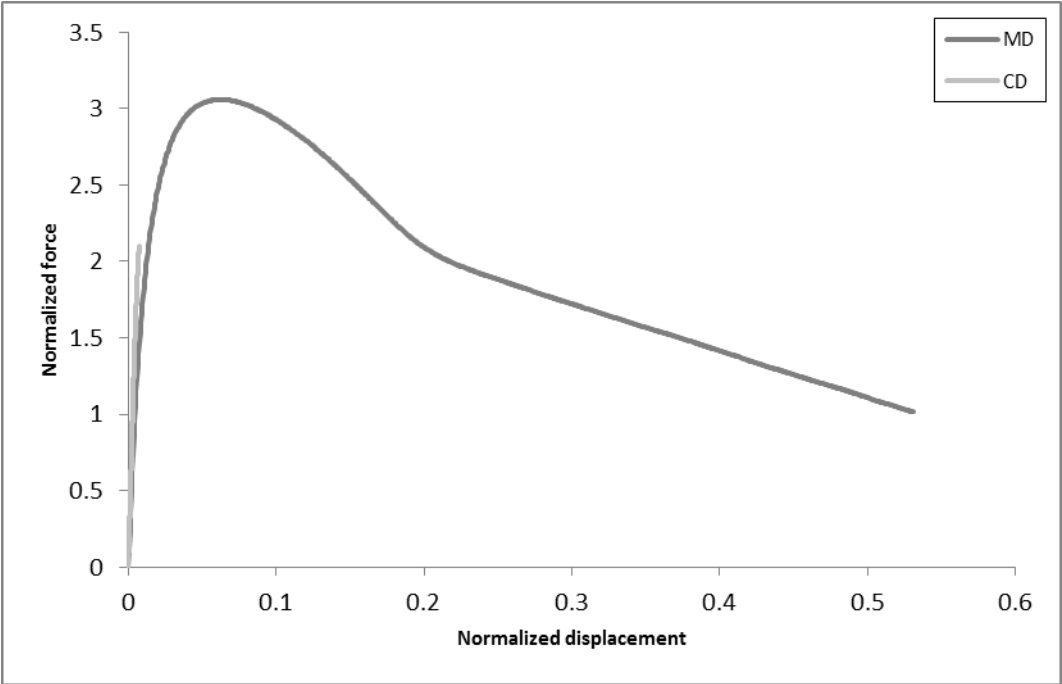


Figure 3.18: Normalized averaged force-displacement curves for MD and CD.

### 3.2.2 Scanning Electron Microscopy

To further investigate the fracture of MD, SEM was utilized. Due to time limitations, only one sample was studied. The section of the fractured sample studied, is shown in Figure 3.19. The microscope used has a BSE detector.



Figure 3.19: Section of fractured MD sample studied in SEM.

### Results

In this section some of the SEM-images are shown, more images can be found in Appendix C. In Figure 3.20, two cracks are present, both were perpendicular to original crack direction. The lines on the surface are likely due to the mixed in pigment masterbatch, showing the flow direction and thus the orientation of the material. As can be seen in the image, the crack is in the same direction, thus implying a dependency of polymer orientation. Moreover, in Figure 3.20, as well as Figure 3.21 and Figure 3.22, one can see delamination and the skin layer been peeled off, exposing the underlying layers. The different layers through the thickness have different behavior. Furthermore, in Figure 3.20 and Figure 3.22, fiber-like structure is shown below the skin layer.

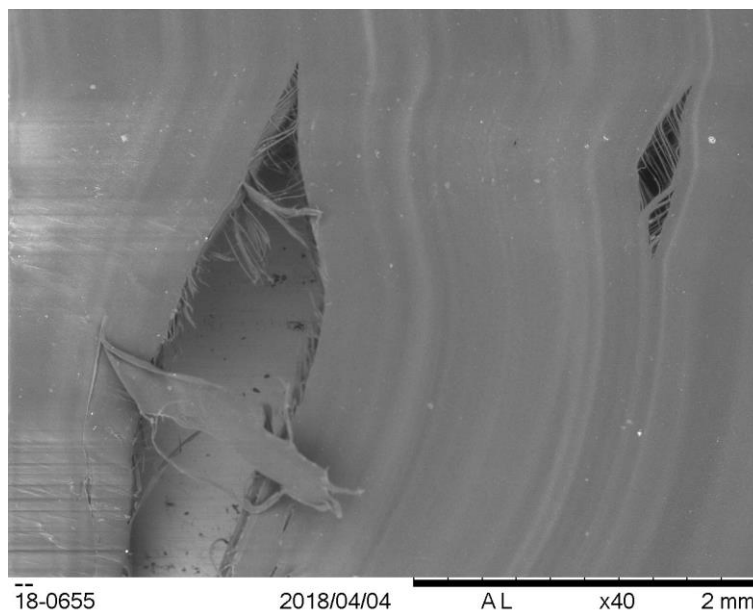


Figure 3.20: SEM-image of MD sample. Showing delamination of top layer and two cracks, perpendicular to the original crack direction, with fiber-like structure in the cracks.

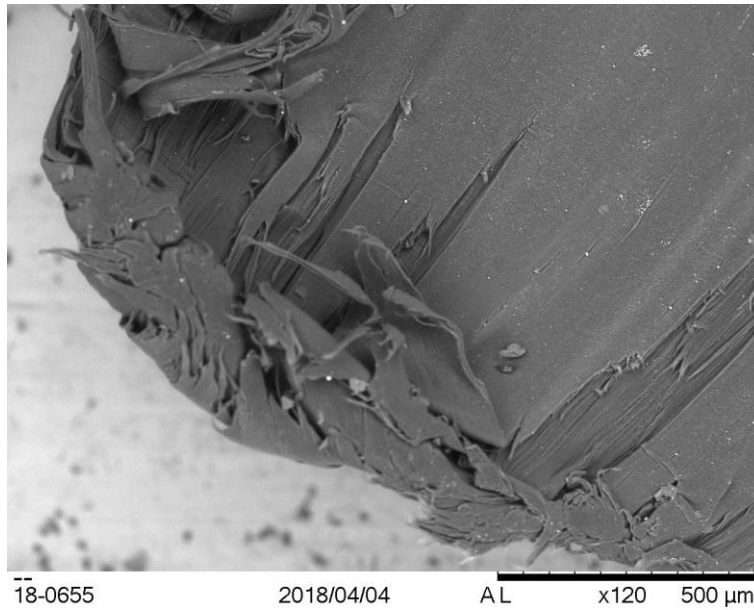


Figure 3.21: SEM-image of MD sample. Showing fracture surface, including delamination.

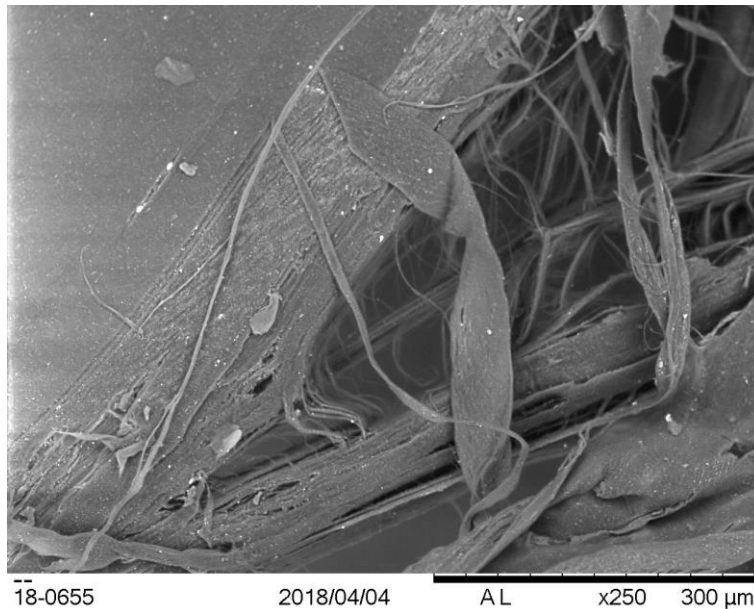
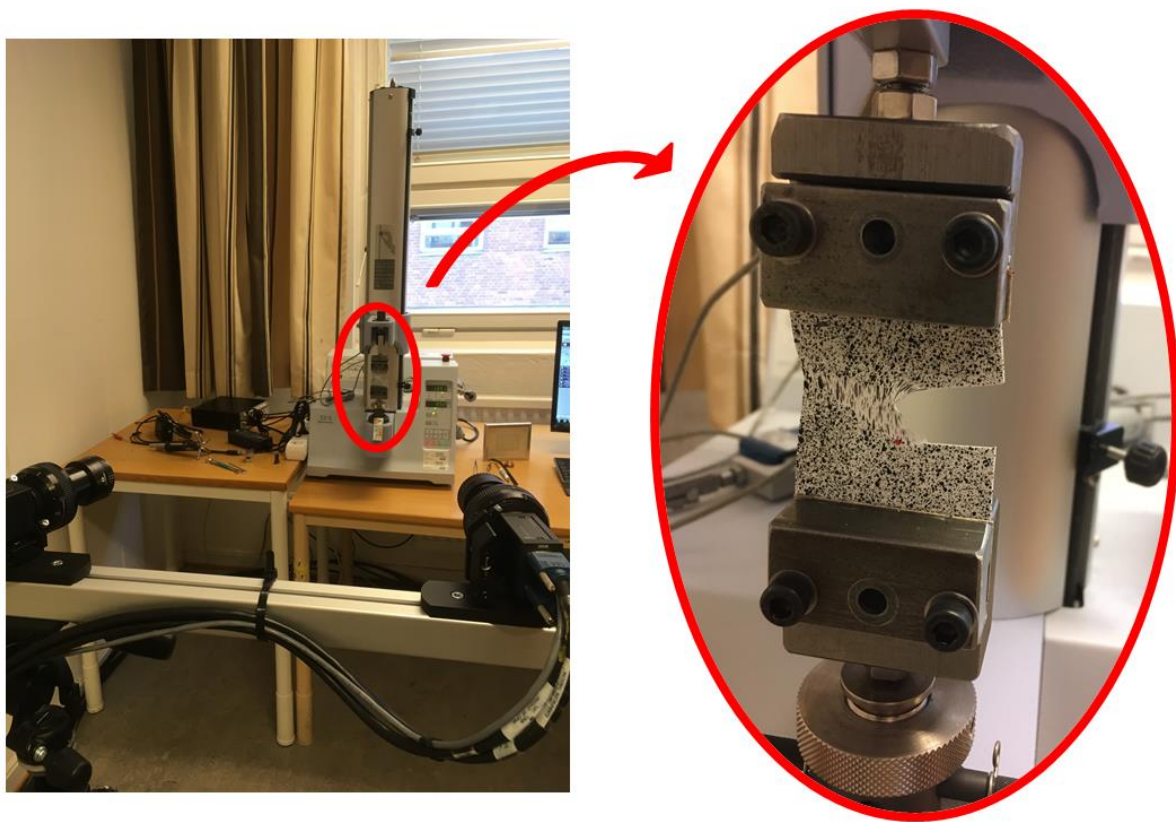


Figure 3.22: SEM-image of MD sample. Showing delamination of top layer and exposing fiber-like structure.

From the SEM-images, one can see how the skin layer has been delaminated from the rest. However, it is difficult to see if there has been any delamination of the shear layer and the bulk. Also, from the SEM, it is not possible to see when each layer fractured.

### 3.2.3 Digital Image Correlation

In this thesis, DIC analysis was performed on samples of MD-R and CD-T. For simplicity, the samples will here be noted MD and CD. The DIC experiments were performed at LTH. The set-up for the experiments, including the two cameras, is shown in Figure 3.23. The light source used was the ceiling lamp as well as the light coming in through the window. The speckle pattern on the samples was applied by spraying on black paint. In the tests, a Shimadzu EZ-S tensile tester was used and tests were filmed by two cameras, Point Grey Gazelle 2.2 with a resolution of 2.2 Megapixels. The force and the displacement was registered in the program TrapeziumX. Vic Snap, a software for acquiring the images was also used for correlating the displacement with the images. Before the images were taken, the exposure time of the cameras was determined. This was maximized without there being any overexposed areas on the samples.



*Figure 3.23: Set-up for DIC. To the right an enlarged image of the test specimen.*

Throughout the test, images were taken by the two cameras. The obtained images were analyzed using the correlation software VIC-3D 7. To enable the image correlation, the camera system needs to be calibrated for stereo-vision. Thereafter, the images are combined and an analysis of the 3D displacements is possible. There are some settings, that first must be determined. To start with, the size of the subset is to be determined, where a subset is a small area of the reference image. A small subset results in a higher resolution, however this can lead to difficulties in finding the correlating area in succeeding images as a subset must be large enough to have a unique variation in gray levels. Also, the distance between the centers of the subset is determined, where overlap of the subsets is possible. Thereupon, the analysis



could be determined to be incremental or not, where an incremental approach means the correlation is performed between the current and the previous image, instead of between the current and the reference image. The choice of an incremental approach can lead to an easier correlation process, however, using this approach the correlation error will be added between the images. Also, in the analysis, one can choose to study all of the captured images or to study every image at a certain interval.

For the DIC experiments in this thesis, an incremental approach and all the images were used, due to the large deformations. The subset was sized to 61 pixels, and the distance between the centers to 7 pixels. The tensile tests were performed at 100 mm/min, with a gauge length of 30 mm and grip width of 40 mm. The lower grip was fixed and the displacement was regulated by the upper grip.

**Results**

The collected force-displacement data from the tensile loader is shown in Figure 3.24. From the graph, it is possible to see that there is little difference between the MD test specimens. All of the three curves have the same characteristics of an initial peak, followed by a slope with a kink in it. Thus the repeatability of the MD specimens is high, as shown earlier. Due to this, DIC-analysis is only necessary for one sample, here chosen to be MD8. Regarding the CD test specimens, there is quite some differences for the three specimen. Out of the three, two of them hit an initial peak and thereafter the force drops drastically. The third one fractures before a force peak could be identified. Of the two with a force peak, there is a large difference in amplitude. Therefore, it is difficult to make general description of how CD test specimens behave. To show an example of how CD test specimens behave, the test denoted as CD2 is presented in this report.

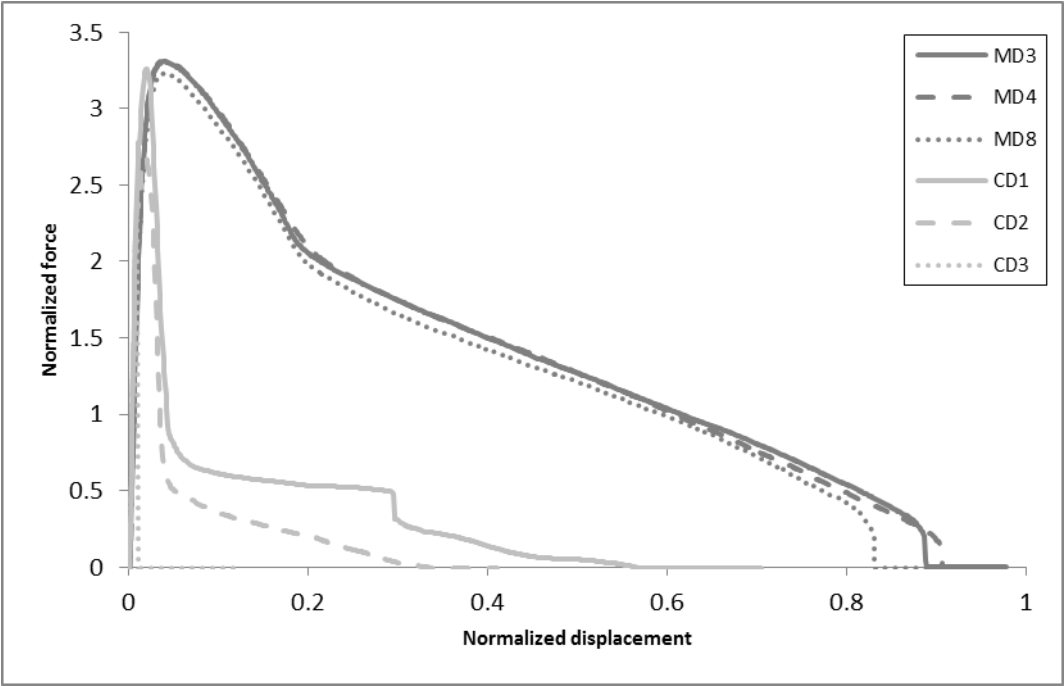


Figure 3.24: Normalized force-displacement curves for DIC test specimens.

### MD

The force-displacement curve, along with corresponding images of the test specimen is shown in Figure 3.25. It can be seen that there is an opening of the crack in the initial part of the curve, which is followed by crack propagation and a necking area. As the displacement continues, the area to the right of the crack gets highly deformed. The crack continues to grow until the edge of the test specimen is reached and fracture occurs. The deformed specimen has a longer piece hanging from the top than the bottom, thus there is asymmetry. This asymmetry could be due to the loading, the upper grip was the only one moving. It could also be due to material orientation and thickness. Throughout the test, the speckle pattern follows the movement of the test specimen, thus the surface layer is involved in the deformation process. When studying how the speckle pattern deforms, it is clear that the direction of the deformation is towards the bottom right of the specimen. Furthermore, there is a small amount of slippage at the fixed grip.

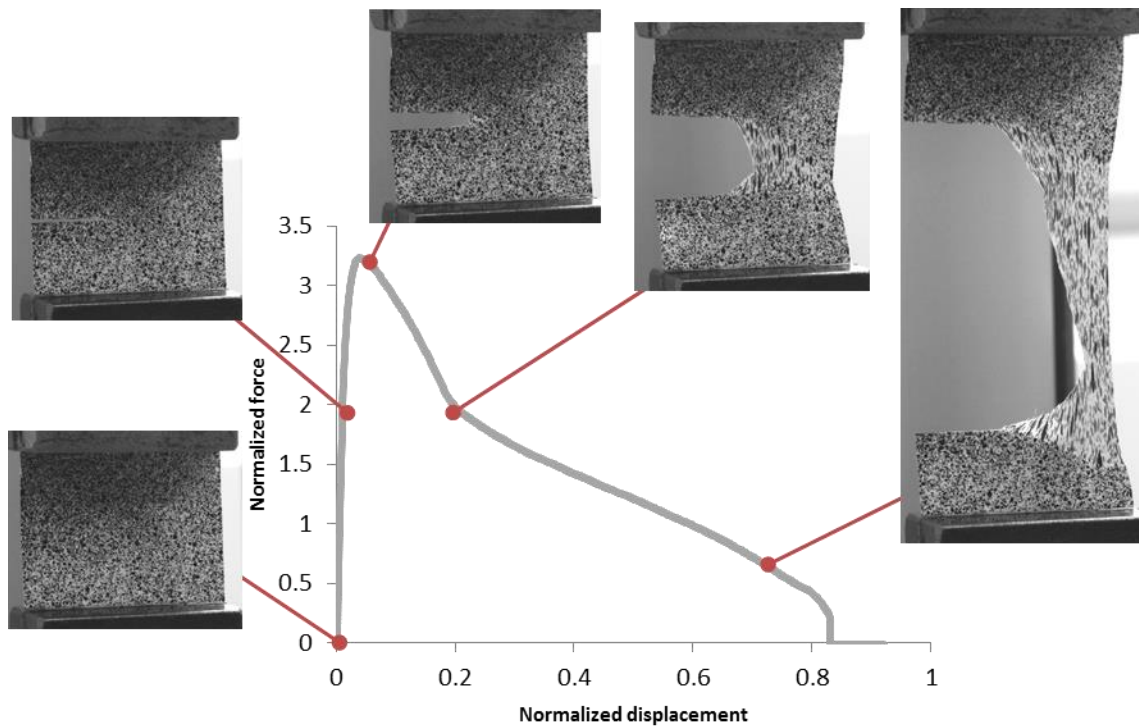


Figure 3.25: Normalized force-displacement curve for MD, with corresponding images at selected points.

The initial part of the force-displacement curve is shown in Figure 3.26. Up to the peak of the curve, there is an opening of the crack, without there being any crack propagation. From the images of the crack, blunting of the sharp crack is visible. Also, close to the peak of the curve, a necking region beyond the crack edge is formed and evolved in the shape of a V. At the peak of the curve, the crack starts to propagate, with a propagating neck in front of it.

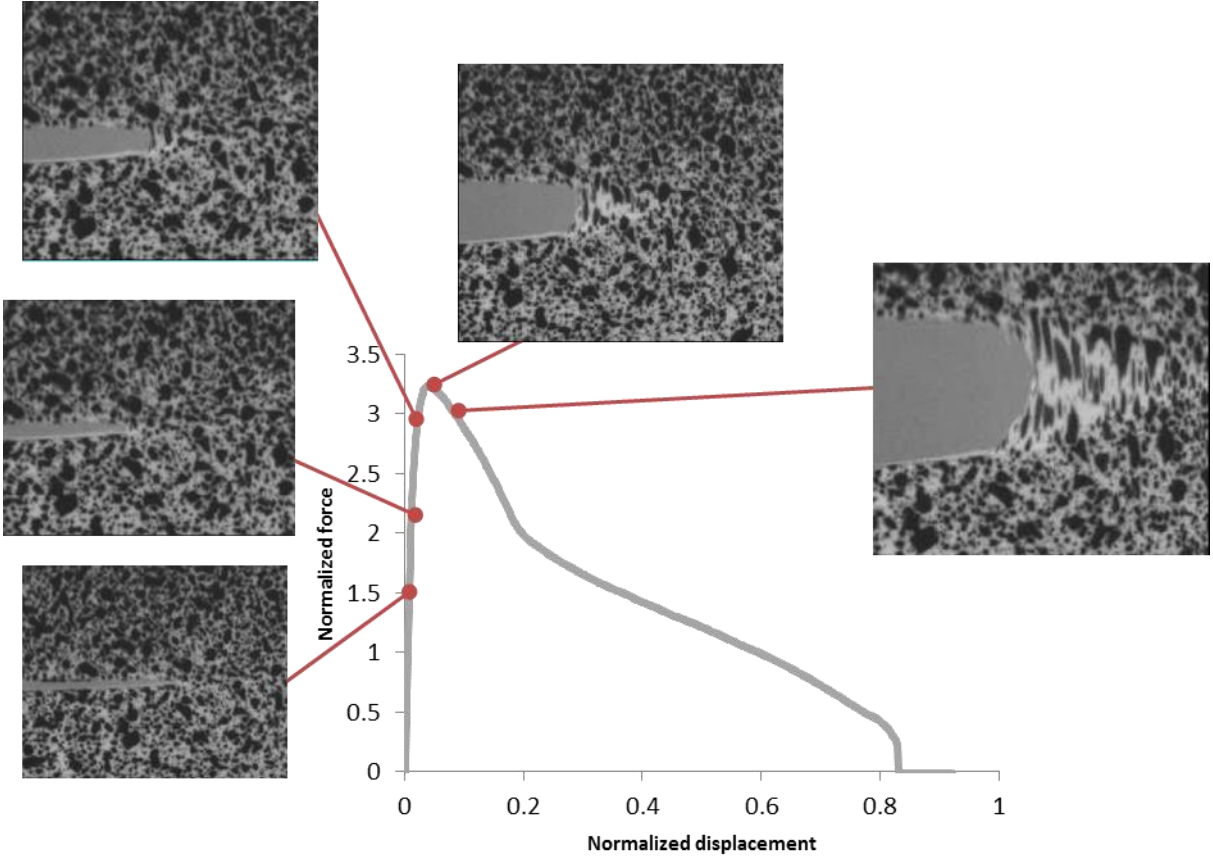


Figure 3.26: Normalized force-displacement curve for MD, with corresponding enlarged images of the crack edges for the beginning of the curve.

The major principal strain field for MD for the same section of the force-displacement curve is shown in Figure 3.27. The strain field shown is the largest principal strain of the Hencky strain tensor, also referred to as true strain. In the figure, the strain field is shown for the whole sample, the scale is fixed and the same for all images. The images show areas where no strain fields were measured, this could be due to a crack or due to difficulties in correlation. Therefore, the crack opening should be studied in the images showing speckle pattern. As the sample starts to deform, a region of higher strains is located at the crack tip, directed towards the corners of the sample. When the crack starts to grow, the strain is further increased close to the crack tip and is showing a region of higher strains towards the corner of the fixed grip. The shape of the strain region is in line with the shape of the plastic region, presented in in the theory in section 2.3.

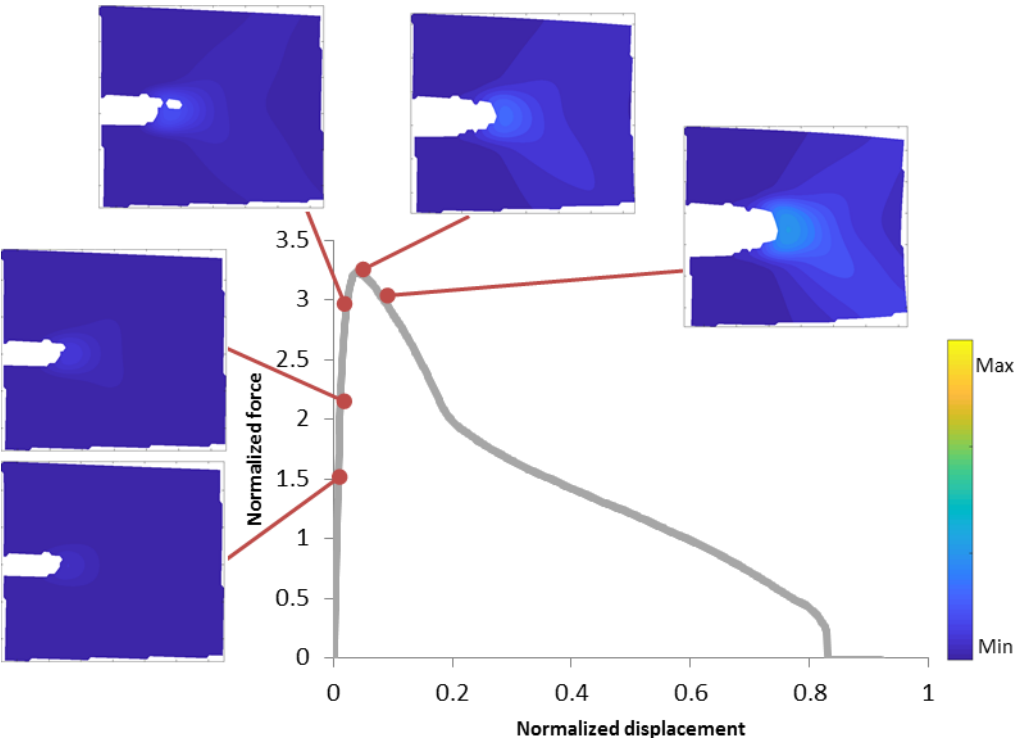


Figure 3.27: Major principle Hencky strain fields for MD, full field, corresponding to previous positions on the normalized force-displacement curve.

After the initial peak, the force decreases and the necked area increases, as can be seen in Figure 3.28. The crack propagates, leaving the material below the crack to be unaffected by further deformation, whilst the material above keeps on being drawn into the highly deformed area until the crack has propagated to the edge of the test specimen, creating a kink in the force-displacement curve. In the test specimen, there seems to be no crazing. The necking region close to the crack edge largely exceeds the thickness of the plate. Another observation that can be made is that there are some thin threads sticking out from the cracked surface on an otherwise smooth surface.

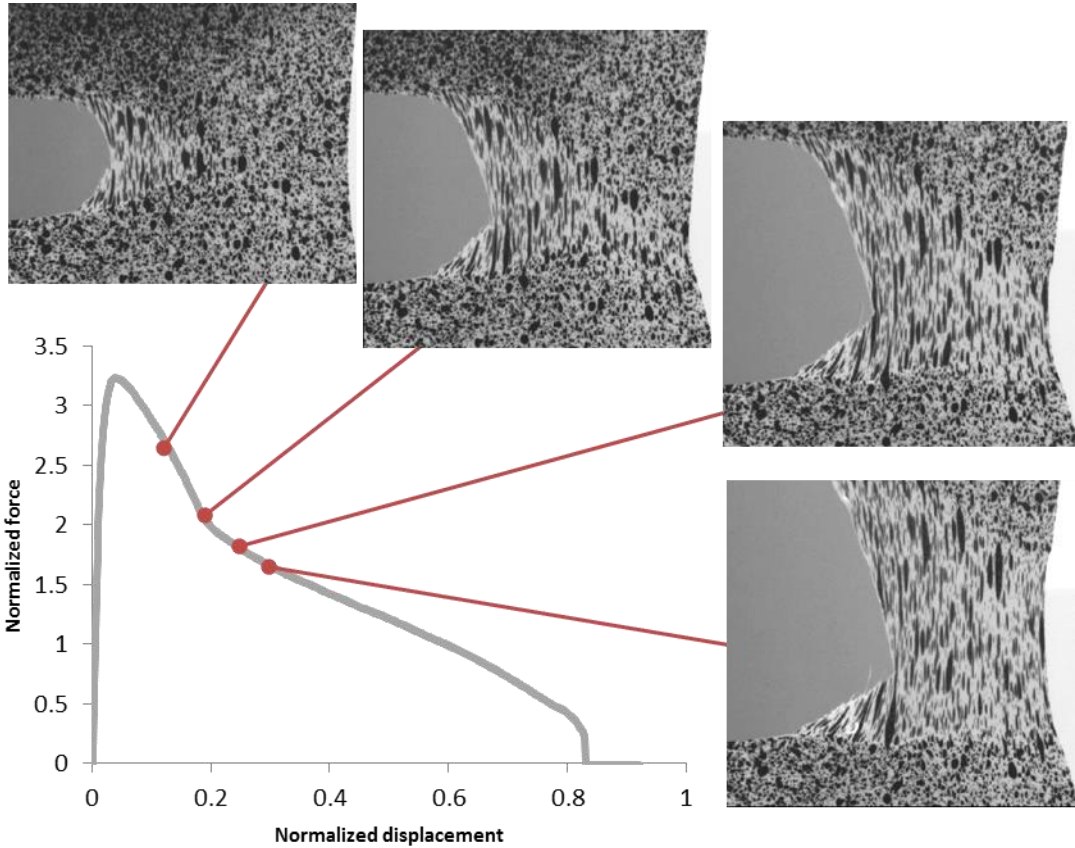


Figure 3.28: Normalized force-displacement curve for MD, with corresponding images of the crack edge for the second half of the curve.

The major principal strain fields for the same part of the force-displacement field is shown in Figure 3.29. Note that the scale of the strains is the same as in previous figures. The images show high strains near the crack tip and towards the right side of the sample, in a slight angle towards the fixed grip. As the deformation is increased, the strain increases whilst having the same shape of the strain region.

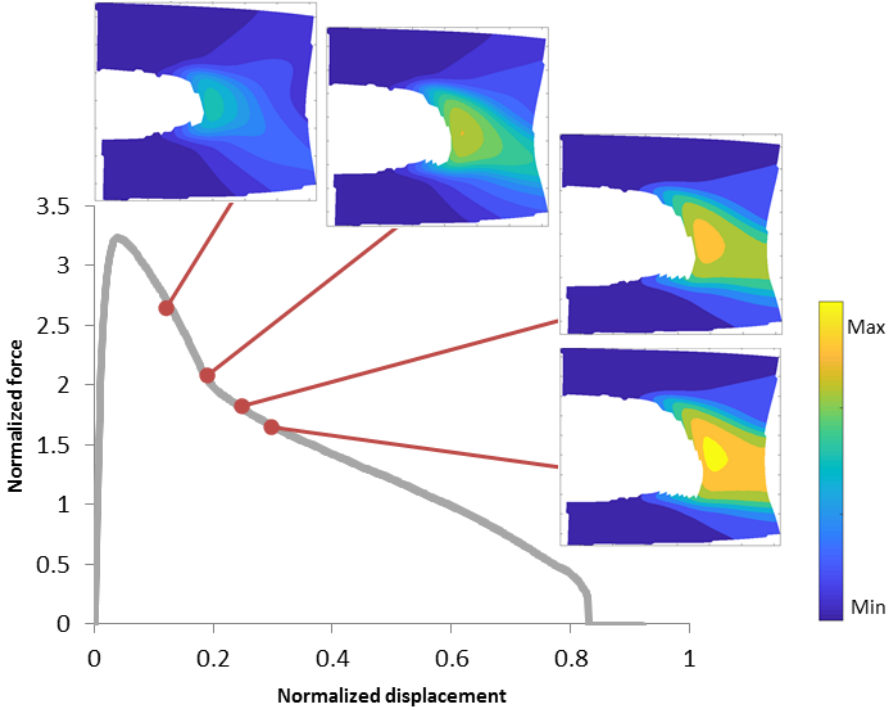


Figure 3.29 Major principle Hencky strain fields for MD, full field, corresponding to previous positions on the normalized force-displacement curve.

### CD

The force-displacement curve for the CD specimen is shown in Figure 3.30, with corresponding images of the test specimen. Also, in Figure 3.31, enlarged images of the crack are shown. From the figures, it is possible to see that there seems to be no blunting and hardly any opening of the crack, unlike MD. Since CD has less of a crack opening and blunting before crack growth, this indicates that the fracture toughness is lower for CD than MD. When the force is increased to an initial peak, there seems to be no crack propagation. After the peak is reached, the crack starts to propagate rapidly. As the crack propagates, material with no speckle pattern is shown, indicating that the different layers of the specimen fracture at different times and that there is crack growth under incomplete penetration. The skin layer, with the speckle pattern fractures earlier than what could be the bulk or even the shear layer. As the crack propagates, it leaves behind a rough fracture surface, which could be an indication of crazing. Little to no necking of the material can be seen visually, nor can the type of penetration be determined. When the crack has moved almost fully through the plate, there is a small string left to deform. This string is probably due to the test set-up more than a material property.

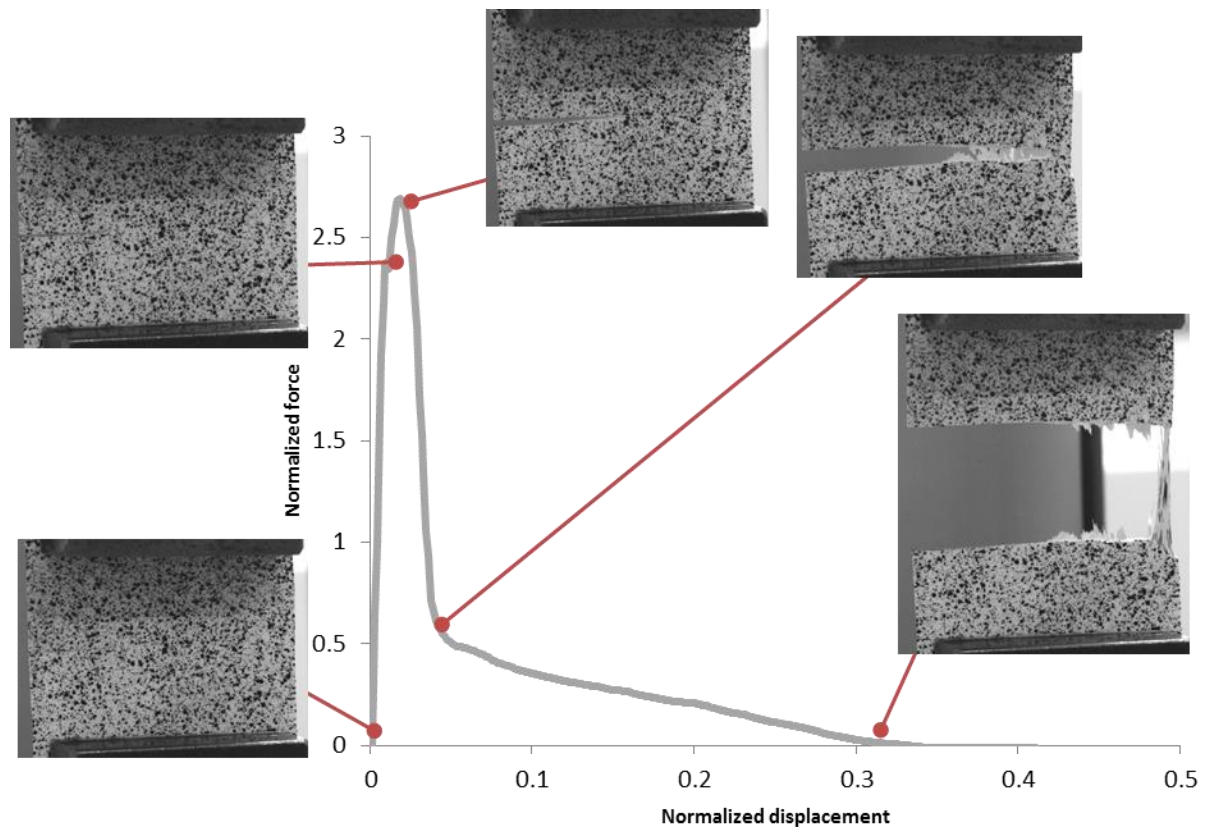


Figure 3.30: Normalized force-displacement curve for CD, with corresponding images at selected points.

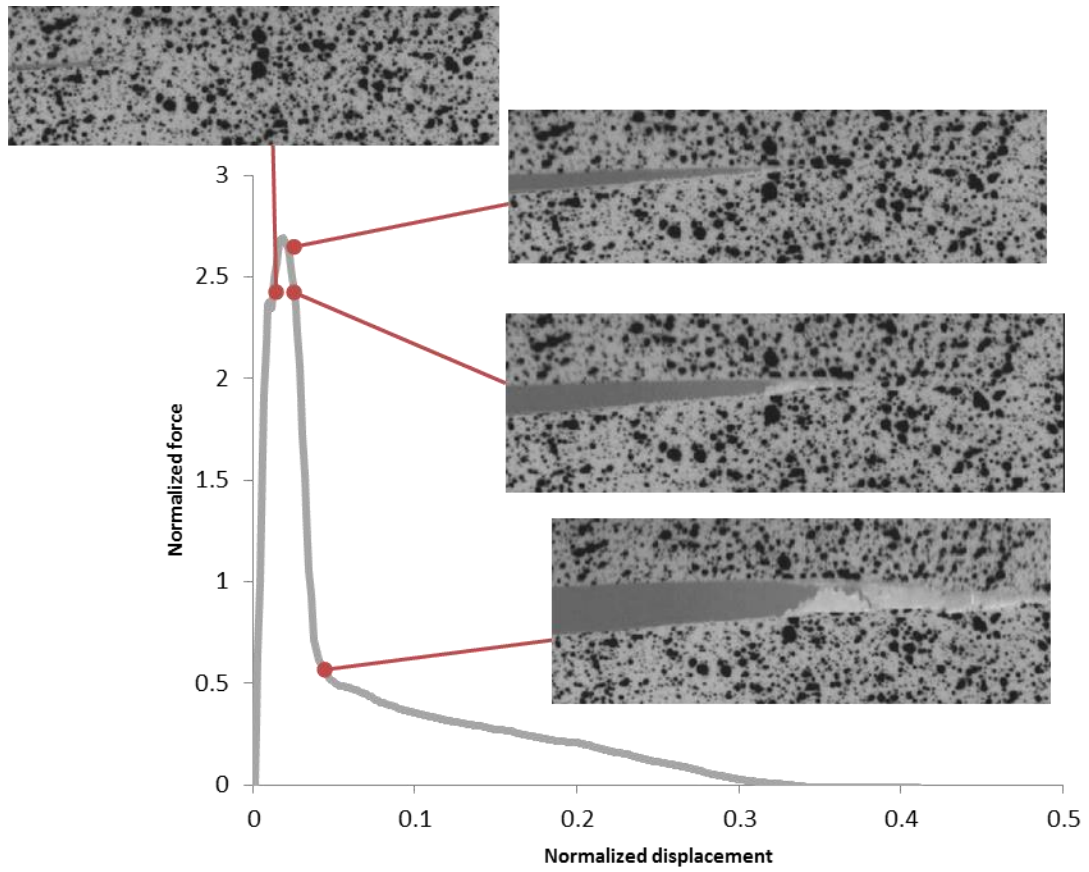


Figure 3.31: Normalized force-displacement curve for CD, with corresponding images at selected points, enlarged at the crack.



The major principle strain for the CD test specimen is shown in Figure 3.32. The strain scale is the same for all the images in the figure, but not the same as for MD. For CD, the strain field is located at the crack tip, towards the corners of the test sample. As the crack grows, the strain fields are limited, making it difficult to measure strain near the crack.

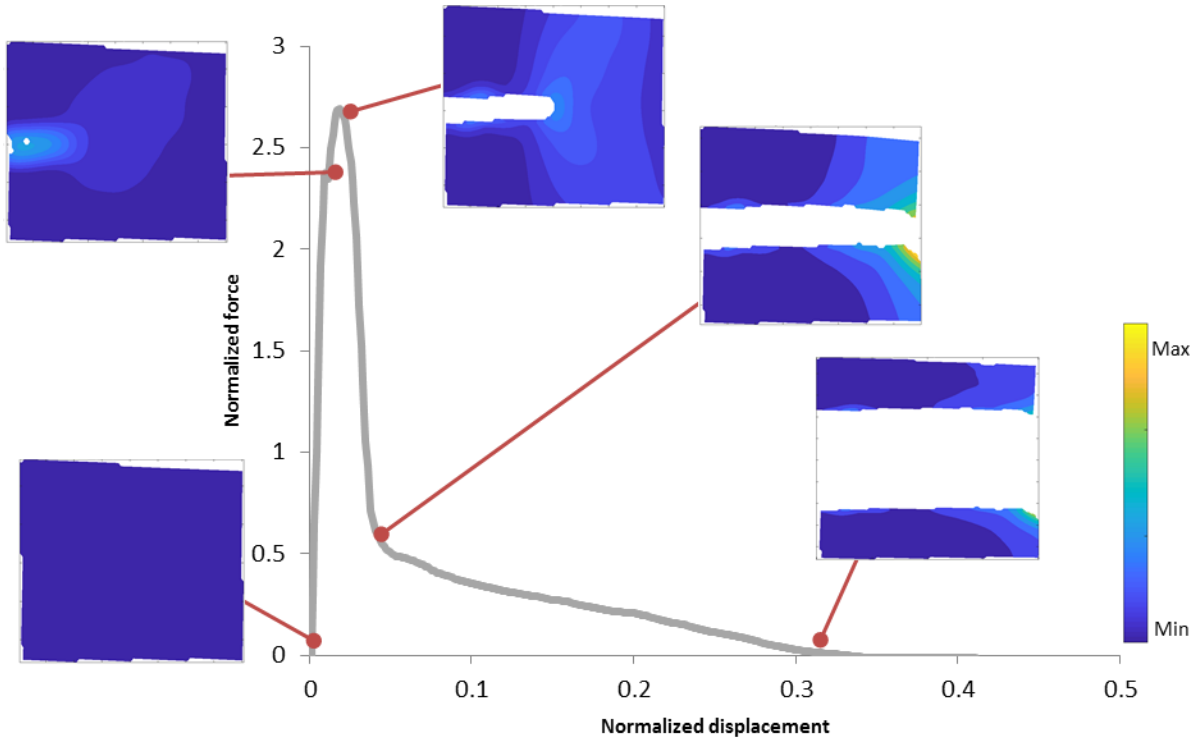


Figure 3.32: Major principle Hencky strain fields for CD, full field, with positions on the normalized force-displacement curve.

Furthermore, for MD there seems to be a correlation between the speckle pattern movement and the specimen deformation. However, it is unclear if the strain fields are representative of what is happening inside the material, as pointed out by Broberg, [10], what happens on the surface does not always represent what is going on inside the material. For CD it is important to keep in mind that the speckle pattern was lost as the crack propagated, thus the strains fields are not representative of the white area shown in the previous figures. However, from the strain fields presented, some similarities between MD and CD are shown. Both specimen show higher strains near the crack tip and towards the corners of the test specimen.

## 4 Abaqus Simulation

In the following section, the virtual engineering section of the master thesis is presented. The simulations were conducted in Abaqus and were focused on MD. The simulations were made for two models; one of a dogbones sample to calibrate the material model and one of the cracked plate, the one used for fracture mechanical testing.

### 4.1 Dogbone Sample

To start with, a material card was needed. As previously presented in section 1.1.1, this was created by inverse calibration. One part of the optimization loop was the simulation in Abaqus of a dogbone sample, similar to the one used in the physical tensile tests. The model of the dogbone sample was created at Tetra Pak prior to this thesis. In this section, the model of the dogbone sample is presented briefly.

The modelled part of the dogbone sample was the section that would have been in between the grips during a physical tensile test. The bottom of the sample was set to be fix, whilst the top is set to a fixed displacement in the direction of the dogbone. In Figure 4.1, the mesh is presented, the top half has an area of finer mesh, due to necking initiating in this area. The model consists of linear elements (8-node brick, C3D8) of size 0.6 mm and 0.1 mm. The thickness of the dogbone was set to be 0.63 mm and consists of five elements. The material was set to homogenous and isotropic. The material model consisted of linear elasticity, combined with Mises yield surfaces, which were presented in section 2.5.1. The input was the Young's modulus, Poisson's ratio, density and the plastic strain as a function of the stress, according to Equation 2.5 and Equation 2.6. Furthermore, the Abaqus implicit solver was used as a solver.

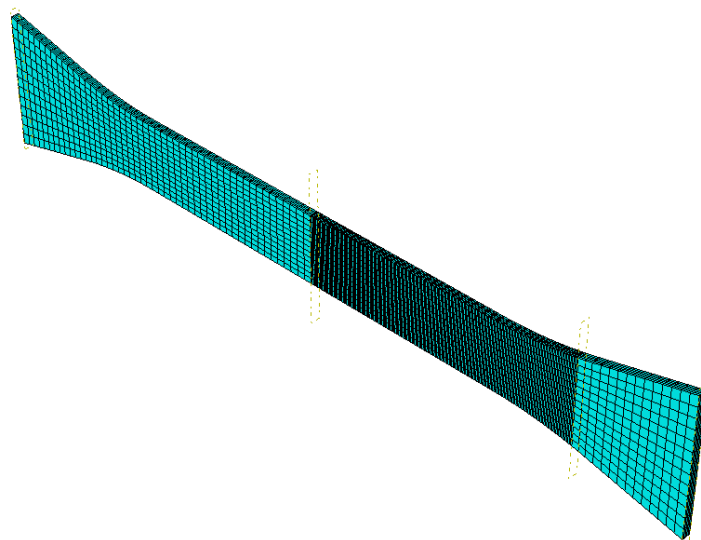


*Figure 4.1: Mesh of dogbone sample, with finer mesh closer to the loaded end.*

## Results

In Figure 4.2, an image of the deformed dogbone sample is shown. From the figure, one can see that there has developed a necked region, closer to the loaded end of the sample. The necked region is both thinner and more narrow than the rest of the sample.

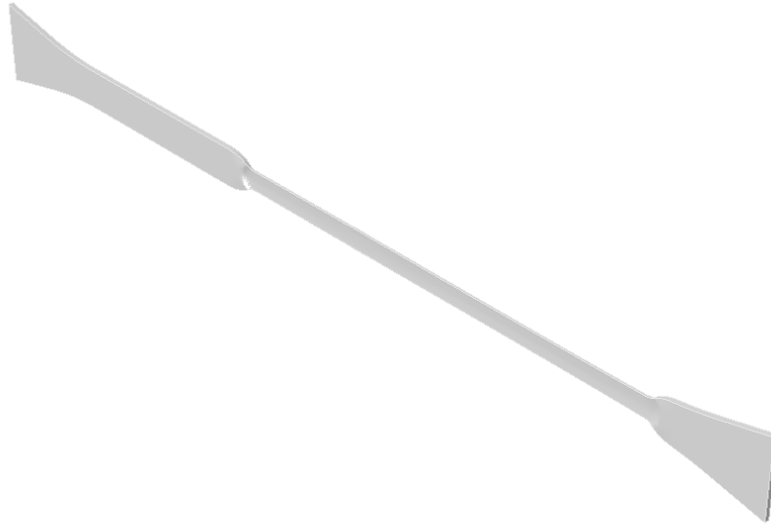


Figure 4.2: The deformed dogbone sample.

From the simulation, the macroscopic force and displacement was plotted against the averaged curve from the tensile testing, as shown in Figure 4.3. Also, in the figure the true stress and true strain curve is shown, which is the input for the plastic section of the Abaqus material card. From the figure, it is shown that the simulation and thus the material card, had a similar Young's modulus to the physical test. However, the force dip after the initial peak was not fully captured.

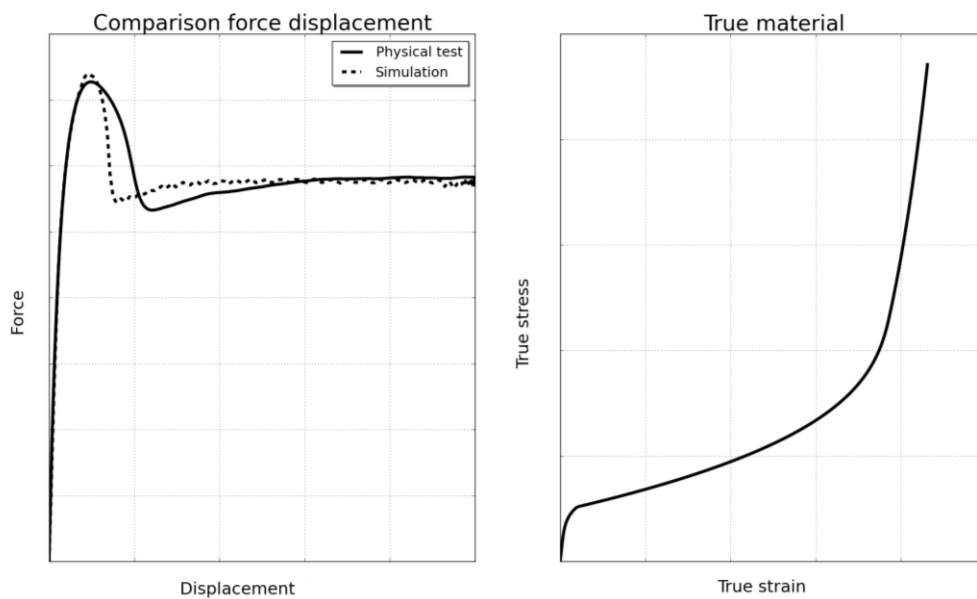


Figure 4.3: Force-displacement curves for physical test and simulation, along with the true stress-strain curve from the simulation.

## 4.2 Fracture Mechanical Testing

The model of the cracked plate was made to resemble the physical fracture mechanical test performed at LTH as much as possible. As the simulations were focused on MD, here the cracked plate model was based on the test specimen previously referred to as MD-R. The geometry and the dimensions of the plate are presented in Figure 4.4 and Table 4.1. Some simplifications of the geometry were made; the plate was set to have a uniform thickness of 0.60 mm, which is not the case for the physical plates, which usually have a thickness varying from 0.59 mm to 0.61 mm. Moreover, the crack was set to be infinitely sharp and the height of the plate was set to 50 mm, taking into consideration flow of material on the inside of the plate.

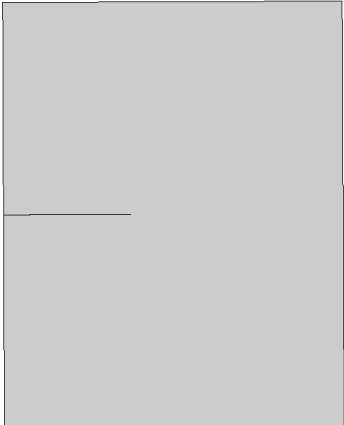
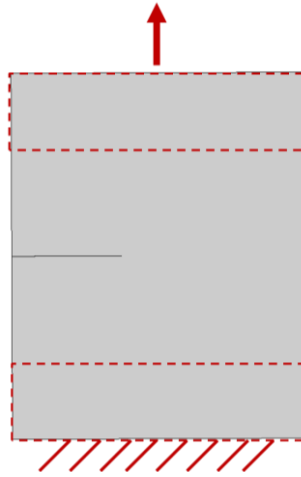


Figure 4.4: Geometry of cracked plate.

Table 4.1: Dimensions of cracked plate.

Dimension	[mm]
Height	50
Width	40
Thickness	0.60
Crack length	15
Grip width	40
Gauge length	30

The boundary conditions were modeled by having a top and a bottom area of the plate that move as the grips did in the physical test, as can be seen in Figure 4.5. The bottom of the plate was set to be fixed in all directions, whilst the top was set to move in the direction of the plate, whilst unable to move in any other direction. No consideration was taken to slippage between the plate and the grips. The speed was set to be the same as the be 100 mm/s, which is 60 times faster than the physical tests and the simulation time was 0.75 s.



*Figure 4.5: Illustration of the grips and thus the boundary conditions of cracked plate.*

Regarding the material of the plate, it was set to be homogenous and isotropic, which is a simplification. The material card used was the one made by inverse calibration and presented in the previous section. The main focus of the simulation of the cracked plate was to determine the damage model and its parameters. An explicit solver was used, with a regularization value of 0.001. The mesh of the model is shown in Figure 4.6. The mesh consists of linear elements (8-node brick, C3D8) of size 3.0 mm to 0.4 mm, with the smaller element size the closer to the crack the element is.

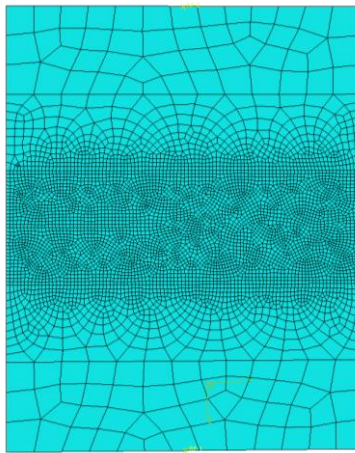


*Figure 4.6: Mesh of cracked plate.*

## Results

A number of different damage initiation and evolution values and types of softening were tested for the cracked plate. The final setting used and thus the one the most similar to the DIC on tensile tests was a damage initiation value of 1.8 with a damage evolution including displacement at failure of 0.40 and an exponential softening of value -5. The true stress and strain curve for a material card with and without the damage parameters is illustrated in Figure 4.7. The damage initiation is where  $D = 0$ , thereafter, the material curve is described by the damage evolution until final fracture and  $D = 1$ .

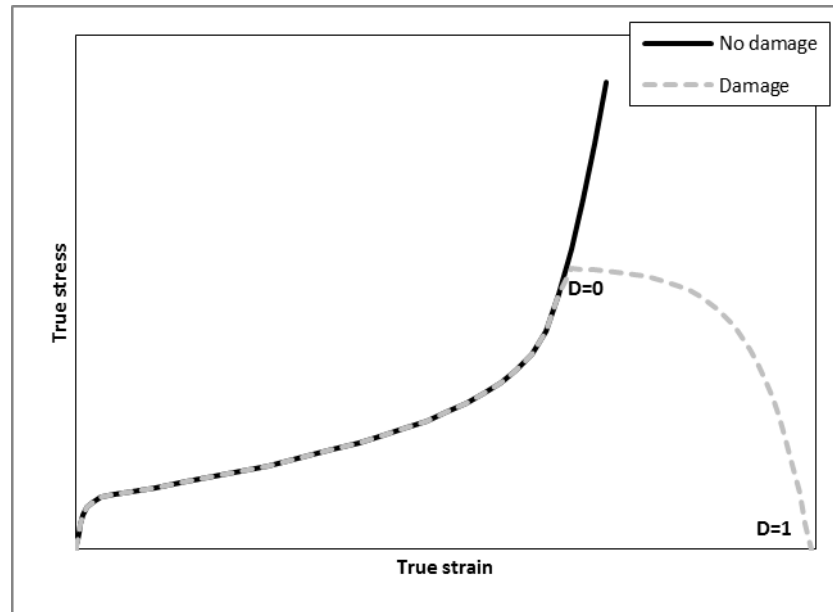


Figure 4.7: Illustration of material card with and without damage.

The resulting force-displacement curve, along with images of the cracked plate at selected points is presented in Figure 4.8. From the figure, it is seen that the force-displacement curve has an initial force peak, where crack opening and blunting has occurred. Thereafter, the force is decreased and a necked region, in the shape of a V is formed towards the edge of the plate. Up to this point, there is little to no crack growth. When the crack starts to grow, the slope of the force-displacement curve is somewhat decreased. The crack continues to grow in a symmetric manner until final rupture.

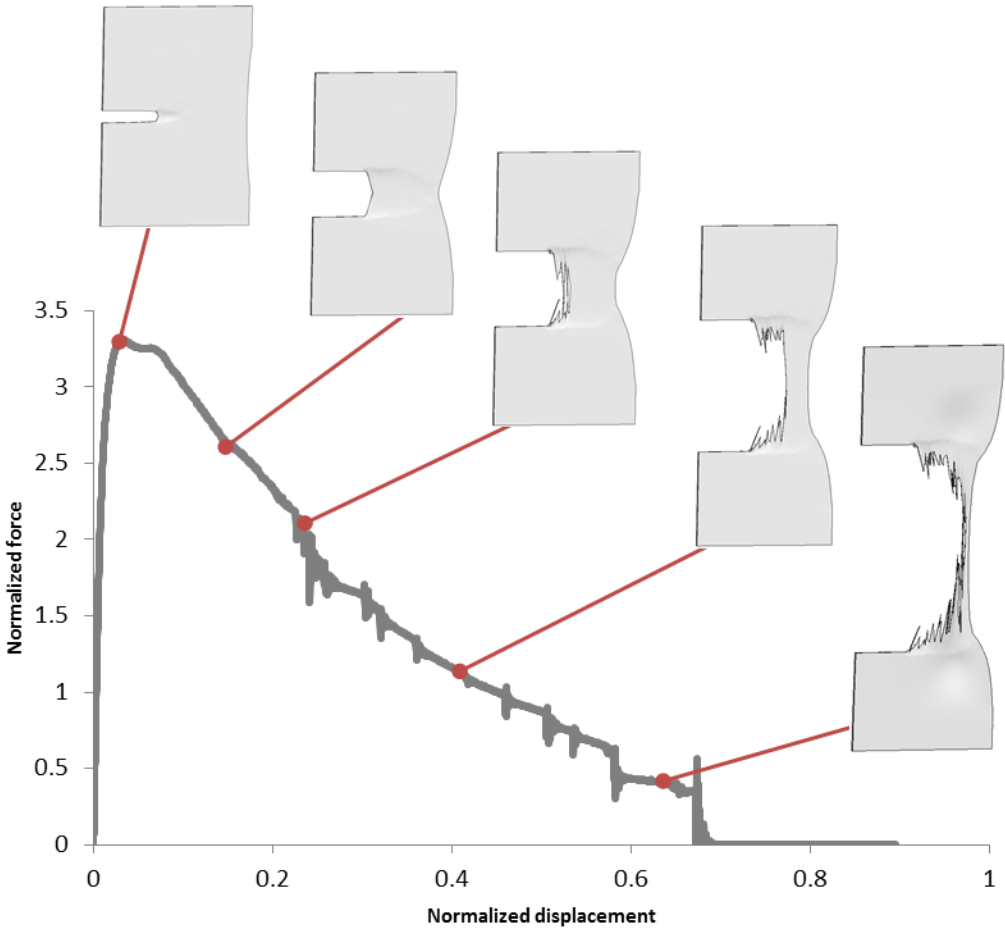


Figure 4.8: Normalized force-displacement with corresponding images at selected points.

Important to consider is the mesh-dependency, where changing the element size would result in a need to change the damage parameters to be able to get the same result as previously. However, with a finer mesh there would be less of a distortion of the elements and the fracture surface would be less rough.

## 5 Discussion

This thesis includes several experimental techniques, leading up to the simulation of a cracked plate in MD-R. Due to the difference in mechanical behavior of MD and CD, the conclusions made for MD cannot be directly transferred onto CD. In this section a discussion of the different techniques and their results is presented, starting with a comparison of the simulation and the DIC of the cracked plate in MD.

When comparing the simulation to the DIC, there are several things that can be compared to one another. Firstly, the visual appearance of the samples, secondly, the force-displacement curve and lastly the strain fields. In Figure 5.1 both the force-displacement curve and the visual appearance of the simulation and the DIC are presented. From the figure, it can be seen that the initial behavior, until the force peak, the simulation and the DIC correlates very well. After the force peak, the necking region propagate faster in the simulation than what can be seen in the DIC. Thereafter, the curves are not as similar to each other and the crack is propagating. In the simulation, voids in the necked region occur before the crack edge. Furthermore, for the simulation the crack direction is straight to the edge of the plate, whilst for the DIC the direction is to the bottom right corner. Throughout the curve, the opening of the crack is similar in the simulation and the DIC.

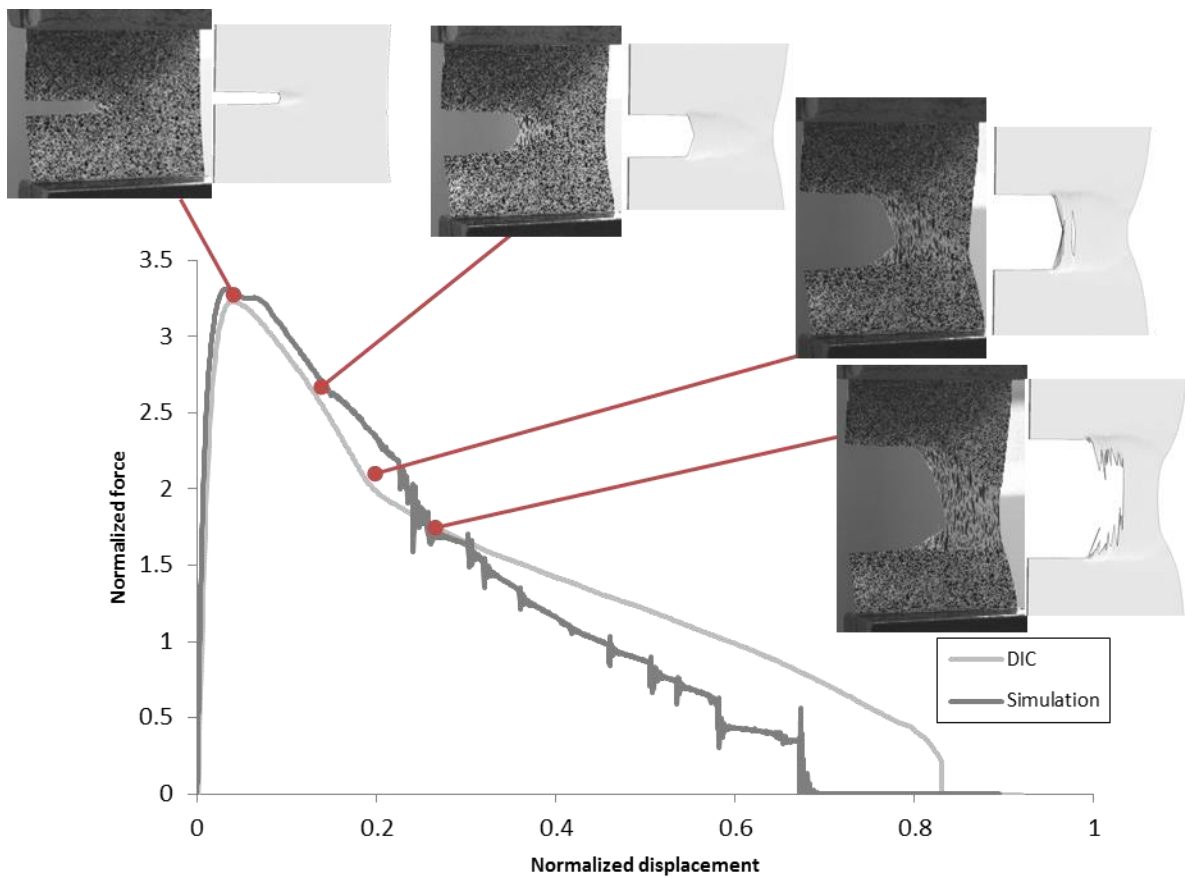


Figure 5.1: Normalized force-displacement curve for MD-R, with corresponding images for simulation and DIC.

In Figure 5.2 the strain fields from the simulation and the DIC are presented at selected points on the force-displacement curve. It can be seen that the strain fields have the same shape,



until the two last images, where the strain field from the DIC is more slanted to the bottom edge and the strain field from the simulation is symmetric. The amplitude of the strain fields is in general a bit higher for the simulation than measured by DIC. Important to consider is that in the DIC, the subset affects the resolution but also there has been a loss of data, making the crack look bigger than it actually is, which is presented better in Figure 5.1.

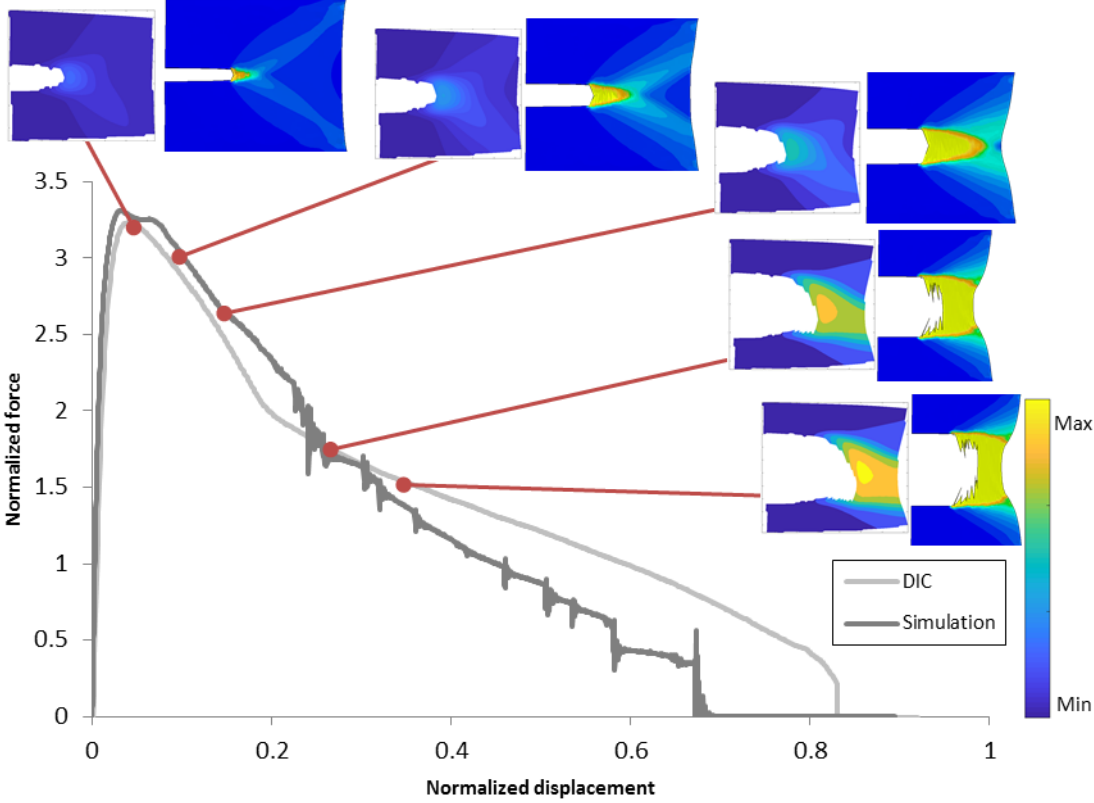


Figure 5.2: Normalized force-displacement curve for MD-R, with corresponding images with major Hencky strain fields for DIC to the left and simulation to the right. The scale is the same for all images.

Important to consider is the limitations and simplifications of the simulation and how it differs from the physical tests. As mentioned earlier, in the simulation there is no slippage or anisotropy, nor is there any differences in material behavior through the thickness. The simplifications impact the result and thus how well the simulation correlates to the DIC. Furthermore, the material and damage model used is intended for metals, not polymers, but seeing as there is no material model specifically for polymers, the chosen material model was the best, though not a perfect fit.

The SEM-images of an MD-R sample showed the different layers and how they seem to fracture at separate occasions. Implementing this in the simulation model could impact the result. The reason for the crack direction to be different in the simulation compared to the DIC could be due to the simplifications made, settings chosen and the meshing of the model. Despite the simplifications made, there is still quite a good correlation between the simulation and the DIC for the chosen damage settings, showing the possibilities of modeling fractures in Abaqus.

When doing simulations, there is a need to consider to what detail the model should represent the physical specimen and test method. For instance, in SEM, it was shown that there is fibril structure of the material, in the inner layers of the plate. These could be modelled but would render a heavy simulation, perhaps too focused on the microstructure to capture the macroscopic behavior. The trade-offs made should be so that the model represents the physical behavior well, without being too detailed.

Regarding DIC, there is further information that could be gained from the tests. For example one can measure the crack tip opening displacement. However, it is unclear whether or not the DIC is representative of what is happening inside of the material. Furthermore, the tensile testing and inverse calibration affects the simulation of the cracked plate. How well the material card represents the real material behavior will impact the accuracy of the simulations.

The fracture mechanical testing for different crack length showed a decrease in force for longer initial crack length, which is in line with the theory presented. Also, MD-R showed more blunting of the crack opening than CD-T, indicating higher toughness for MD-R, further confirming the anisotropy of the material. Also, MD-R has much more of a ductile behavior than CD-T. However, the fracture mechanical testing had some difficulties in fixation of test specimen and better grips would probably lead to a force peak more like the simulation.

Furthermore, SAXS and WAXS could reveal quite a bit on the material orientation of the dogbone sample. However, there was no difference for the positions in the undeformed sample which could explain the difference seen in fracture mechanical behavior of the different CD test specimen. To get a more precise result, with less of an averaging, a smaller beam size would be needed. Also, there was a problem with a too small detector to be able to capture the scattering pattern fully. Therefore, new settings would be required to get a better result.

## 6 Conclusion

In this master thesis the damage behavior and damage modeling of an injection molded plate of HDPE were investigated. The work has included many different experimental techniques and has shown the possibilities of combining several techniques to investigate the material mechanical and fracture mechanical behavior of a polymer. From tensile testing of dogbone samples, it can be concluded that the material behavior is dependent on material direction. Furthermore, SAXS and WAXS was used on an undeformed and a deformed dogbone sample to investigate the material orientation. It was shown that the dogbone sample has an initial anisotropy, which is further increased as the dogbone is deformed in tension. For a deformed specimen, the necked region has more of an orientation whilst the region without necking has similar orientation to the undeformed specimen. However, it was not possible to determine any differences in material orientation of an undeformed sample depending on the distance from the injection point.

From fracture mechanical testing, it was shown that the fracture mechanical behavior is dependent on location and orientation of the crack as well as displacement rate. The specimen of MD-R and CD-T behave very differently in tension testing. Thus there is a dependence of where the crack is placed and the direction of the crack, which could not be fully explained by SAXS and WAXS. The anisotropy of the injection molded plate place an important role. Increasing or decreasing the crack length will keep the same fracture mechanical behavior, though the amplitude of the force-displacement curve will decrease. From SEM of an MD specimen, it was seen that the top layer of the injection molded plate delaminate and fractures separately during tensile testing.

DIC of MD and CD made it possible to relate the physical appearance with the positions on the force-displacement curve. It was shown for MD that at the initial force peak, the crack starts to grow slowly, with a large opening and blunting of the crack tip. After which there is a large deformation and continued crack growth, leading to fracture. For CD there is more of a sharp and fast crack growth, were the layers through the thickness fracture at different times.

The cracked plate of MD-R was modeled in Abaqus with a damage model implemented. A comparison of the simulation with the DIC show large similarities in visual appearances and force-displacement curves. Even though, there are simplifications made in the simulation model, there is still a good correlation between the simulation and the physical tests.

## 7 Future Work

There are several possibilities to continue the work this master thesis has started. To begin with, the fracture mechanical testing should be applied for more settings, such as temperature, but also to gain more statistical data. To eliminate the slippage between the grips and the test specimen, better fixtures are needed. Furthermore, more tests on MD could be performed to see why there is an asymmetry of the fractured specimen, to start with by changing the positioning of the sample. By turning the sample upside-down, one can see if the crack direction is due to loading or not. The fracture mechanical testing could also further investigate the effects on position of the crack, if there is a significant change in behavior when the crack originate from the edge or the middle of the plate.

Furthermore, it was shown that the different CD specimen behave differently. Why this is could not be shown fully in this thesis and could therefore be further investigated. There is a possibility of using SAXS and WAXS to further investigate the material, both at more positions but also through the thickness. Also, with in-situ testing could a great deal of knowledge could be gained, including information on the elastic deformation. The data collected in this thesis could be further investigated, such as what the d-spacing relates to. Further material behavior could be gained from in-situ testing in SEM, thereby one can see when each layer fractures and when delamination occurs.

There are also further possibilities of using DIC, both for other applications, but also to continue the work in this thesis, by studying more specimen and for more settings. Information on what occurs inside the material could be gained by Digital Volume Correlation (DVC).

The simulation could be further improved and tested for more cases, such as different crack lengths, but also to model CD-T, seeing as in this thesis the simulation was focused on MD-R. The anisotropy could then be modeled, enabling loading in a mix of directions. Other aspects to consider is stress triaxiality and strain rate. By having a good simulation, situations can be predicted instead of only replicated and analyzed. When a good model exists, this should be tested in the simulation of an application and see how well the simulation correlates with reality.

Furthermore, it should be considered if it is possible to perform fracture mechanical testing at higher speeds, which would be more representative of the material behavior of the application. Possibly, at a higher speed, the fracture mechanical behavior is also be easier to model in Abaqus.

As explained in the beginning of this report, a package includes several materials out of which only one is investigated. The work performed could be implemented to include other polymers.

## 8 References

- [1] Tetra Pak, "Tetra Pak history," Tetra Pak, [Online]. Available: <https://www.tetrapak.com/about/history>. [Accessed 23 January 2018].
- [2] Tetra Pak, "Tetra Pak in brief," Tetra Pak, [Online]. Available: <https://www.tetrapak.com/about/tetra-pak-in-brief>. [Accessed 23 January 2018].
- [3] S.-F. Hwang, M.-C. Shen and B.-B. Hsu, "Strain measurement of polymer materials by digital image correlation combined with finite-element analysis," *Journal of Mechanical Science and Technology*, vol. 29, no. 10, pp. 4189-4195, 2015.
- [4] J. Abanto-Bueno and J. Lambros, "Investigation of crack growth in functionally graded materials using digital image correlation," *Engineering Fracture Mechanics*, vol. 69, pp. 1695-1711, 2002.
- [5] W. D. Callister Jr. and D. G. Rethwisch, *Fundamentals of Material Science and Engineering*, 4th ed., Asia: John Wiley & Sons, 2013.
- [6] U. Bruder, *User's guide to plastics*, Lithuania: Bruder Consulting AB, 2014.
- [7] "The Handy Chemistry Answer Book," papertrell, [Online]. Available: [https://www.papertrell.com/apps/preview/The-Handy-Chemistry-Answer-Book/Handy%20Answer%20book/What-is-LDPE-low-density-polyethylene/001137025/content/SC/52cb010082fad14abfa5c2e0\\_default.html](https://www.papertrell.com/apps/preview/The-Handy-Chemistry-Answer-Book/Handy%20Answer%20book/What-is-LDPE-low-density-polyethylene/001137025/content/SC/52cb010082fad14abfa5c2e0_default.html). [Accessed 12 February 2018].
- [8] Engineer Designer, "Top five benefits of plastic injection moulding," Engineer Designer, 8 December 2016. [Online]. Available: <http://www.engineeringdesigner.co.uk/2016/12/08/top-five-benefits-plastic-injection-moulding/>. [Accessed 8 February 2018].
- [9] E. Andreasson, L. Persson, H. Jacobsson and N. Johan, "Integrating Moldflow and Abaqus in the Package Simulation Workflow," in *SIMULIA Community Conference*, Providence, 2013.
- [10] K. B. Broberg, *Cracks and Fracture*, Academic Press, 1999.
- [11] T. L. Anderson, *Fracture Mechanics - Fundamentals and Applications*, 3rd ed., Taylor & Francis Group, CRC Press, 2005.
- [12] J. G. Williams, D. R. Moore and A. Pavan, "Fracture Mechanics Testing Methods for

- Polymers, Adhesives, and Composites," *European Structural Integrity Society*, vol. 28, pp. 3-375, 2001.
- [13] Dassault Systemes, "ABAQUS UNIFIED FEA - Complete Solutions for Realistic Simulations," Dassault Systemes, [Online]. Available: <https://www.3ds.com/products-services/simulia/products/abaqus/>. [Accessed 9 March 2018].
- [14] "Abaqus 2016 Online Documentation," Dassault Systèmes, 5 July 2015. [Online]. Available: <http://50.16.225.63/v2016/index.html>. [Accessed 12 February 2018].
- [15] Philips Electron Optics, *Environmental Scanning Electron Microscopy: An Introduction to ESEM.*, The Netherlands: Philips Electron Optics, 1996.
- [16] B. Pan, K. Qian, H. Xie och A. Asundi, "Two-dimensional digital image correlation for in-plane displacement and strain measurement: a review," *Measurement Science and Technology*, vol. 20, 2009.
- [17] Y. Dong och B. Pan, "A Review of Speckle Pattern Fabrication and Assessment for Digital Image Correlation," *Experimental Mechanics*, vol. 57, pp. 1161-1181, 2017.
- [18] J.-J. Orteu, "3-D computer vision in experimental mechanics," *Optics and Lasers in Engineering*, vol. 47, pp. 282-291, 2009.
- [19] P. Willmott, *An Introduction to Synchrotron Radiation: Techniques and Applications*, John Wiley & Sons, Ltd. , 2011.
- [20] H. Schnablegger and Y. Singh, *The SAXS Guide*, Austria: Anton Paar GmbH, 2011.
- [21] J. Engqvist, "Mechanical behavior of glassy polymers: experiments and modelling," Media-Tryck AB, Lund, Sweden, 2016.
- [22] S. Schmacke, "Investigations of Polyethylene Materials by Means of X-ray Diffraction - Artificial Ageing of Polyethylene Gas Pipes," 2010.
- [23] DUMBBELL CO., LTD, "Super Dumbbell Cutters Available [Extracted] List of Corresponding Standards," UMBELL CO., LTD, [Online]. Available: [http://www.dumbbell.co.jp/english/super\\_dumbbell01.html](http://www.dumbbell.co.jp/english/super_dumbbell01.html). [Accessed 14 February 2018].

# Appendix

## A. Data collection points for SAXS and WAXS for deformed specimen

Positioning of data collection points, with labelling according to section 3.1.2. The size of the circles have the same relation as the actual beam size had to the sample size.

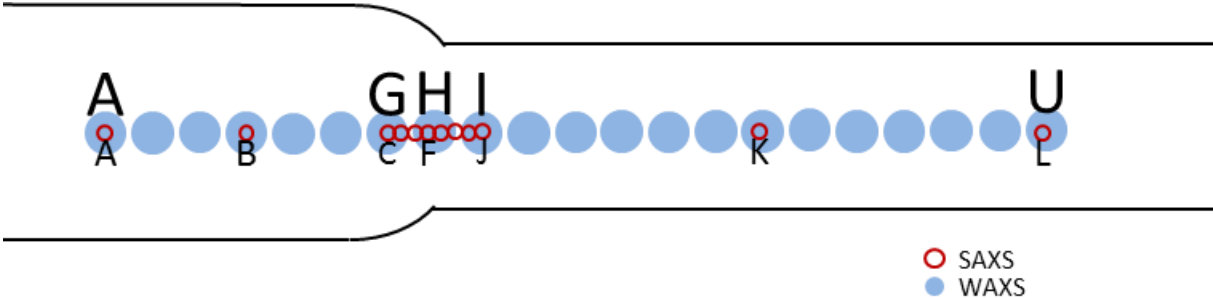


Figure A. 1: Enlarged illustration, showing notation for WAXS above the circle and SAXS below.

## B. Tensile Testing of Plates

In the following figures, only one sample of each setting is shown. For the case where more than one sample was tested, the chosen sample is representative of the series.

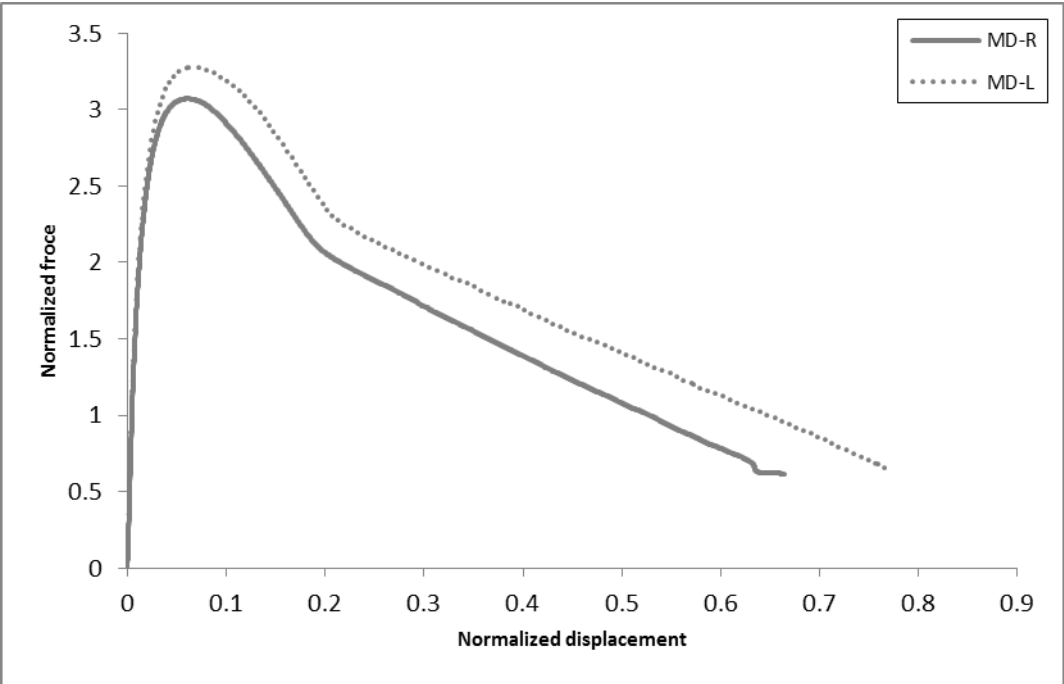


Figure B.1: Different MD specimen.  
(At 100 mm/min, crack length 15 mm, gauge length 30 mm and center position of grips.)

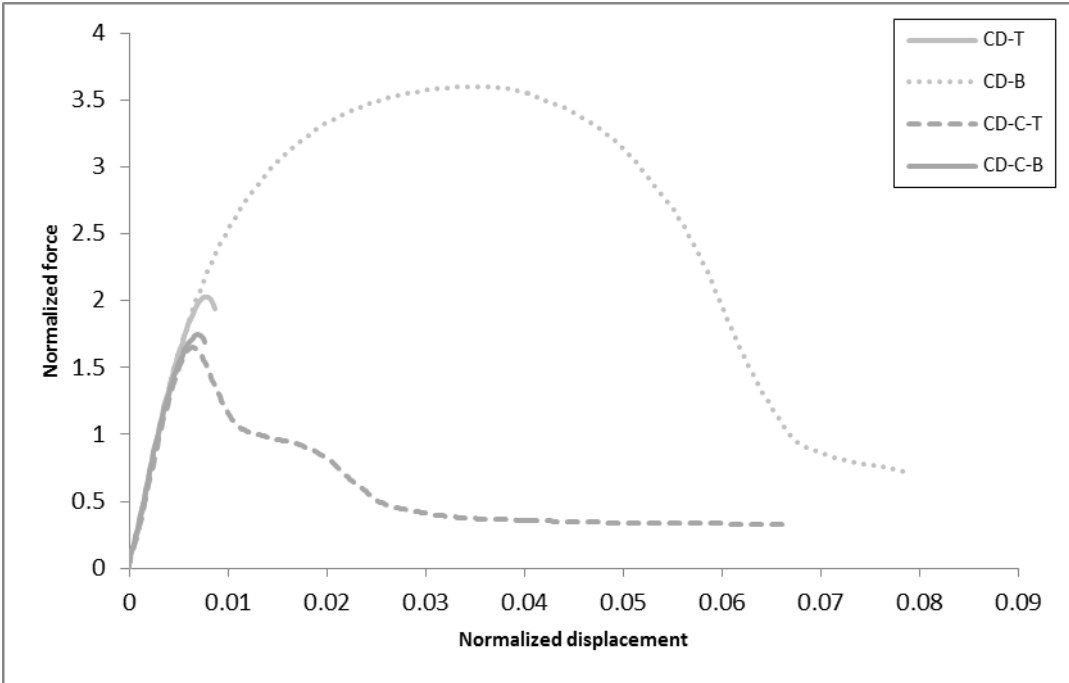


Figure B.2: : Different CD specimen.  
(At 100 mm/min, crack length 15 mm, gauge length 30 mm and center position of grips.)



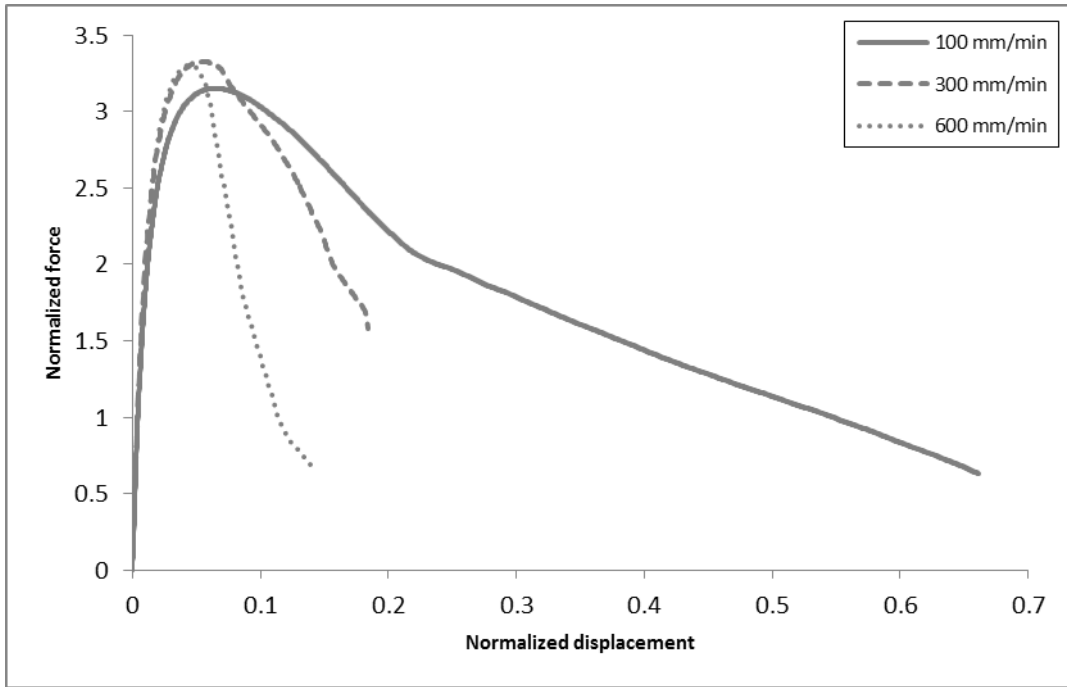


Figure B.3: Speed dependency.  
(MD-R, crack length 15 mm, gauge length 30 mm and center position of grips.)

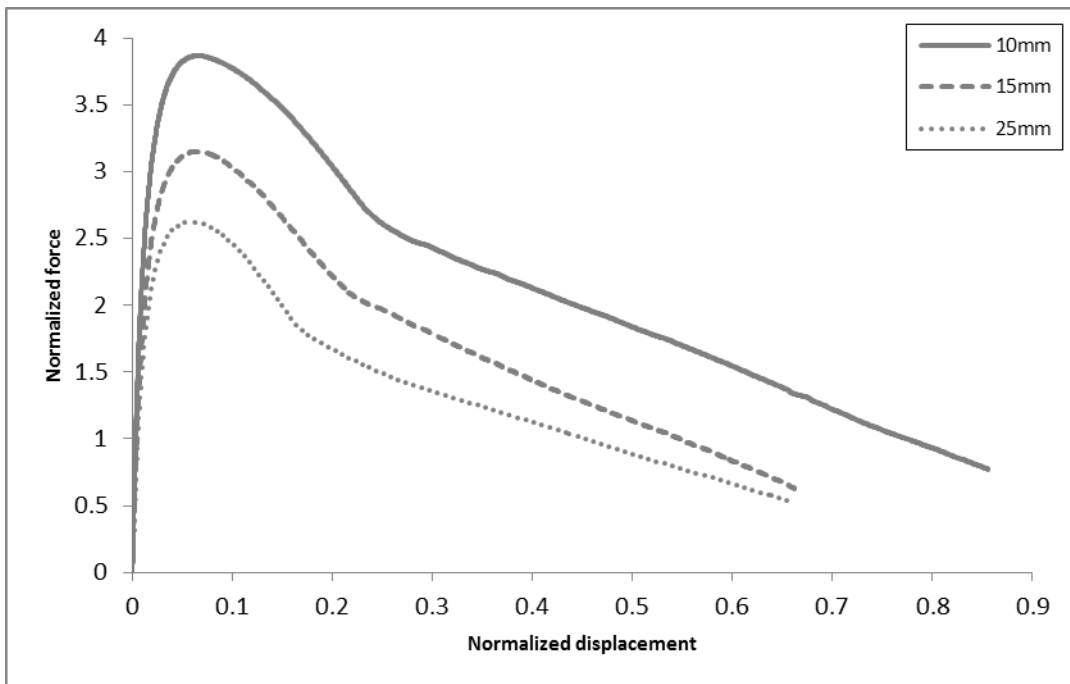


Figure B.4: Crack length dependency.  
(MD-R at 100 mm/min, gauge length 30 mm and center position of grips.)

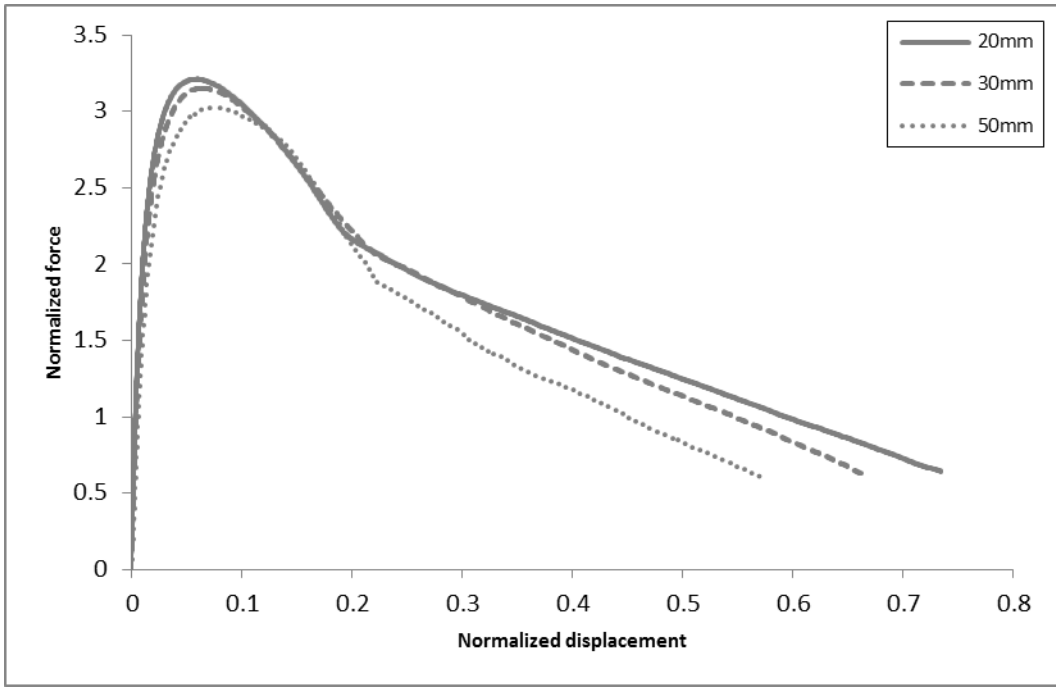


Figure B.5: Gauge length.  
 (MD-R at 100 mm/min, crack length 15 mm and center position of grips.)

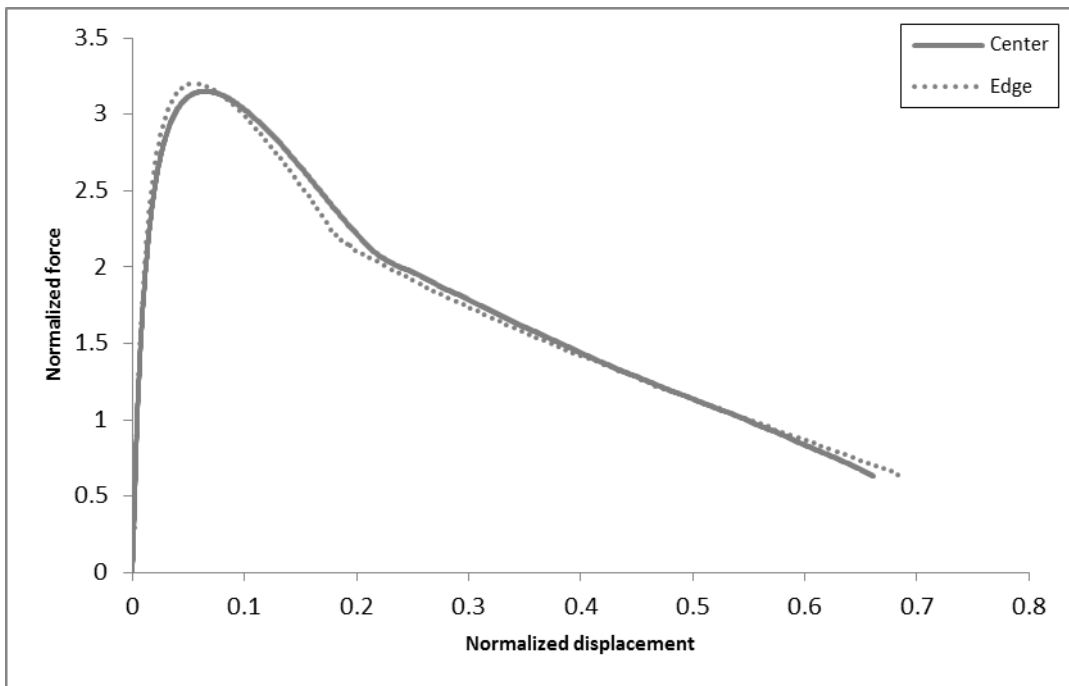
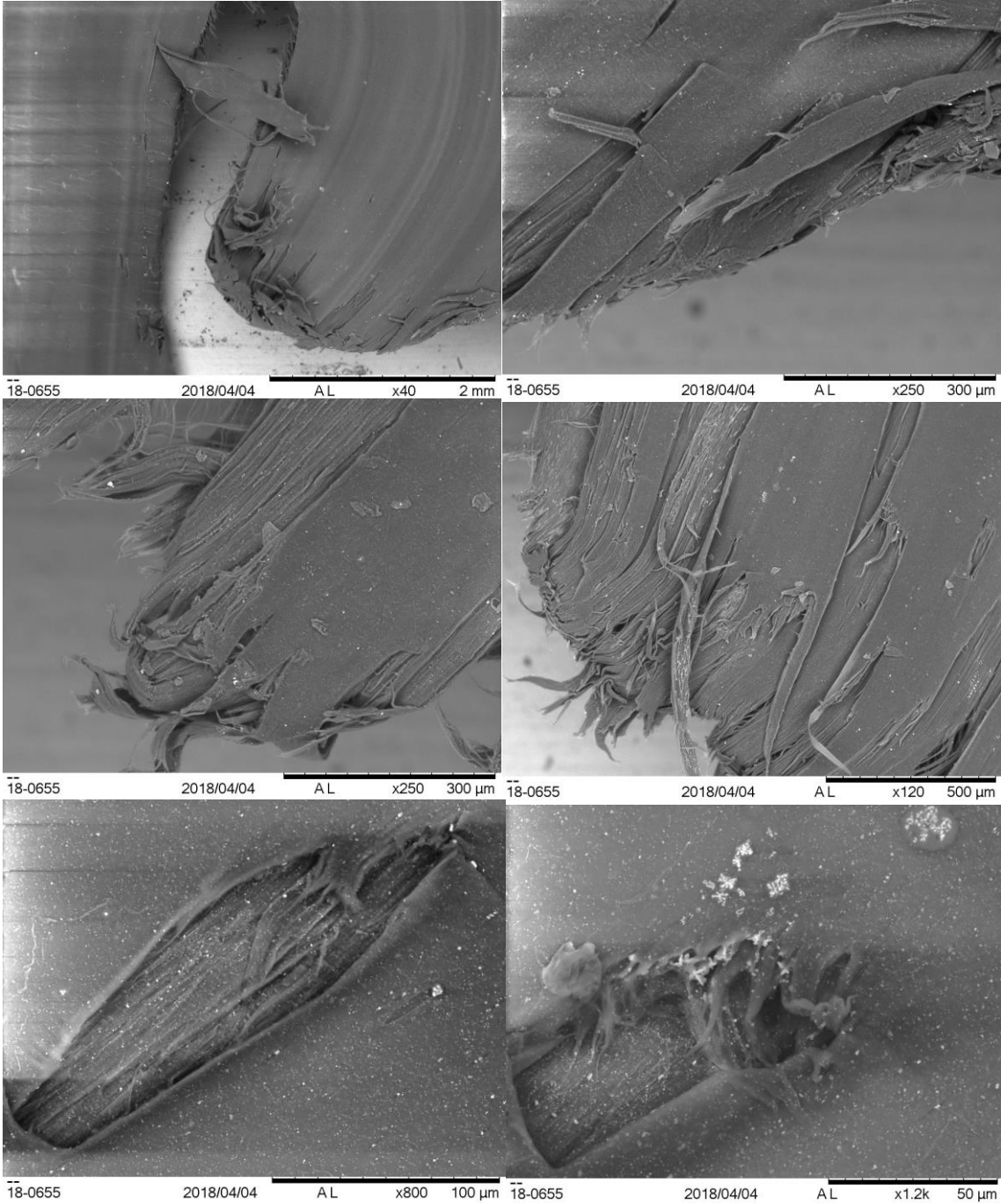
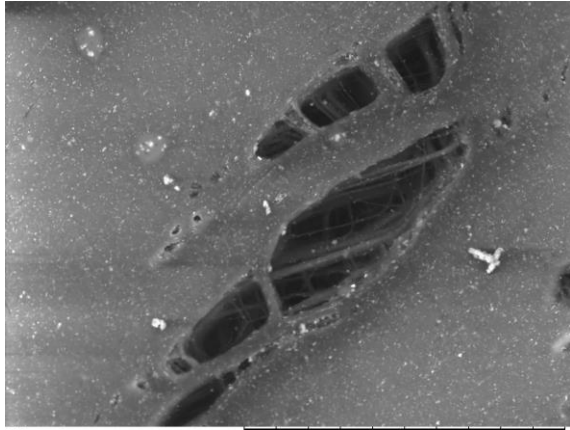


Figure B.6: Grip position.  
 (MD-R at 100 mm/min, crack length 15 mm and gauge length of 30 mm.)

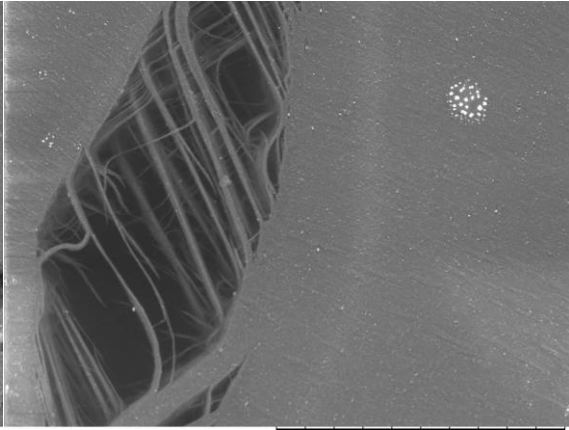
### C. SEM-images

SEM-images of a fractured MD-R sample.

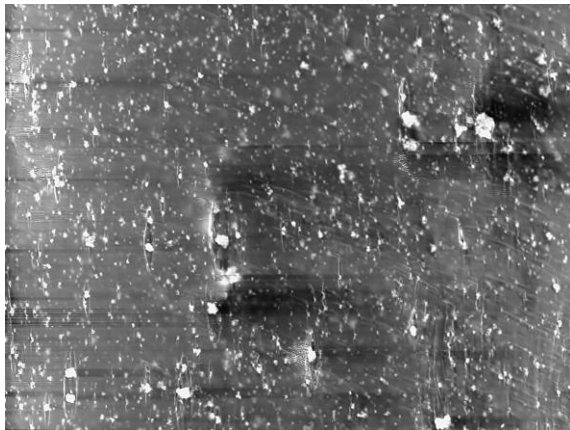




18-0655 2018/04/04 AL x1.0k 100 μm



18-0655 2018/04/04 AL x300 300 μm



18-0655 2018/04/04 AL x3.0k 30 μm



18-0655 2018/04/04 AL x180 500 μm